



THE UNIVERSITY
of LIVERPOOL

DEPARTMENT OF ENGINEERING

Ph.D. THESIS

**MICROMACHINING WITH SINGLE MODE FIBRE
LASERS FOR MEDICAL DEVICE PRODUCTION**

Thesis submitted in accordance with the requirements of
the University of Liverpool for the degree of Doctor in
Philosophy

by

Klaus Kleine

December 2009

DECLARATION

I hereby declare that all of the work contained within this dissertation has not been submitted for any other qualification.

Sign: _____

Date:

Word Count = 28874

INTRODUCTION

This Thesis is based on several research and development programs to implement the use of fibre lasers in the manufacturing of medical devices like stents and pacemakers. In general, the medical device manufacturing industry has a high demand for laser micromachining applications. The content of the thesis describes laser micromachining of metallic components with single mode fibre lasers. At the time I started my research, most laser machining processes used flash-lamp pumped solid-state lasers for those applications. Reliable laser operation and low maintenance are required to meet the yields and up-time requirements for medical devices, such as stent cutting and pacemaker welding. Many lasers for micromachining applications are configured to operate near the diffraction limited beam performance to achieve very small feature sizes. It is challenging to maintain such a laser system performance in a production environment.

The fibre laser provides a number of attractive features that could address the needs to maintain high up-time and high yields:

- A single mode fibre laser does not require mirror alignment.
- Diode pumped fibre lasers reduce maintenance due to eliminating the flash lamp change.
- The compact air-cooled design helps to save expensive clean room space on the production floor.

By 2000 the increases in average laser power extended the use of the fibre lasers into industrial applications such as cutting and welding. This fact

spurred further development of high power fibre laser leading to the multi kilowatt levels currently available. The lasers investigated in this thesis generated 50 W to 200 W of laser power, representing the highest power levels commercially available at that time.

For the microcutting of medical implants such as stents and guide wires, kerf width and sidewall surface quality are of special interest. Developing processes capable of achieving these criteria was the primary objective of the research described in this thesis. A secondary concern is the heat affected zone created by the laser machining process. Operation conditions to minimize this effect are also discussed in this thesis.

Many microwelding applications in the electronics, telecom and medical device industry require smaller and smaller laser joining areas. The quality of a laser welded joint is very dependant on the temporal and spatial parameters of the laser beam. These parameters must be adjusted to match to the processing speed and the materials being welded. Switching continuous wave fibre lasers can achieve the parameters for processes requiring low average power. However the pulse-to-pulse stability can effect the process and has been investigated. Some welding applications require focus spot diameters in the order of 50 μm and pulse energy levels as low as 10 mJ. The fibre laser's excellent single mode beam quality provides the desired spot size and laser power density.

The research summarized in this thesis was performed to prove that fibre lasers are viable tools for micromachining. This thesis compares fibre laser machining results with those using legacy laser processes and describes ways to improve the quality of the fibre laser machining process.

The research work resulted in two patents on fibre laser microcutting and one patent application on pulsed synchronized output (PSO) cutting that is

currently under review. The patents and the filed application are listed in chapter 4.

CONTENTS

DECLARATION	II
INTRODUCTION	III
CONTENTS.....	1
ACKNOWLEDGMENTS.....	4
LIST OF FIGURES.....	5
1. LITERATURE REVIEW.....	10
1.1. MEDICAL DEVICES INVESTIGATED.....	10
1.1.1. <i>Stents</i>	10
1.1.2. <i>Pacemakers</i>	12
1.2. LASER MICROMACHINING.....	15
1.2.1. <i>Optics for Micromachining with Solid State Lasers</i>	17
1.2.2. <i>Laser Cutting with Solid State Lasers</i>	21
1.2.2.1. <i>Fusion Cutting Process</i>	22
1.2.2.2. <i>Reactive Fusion Cutting</i>	24
1.2.3. <i>Focus position</i>	25
1.2.4. <i>Sidewall Striation</i>	26
1.2.5. <i>Laser Microwelding with Solid State Lasers</i>	31
1.2.5.1. <i>Conduction Laser Welding</i>	32
1.2.5.2. <i>Keyhole Laser Welding</i>	33
1.2.5.3. <i>Microwelding Laser Parameters</i>	34
1.3. GAS NOZZLES FOR LASER MICRO PROCESSING APPLICATION.....	37
1.3.1. <i>Laser Cutting Nozzle</i>	37
1.3.2. <i>Laser Welding Nozzle</i>	39
1.4. LASERS FOR MICROMACHINING INVESTIGATED FOR THIS THESIS.....	40
1.4.1. <i>Flash lamp pumped Nd:YAG Lasers</i>	41
1.4.1.1. <i>Lamps for Pumping Solid State Lasers</i>	45
1.4.2. <i>Diode Pumped Fibre Lasers</i>	48
1.4.2.1. <i>Laser Diodes for Pumping of Fibre Lasers</i>	54
2. FIBRE LASER FOR MICROCUTTING.....	58
2.1. EXPERIMENTAL LASER CUTTING SETUP.....	58
2.1.1. <i>Fibre Laser Stent Cutting System</i>	59
2.1.2. <i>Fibre Laser Flat Sheet Cutting System</i>	60
2.1.3. <i>Nd:YAG Stent Cutting System</i>	62
2.1.4. <i>Motion System for Laser Cutting</i>	63
2.1.5. <i>Laser Cutting Head</i>	65
2.1.6. <i>Material and Assist Gas for the Cutting Experiments</i>	69
2.1.7. <i>Beam Diagnostic Setup of YAG Laser and Fibre Lasers</i>	69

2.1.8.	<i>Laser Pulse Measurement</i>	73
2.1.9.	<i>Surface Roughness Measurement</i>	75
2.2.	COMPARING PULSED FIBRE LASERS WITH TRADITIONAL FLASH LAMP PUMPED ND:YAG SOLID STATE LASERS.....	77
2.2.1.	<i>Beam Quality Measurement</i>	77
2.2.2.	<i>Temporal Behavior</i>	80
2.2.2.1.	<i>Temporal Behavior of Fibre Lasers</i>	80
2.2.2.2.	<i>Temporal Behavior of Flash Lamp Pumped Nd:YAG Lasers</i>	83
2.2.3.	<i>Comparing the cutting results of the Fibre Laser Cutting Process with the Flash Lamp Pumped Nd:YAG Laser</i>	84
2.2.4.	<i>Conclusion on initial experiments to compare Nd:YAG Laser and Fibre Laser cutting</i>	89
2.3.	PULSED FIBRE LASER CUTTING PROCESS OPTIMIZATIONS	90
2.3.1.	<i>Fibre Laser Cutting Experiment Scope</i>	92
2.3.2.	<i>Effect of Laser Peak Pulse Power on Surface Roughness</i>	92
2.3.3.	<i>Effects of Laser Pulse Frequency on Surface Roughness</i>	95
2.3.4.	<i>Effect of laser cutting parameters on recast layer thickness</i> 97	
2.3.5.	<i>Conclusion on Pulsed Fibre Laser Cutting Parameter Optimization</i>	104
2.4.	INFLUENCE OF PULSE SHAPE ON FIBRE LASER CUTTING RESULTS....	104
2.4.1.	<i>Cutting System Setup for Pulsed Shaped Cutting</i>	105
2.4.2.	<i>Influence of laser pulse shape on cutting quality</i>	106
2.4.3.	<i>Conclusions on Pulse Shaping</i>	109
2.5.	POSITION SYNCHRONIZED FIBRE LASER CUTTING PROCESS.....	109
2.5.1.	<i>Position Synchronized Fibre Laser Cutting System Setup</i> .	110
2.5.2.	<i>Position Synchronized Fibre Laser Cutting Calculations and Modeling</i>	111
2.5.3.	<i>Position Synchronized Fibre Laser Cutting Process Results and Discussion</i>	118
2.5.4.	<i>Laser Cutting Results for Pulsed Synchronized Cutting</i>	120
2.5.5.	<i>Conclusion on Pulsed Synchronized Cutting</i>	122
3.	FIBRE LASER FOR MICROWELDING	123
3.1.	FIBRE LASER WELDING EXPERIMENTAL SETUP.....	123
3.1.1.	<i>Material and Assist Gas for the Welding Experiments</i>	127
3.2.	CONTINUOUS WAVE WELDING WITH FIBRE LASER EXPERIMENTS ...	129
3.2.1.	<i>Welding of Stainless Steel with CW Fibre Lasers</i>	129
3.2.1.	<i>Welding of Titanium with CW Fibre Lasers</i>	133
3.2.2.	<i>Conclusions on Continuous Wave Fibre Laser Welding</i>	137
3.3.	PULSED FIBRE LASER WELDING PROCESS	139
3.3.1.	<i>Background on Pulsed Fibre Laser Welding</i>	139
3.3.2.	<i>Experimental Work on Pulsed Fibre Welding</i>	139
3.3.3.	<i>Welding of Stainless Steel with Pulsed Fibre Lasers</i>	140
3.3.4.	<i>Welding of Titanium with Pulsed Fibre Lasers</i>	144

ACKNOWLEDGMENTS

The author wishes to express sincere appreciation to Professor Watkins for his assistance during the Ph.D. program and in the preparation of this thesis. In addition, special thanks to Dr. Tony Hoult for his help as an off-campus advisor. Thanks to Dr. Silke Pflueger, Dr. Stuard Mac Cormack and Dr. Murray Reed for their valuable input. Thank you also to the members of the school council for their support.

In addition I would like to thank Dr. Steve Jones for his support at Guidant Inc.

I would like to thank Guidant for funding the project and for providing equipment and materials during the course of my Ph.D.

I would like to thank Abbot Medical for giving me access to the company library.

LIST OF FIGURES

<i>Number</i>	<i>Page</i>
Fig. 1: Stent delivery system.....	11
Fig. 2: Stent pattern delivery system	11
Fig. 3: Boston Scientific Pacemaker (Image taken from www.bostonscientific.com).....	13
Fig. 4: X-Ray image of an implanted pacemaker with an atrial and ventricular lead	14
Fig. 5: Laser welding glow box with loading chamber from Braun TM	15
Fig. 6: Holes 40 mm square drilled through a human hair using a 183 nm Excimer Laser	16
Fig. 7: Longitudinal and lateral spherical aberration	18
Fig. 8: Longitudinal and lateral spherical aberration	18
Fig. 9: single-element plano-convex lens compared with a two element achromat	19
Fig. 10: Encircled energy at different radii for a singlet and doublet F/5 lenses focusing 1064 nm radiation from a Nd:YAG Laser.	20
Fig. 11: Schematic diagram of fusion cutting process and resultant cut kerf geometry.	22
Fig. 12: Relationship between viscosity and temperature for iron and FeO.	25
Fig. 13: Focus position and cutting quality.	26
Fig. 14: Walls of the kerf show striations exhibiting cut and break sections	28
Fig. 15: Cut surface of 6 mm thick oxygen cut mild steel as a function of speed and focal plane position, cut with 1.5 kW CO ₂ laser at 3 bar .	29
Fig. 16: The effect of cutting speed on cut quality at various pulse frequencies.	30
Fig. 17: Sidewall of stent patterns with dross at the bottom of the cut.	31
Fig. 18: Laser welding.	32
Fig. 19: Conduction Laser Welding.	33
Fig. 20: Keyhole Laser Welding.....	34
Fig. 21: Supersonic flows colliding with matter always generate at least one shock wave. In free jets, a shock-barrel structure contains a silence zone isolated from ambient atmosphere by a lateral shock barrel and a front shock called Mach disk	38
Fig. 22: Cutting speed as a function of oxygen purity in 3 mm mild steel, 1kW fibre laser, 3 bar,	39
Fig. 23: Laser welding configuration with co-axial shield gas nozzle	40
Fig. 24: Schematic diagram of flash lamp pumped Nd:YAG Laser.....	41
Fig. 25: Irradiance Distribution in a TEM ₀₀ beam	42

Fig. 26: Fundamental mode dimensions inside the laser rod as a function of focal length of the thermally induced lens.	43
Fig. 27: Mirror misalignment in an argon laser that will produce 10% drop in output power versus normalized mirror radius.	44
Fig. 28: Typical design of an arc lamp	45
Fig. 29: Fractional utilization of krypton lamp output by Nd:YAG	47
Fig. 30: Single-clad fibre laser geometry. The rare-earth active core is surrounded by a cladding and a polymer coating	49
Fig. 31: Double-clad fibre laser geometry. The rare-earth active core is surrounded by a cladding, outer clad and a polymer jacket	50
Fig. 32: Fibre Laser arrangement with free space two diode-stack pump sources. HR: high reflective, HT: high transmission	51
Fig. 33: Fibre Laser arrangement end-pumped with spliced couplers and fibre coupled diodes	52
Fig. 34: Concept of a GT wave fibre	52
Fig. 35: Structure of an evanescent field pumped fibre laser.....	53
Fig. 36: Structure of a semiconductor laser	54
Fig. 37: Laser diode mounted on heat sink (Bookham Product information).	55
Fig. 38: Pump spectrum of an ytterbium-doped fibre laser	56
Fig. 39: Experimental fibre laser (IPG PYL 50) cutting system in the laser lab at Guidant for the stent cutting experiment (tubular material)....	59
Fig. 40: IPG YLM 50W fibre laser with collimator.....	60
Fig. 41: Experimental fibre laser cutting system with a SPI 100W single mode fibre laser and Aerotech linear stage motion system for the flat sheet cutting experiments.	61
Fig. 42: SPI 100C fibre laser with delivery fibre and collimator.....	62
Fig. 43: Lasag KLS 246 FC lamp pumped Nd:YAG laser	63
Fig. 44: PSO Control logic	65
Fig. 45: LaserMech™ Cutting Head	66
Fig. 46: Coma appears in the focus because of off-axis rays focus at different points	67
Fig. 47: Laser beam on View-it ® from Kentek Inc.	68
Fig. 48: Calculation of beam quality from measured caustic.....	70
Fig. 49: Typical Beam Profile of a single mode Nd:YAG laser measured with the M200 from Spiricon™	72
Fig. 50: Beam quality measurement setup M200 from Spiricon™	73
Fig. 51: DET410 Spectral responsively curve.....	74
Fig. 52: Photo diode measurement setup.....	75
Fig. 53: Veeco™ Optical Profiler 3300N at Guidant.....	76
Fig. 54: Veeco™ Optical Profiler 3300N screen-shoot.	76
Fig. 55: Beam propagation for fibre laser after collimator, at 4.5 W with 0.1 ms pulse length and 1500 Hz pulse frequency. $M^2 = 1.15$ for a 500 mm focusing optic.	77

Fig. 56: Beam propagation of lamp pumped pulsed Nd:YAG laser after collimator, at 4.5W with 0.1 ms pulse length and 1500Hz pulse frequency, M2 = 1.14 with a 500 mm focusing optic.	78
Fig. 57: Screen shot of typical Fibre Laser Pulse Shape measured with a Tektronix 100 MHz digital oscilloscope and a Thorlabs (DET410/M) InGaAs photo diode with a 0.5 ns response time.	80
Fig. 58: Temporal behaviour of a typical fibre laser pulse exported of a Tektronix 100 MHz digital oscilloscope measured with a Thorlabs (DET410/M) InGaAs photo diode with 0.5 ns response time.	82
Fig. 59: Temporal behaviour of a lamp pumped Nd:YAG laser exported of a Tektronix 100 MHz digital oscilloscope measured with a Thorlabs (DET410/M) InGaAs photo diode with 0.5 ns response time.	83
Fig. 60: SEM picture of a laser cut sidewall with a pulsed fibre laser.	86
Fig. 61: SEM picture of a laser cut side-wall with a pulsed lamp pumped Nd:YAG laser.	86
Fig. 62: Optical profiler picture of a laser cut side-wall for a pulsed fibre laser.	87
Fig. 63: Optical profiler picture of a laser cut side-wall for a pulsed lamp pumped Nd:YAG laser.	88
Fig. 64: SEM picture of a stainless steel stent stent delivery system after ultra sonic cleaning.	91
Fig. 65: SEM picture of a stainless steel stent stent after electro polishing.	91
Fig. 66: Average surface roughness as a function of laser peak power with indication of measurement location.	93
Fig. 67: Optical Profiler Image for Laser Cut Sidewall at 20W Laser Peak Power. At 1500 Hz pulse frequency.	94
Fig. 68: Optical Profiler Image for Laser Cut Sidewall at 40W Laser Peak Power. At 1500 Hz pulse frequency.	94
Fig. 69: Average Surface Roughness as a Function of Laser Pulse Frequency. SEM Pictures for 600Hz and 3000Hz.	96
Fig. 70: Theoretical surface roughness caused by overlapping laser pulses at 600Hz.	96
Fig. 70: Cross-section of stainless steel sample. The recast layer is visible on the left side of the sample (sample is chemical etched to make grain boundary visible).	98
Fig. 71: Influence of laser pulse length and cutting speed on recast layer thickness (in μm) at 7 bar assist gas pressure. The recast layer thickness is labeled on the contour line.	100
Fig. 72: Influence of laser pulse length and cutting speed on recast layer thickness (in μm) at 3.5 bar assist gas pressure.	101
Fig. 73: Influence of Laser Pulse Length and Cutting Speed on Necessary Minimum Average Laser Power.	102

Fig. 74: Influence of frequency on minimum average power and peak power for 0.1 mm stainless steel at 6 mm/s, 6 bar oxygen pressure and 0.1 ms pulse length.	103
Fig. 75: Response of the fibre laser output (solid line) to ramped-down diode pumping	106
Fig. 76: Response of the fibre laser output to a ramped-up diode pumping	107
Fig. 77. : Minimum average required laser power as a function of laser pulse length for the three different pulse shapes	108
Fig. 78. : Influence of ramp-down and ramp-up pulses on taper.	109
Fig. 79: Block diagram of the experimental fibre laser cutting systems with a SPI Laser 100W single mode fibre laser and Aerotech linear stage motion system with a feedback between the motion system and the fibre laser system.	111
Fig. 80: Power loss due to heat conduction as function of cutting speed.	113
Fig. 81: Laser power contributed directly to the cutting process (dashed line) and laser power setting (solid line) at laser system.	115
Fig. 82: Heat penetration to 600°C as a function of cutting speed based on the energy lost through heat conduction resulting from the energy balance for 50W of fibre laser power and a power loss due to heat conduction of 25W.	117
Fig. 83: Velocity and position as a function of the timing (Clock signal in ms) of the CNC motion system	118
Fig. 84: Velocity as a function of the timing signal of the CNC system.	119
Fig. 85: Pulse train during PSO controlled acceleration and deceleration as a function of timing (Clock signal in ms).	120
Fig. 86: Sample of a fibre laser cut without PSO.	121
Fig. 87: Picture of a sample laser cut with PSO.	121
Fig. 88: Experimental setup of the continuous wave fibre laser welding system.	124
Fig. 89: Two axis galvanometer scanner setup from SaenLab™.	125
Fig. 90: Picture of the Experimental Pulsed Welding System.	126
Fig. 91: Welding head from LaserMech™ for pulsed welding with a fibre laser.	127
Fig. 92: Bausch and Lomb microscope with camera that was used for the weld geometry measurements.	128
Fig. 93: Top view of fibre laser CW weld beads in stainless steel at 100W peak power for 25 mm/s, 50 mm/s and 75 mm/s weld (right to left) speed and argon shielding.	129
Fig. 94: Weld width as a function of welding speed and laser power for stainless steel (304 Series) with argon shielding.	130
Fig. 95: Cross section of fibre laser CW weld beads in stainless steel at 100W peak power for 100 mm/s, 125 mm/s and 150 mm/s weld speed (right to left) and argon shielding.	131

Fig. 96: Weld penetration depth as a function of welding speed and laser power for stainless steel (304 Series) with argon shielding.....	131
Fig. 97: Weld bead width as a function of welding speed and laser power for titanium (Grade 1) with argon shielding.....	134
Fig. 98: typical cross section of a fibre laser CW weld after etching the titanium sample to make the weld zone visible. Insert with blue line indicating actual melted areas.....	135
Fig. 99: Weld penetration depth as a function of welding speed and laser power for titanium (Grade 1) with argon shielding.	136
Fig. 100: Temporal behavior of a typical fibre laser pulse for laser welding measured with a Tektronix TDS 3032B 300 MHz digital oscilloscope and a Thorlabs (DET410/M) InGaAs photodiode with a 0.5 ns response time.	140
Fig. 101: Typical cross section of a fibre laser weld after etching the steel sample to make the weld zone visible.	141
Fig. 102: Weld penetration depth in stainless steel as a function of laser peak power for 200Hz pulse-to-pulse frequency and 4 mm/s weld speed with argon shielding gas.....	142
Fig. 103: Top view of fibre laser weld beads in stainless steel (left to right) at 40W, 60W, 80W and 100W peak power for 200Hz pulse-to-pulse frequency, 2 ms pulse length, 4 mm/s weld speed and argon shielding gas.	143
Fig. 104: Weld width as a function of laser peak power and pulse width in stainless steel for 200 Hz pulse-to-pulse frequency, 2 and 4 ms pulse length, 4 mm/s weld speed and argon shielding.	144
Fig. 105: Typical cross section of a fibre laser weld after etching the titanium sample to make the weld zone visible.	145
Fig. 106: Sample pulse train for Energy stability measurement.	147
Fig. 107: Short term power stability over 20 seconds at 100Hz, 2 ms pulse length, 50 W peak power and 10 W average power.	147
Fig. 108: Long term power stability over 1 hour at 100Hz, 2 ms pulse length, 50 W peak power and 10 W average power.	148

1. Literature Review

Developing or improving new production technologies in a manufacturing environment can be complex. The process must be reliable, consistent and repeatable. This review describes two medical devices and the specific laser applications used in their manufacturing. This chapter provides a review of the technology behind the established lamp pumped Nd:YAG lasers in contrast to the improvements that can be achieved with the fibre laser. It concludes with a review of the laser microcutting and welding processes.

1.1. Medical Devices Investigated

Cutting of stents and the welding of pacemaker cans are the two applications that have driven the developments in this research project. This research is applicable to many other existing and potential applications however the sponsor (Guidant Inc.) was specifically interested in results related to these two devices.

1.1.1. Stents

The stent was introduced in the late 1980s for vascular endoluminal endoprosthesis. At that time it was a valuable new technique for interventional radiologists and cardiologists¹.

Stents (Figure 1) are cylindrical metal scaffoldings that are inserted inside a diseased coronary artery to restore adequate blood flow. Most stents are balloon inflatable². A guide wire guides a stent crimped onto a balloon to the diseased area of the blood vessel. The balloon is inflated and the stent is pushed against the artery wall. The stent will stay in place after the balloon is deflated and the balloon and the guide wire are removed, keeping the blood vessel open.

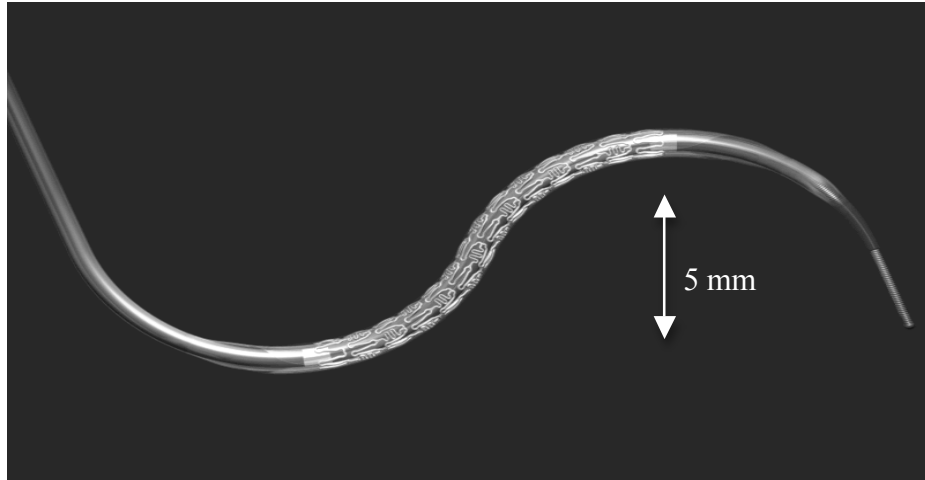


Fig. 1: Stent delivery system

Stents are made of many different materials, the most commonly used material being stainless steel. Therefore, this thesis focuses on the microcutting of stainless steel (316). Other materials used include shape memory metals such as NiTi and other super alloys and polymers.

Kern documents some of the ideal stent characteristics². Those are conformity, flexibility, radial strength, low metallic surface area and low profile. Those characteristics require that a complex structure needs to be cut out of a solid piece of metallic tubing. A typical stent pattern is shown by Serruys et al in figure 2 below. The total length of the pattern shown in Figure 2 is about 15 mm. The width is about 5 mm.

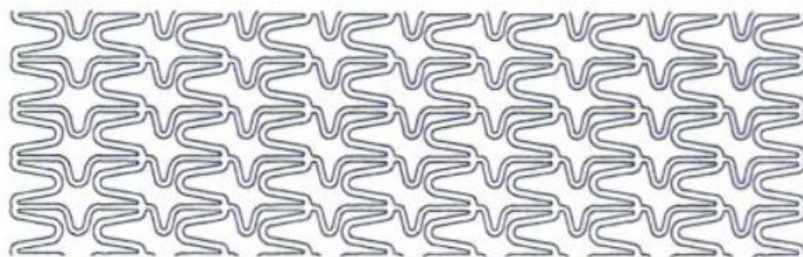


Fig. 2: Stent pattern delivery system³

Stent patterns such as the one shown in figure 2 need to be machined very accurately to ensure even expansion of the stent in the blood vessel. An uneven expansion of the stent will cause an insufficient scaffolding of the vessel wall and could lead to medical complications⁴.

Because of the small structure and the tight geometries, only a small focused laser beam can machine stents out of metal or tubing. To ensure the mechanical performance of the stent, the laser power needs to be adapted to a setting that will not anneal the metal. Therefore, the heat affected zone needs to be very small.

Laser cutting for micromachining stents is already an established process in the medical device industry. Saunders⁵ patented the laser cutting process of stents in 1994. In this patent he describes the use of a lamp pumped solid state Nd:YAG laser for cutting a stent out of a tubular member. Further it states “that a plurality of laser cut cylindrical elements are formed from a tubular member”. Those cylindrical elements are interconnected and aligned on a common longitudinal axis. The elements are comprised of a number of struts that are rectangular in cross section.

The low output power of fibre lasers prevented this laser technology from being used for stent cutting on a production scale. Improvements in average power made the fibre laser suitable for the first industrial stent cutting applications in 2002⁶. A paper presented at the ICALEO in 2002 based on the research for this thesis reported first published industrial results in this field⁷.

1.1.2. Pacemakers

The pacemaker (figure 3) is a medical device that sends electrical impulses to the heart muscles. Electrodes (leads) deliver the impulses to a specific region in the heart. The function of the pacemaker is to maintain an

adequate heart rate. The first pacemaker was implanted in 1958⁸. Modern devices combine a defibrillator and a pacemaker. The expected lifetime of a pacemaker is 6-12 years⁹.



Fig. 3: Boston Scientific Pacemaker (Image taken from www.bostonscientific.com)

The components of the pacemaker must be biocompatible and are typically made out of titanium or stainless steel. Pacemakers are implanted close to heart in the patient's chest.

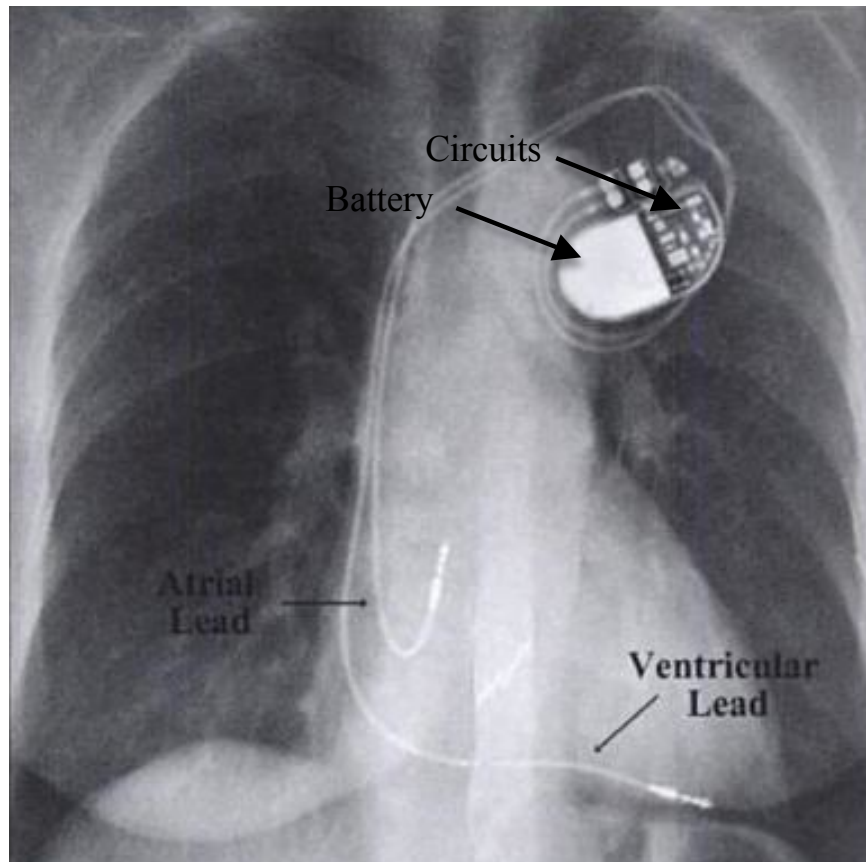


Fig. 4: X-Ray image of an implanted pacemaker with an atrial and ventricular lead¹⁰

Figure 4 shows an x-ray image of an implanted pacemaker¹⁰. A pacemaker-can must be sealed hermetically to ensure reliable operation of the device over the required lifetime of at least 12 years. Pulsed solid-state laser welding with a Nd:YAG laser is the established process for the pacemaker-can production. The pacemaker contains electronic circuits and batteries that must not be damaged during the laser welding process (see labels in figure 4). Fluctuations and variations in laser pulse power or energy can easily penetrate into the sensitive areas of the pacemaker interior. The welding is done in a glove box in an inert environment.



Fig. 5: Laser welding glow box with loading chamber from Braun TM

Figure 5 shows such a glove box with the laser system on the left and the loading chamber on the right side. Due to the sealed enclosure of these glove boxes it is preferable to integrate a fibre coupled solid-state laser or a fibre laser.

1.2. Laser Micromachining

Miniaturization is a very important trend for emerging technologies in general and for the medical device technology specifically. The field of micro fabrication employs various technologies, such as micro drilling, micro milling, focused ion beam micromachining and laser micromachining ¹¹. Gruenewald et al¹² state that high speed, low unit cost material processing with micron or submicron resolution underpins nearly all industries manufacturing high technology products. As an early illustration, features ablated in human hairs are used to show the high-resolution capability for laser micromachining. Figure 6 shows that the

pattern in the human hair is ablated without heat degradation such as melting, charring or burning. The size of the square holes drilled is 40 μm .

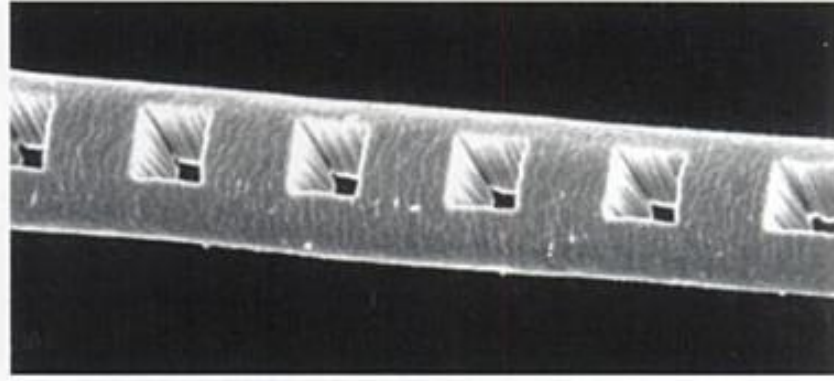


Fig. 6: Holes 40 μm square drilled through a human hair using a 183 nm Excimer Laser

The following equation¹⁴ shows that the wavelength (λ) has a direct influence on the focused spot size of the laser beam.

$$d_{\min} = \frac{4M^2\lambda f}{\pi d_0} \quad (1.1)$$

where d_0 is the beam diameter at the focusing optic, f the focal length, M^2 is beam quality factor and d_{\min} is the focus diameter.

The equations shows that shorter wavelengths are preferable but lasers in the UV range such as the excimer laser are more complex and require more maintenance. Toenshoff¹⁵ et al present microcutting results in metals using an excimer laser but conclude that excimer lasers have low economical efficiency. This is mainly due to the high cost of the excimer laser and the low ablation rates in metals. The high absorption in polymers and the low heat affected zone limits the industrial use of excimer laser primarily to micromachining of plastics and ceramics¹⁶.

Longer wavelength lasers, such as a CO₂ laser at 10.6 μm, will have larger focus spot sizes than a Nd:YAG or fibre laser operating in the wavelength range of 1 μm. Ion et al¹⁷ reported cutting results for a CO₂ laser with short focal length optics. Using standard beam delivery systems for cutting (63 mm focusing optic with a 15 mm collimated beam) the resulting 75 μm spot is too large to enable this laser to be used for micromachining application, such as stent cutting where the spot size needs to be smaller than 25 μm.

The Nd:YAG laser at 1064 nm and the fibre laser at 1030-1080 nm¹⁸ were selected for this investigation because they offer high absorption in metals combined with small spot size and cost efficiency. Schuoecker¹⁹ states that the pulsed operation of solid state lasers can improve the quality of the cut, especially if used for cutting narrow geometries. Further, he states that pulsed operation decreases the flow of energy thereby reducing the heat affected zone and improving the surface roughness.

1.2.1. Optics for Micromachining with Solid State Lasers

The focusing optics for laser micromachining need be selected carefully. Optics that have minimum aberration are preferred for micromachining. There are two classes of aberration; monochromatic and chromatic aberration²⁰. This work was performed with a single wavelength laser, so the chromatic aberration has negligible effect on the spot size. On the other hand, the monochromatic aberration can have an impact on the spot size. The monochromatic aberration results from the lens geometry. The aberration that can be most influenced by the lens selection is the spherical aberration. Figure 7 shows the longitudinal and lateral aberration for a lens. The “circle of least confusion” in figure 7 marks the best focus plane for the smallest spot size.

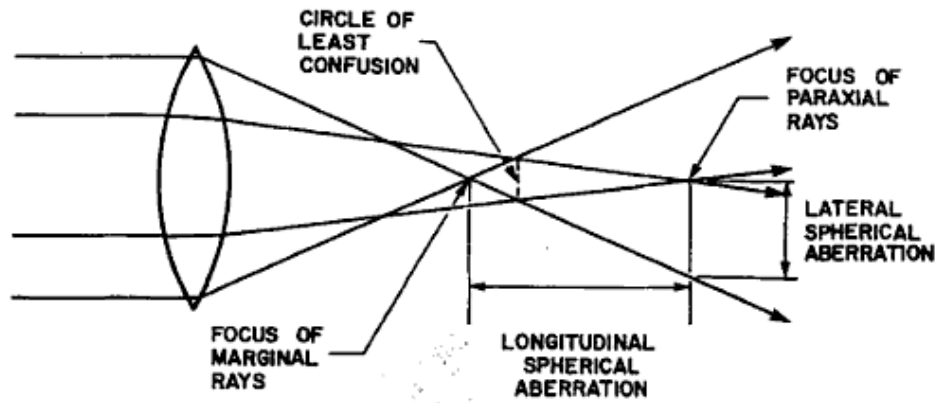


Fig. 7: Longitudinal and lateral spherical aberration²¹.

The lens shape has a major impact on the spherical aberration. In figure 8, the aberrations in longitudinal and transverse (or lateral) directions of a positive singlet is plotted as a function of shape factor.

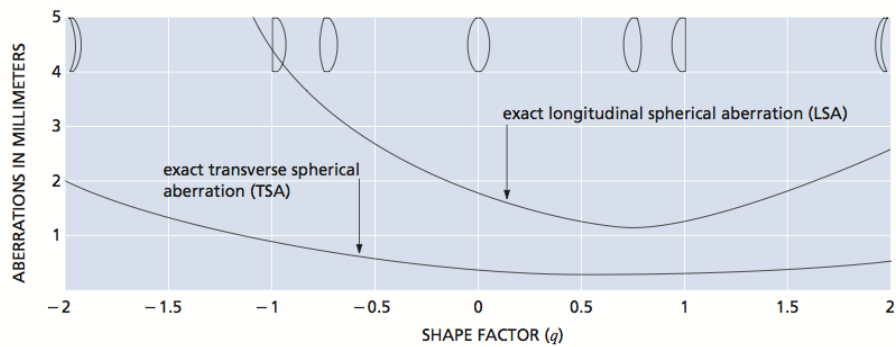


Fig. 8: Longitudinal and lateral spherical aberration²².

This plot (figure 8) suggests that a plano-convex lens (Shape factor 1) should have small aberrations. A slightly bi-convex optic (with the side facing the focus at lower curvature) should be marginally superior for small focus spot sizes. To further reduce the aberration, a lens doublet should be considered. A doublet such as a two element achromat in figure

9 can reduce the aberrations significantly and can provide the small focus spot required for laser micromachining^{21 23 24}.

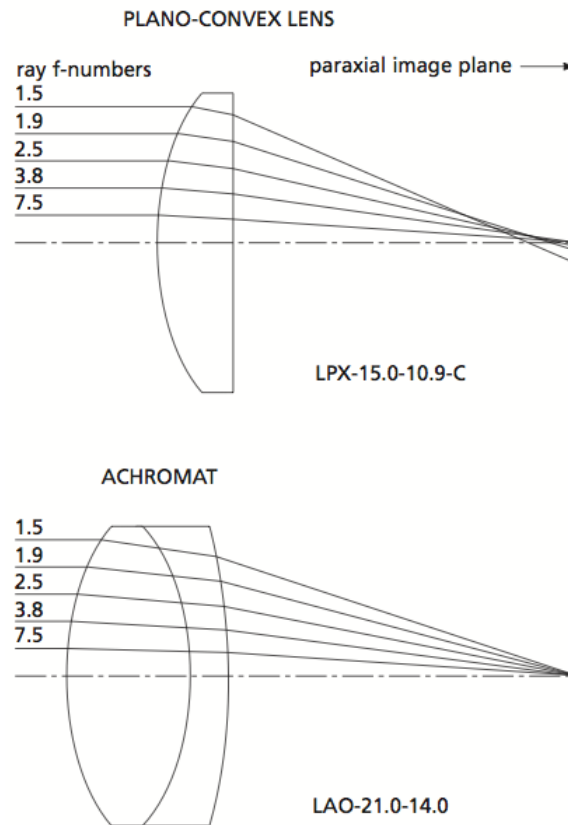


Fig. 9: single-element plano-convex lens compared with a two element achromat²².

Figure 9 also shows that small f-numbers are preferred in order to reduce aberrations. This explains why spherical aberrations become an issue for the short focal lens optics commonly used in laser micromachining.

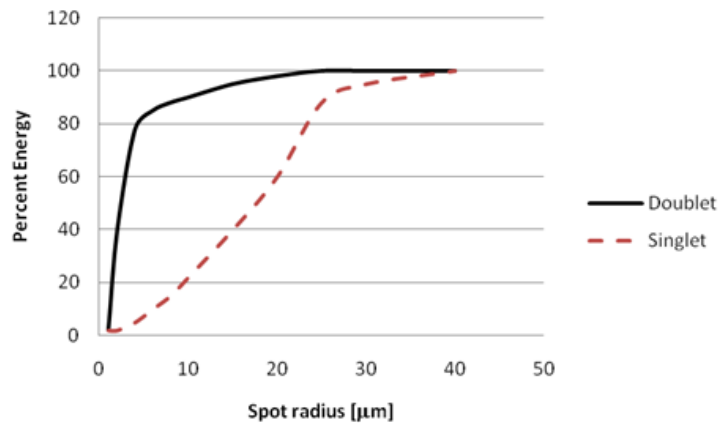


Fig. 10: Encircled energy at different radii for a singlet and doublet F/5 lenses focusing 1064 nm radiation from a Nd:YAG Laser²⁵.

Figure 10 gives an indication of how the theoretical encircled energy changes for a singlet compared to a doublet. The singlet has 80% of the energy in an approximately 50 μm spot and the doublet has 80% of the energy in an approximately <10 μm spot.

Examples of lens materials used at 1 μm wavelengths are fused silica, BaK1, SF11 and BK7 from Schott²⁶. The most commonly used material for optics for solid-state lasers at infrared wavelengths (IR-A, 700 nm to 1400 nm) is BK7 and SF11. The optics are typically coated with an anti reflective coating to improve the transmission of the laser light through the optical setup. Each optical surface can create up to 4% loss at normal incidence²⁷. An optical setup for micromachining with beam expander, focusing optic and protection glass will have at least 4 optical elements with 8 surfaces. This will create up to 32% loss if the optics are not antireflective coated. With a narrow band antireflection coating losses can be lowered to <0.25% for each surface²⁸. A good antireflection coating is particularly important for single mode fibre lasers since they are

particularly sensitive to feedback reflections that can create feedback into the laser resonator creating power spikes that can destroy the fibre laser ²⁹.

1.2.2. Laser Cutting with Solid State Lasers

There are different laser cutting processes that can be used to cut with solid state lasers. Dahotre ³⁰ et al lists four main approaches for laser cutting:

- 1.) Vaporization cutting approach by direct vaporization of the material by the laser energy.
- 2.) Fusion cutting where the laser energy melts the material and which is subsequently expelled by impinging inert gas jet.
- 3.) Reactive fusion cutting where an exothermic reaction creates an additional source of energy. The reactive gas jet removes the molten material in the form of a mixture of oxide and metal.
- 4.) Controlled fracture where energy introduces stress followed by mechanical cleaving.

Steen ³¹ lists three additional laser cutting processes:

- 5.) Cold cutting where sufficient photon energy is used to break apart the atomic structure of the material.
- 6.) Scribing where the laser creates a perforation followed by mechanical fracturing.
- 7.) Burned stabilized laser cutting where most of the energy for the cutting process is supplied by the oxygen assist gas.

This thesis investigates the use of pulsed Nd:YAG lasers and fibre lasers using processes 2 and 3 above. The fusion cutting process (also known as

the melt and blow method) or the reactive fusion process (also known as melt, burn and blow method)³⁰ are established microcutting processes for stainless steel with pulsed solid state lasers with pulse lengths in the range of 10-200 μ s.

1.2.2.1. Fusion Cutting Process

Based on a purely thermodynamic analysis for the melt-blow or fusion cutting process, the energy requirement E_{FC} is proportional to the volume of the generated kerf (figure 11).

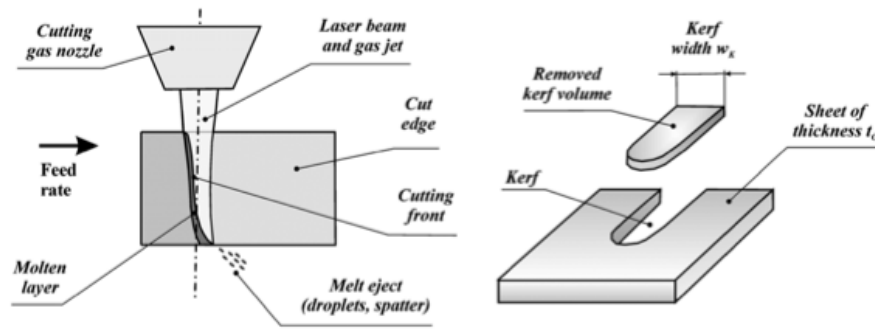


Fig. 11: Schematic diagram of fusion cutting process and resultant cut kerf geometry³².

The power requirement P_{FC} per unit time t can be calculated using the following thermodynamic relationship:

$$P_{FC} = \frac{E_{FC}}{t} = \rho \cdot w_K \cdot t_C \cdot v_C \cdot \Delta h_m \quad (1.2)$$

where ρ is the material density and Δh_m is the specific enthalpy necessary for melting the material (latent heat of melting). The material thickness is t_C , the kerf width is w_K and the cutting speed is v_C . This relationship does not consider the fraction of material that vaporized in the melt pool. Due to the small beam diameter (0.1 to 0.01 mm) and the relatively thin material

the average laser power requirement for microcutting applications is typically below 10W.

Due to the absorption coefficient A of the laser, the loss by heat conduction P_{HL} and the power that is passing through the kerf without getting absorbed P_{PT} , the laser power P_L is only partially transformed into the power P_{FC} for the fusion cutting process. The energy balance considering those factors is:

$$P_{FC} = AP_L - P_{HL} - P_{PT} \quad (1.3)$$

Multiple factors influence the laser absorption coefficient during the cutting process. The main factors are the material temperature, the surface conditions and the cut front inclination. The absorption coefficient A for stainless steel laser machining in the wavelength region 1000-1100 nm is in the range of 0.4 to 0.6^{33 34 35}.

The power loss due to heat conduction P_{HL} can be calculated with the following equation:

$$P_{HL} = 2sk(T_M - T_0)Pe \quad (1.4)$$

where s is the material thickness of the sample, k is the thermal conductivity, T_M is the melting temperature of the steel and T_0 is the room temperature.

In order to calculate the thermal diffusion, the dimensionless Peclet number (Pe) needs to be determined. The Peclet number can be defined from the following equation:

$$Pe = d v / \alpha \quad (1.5)$$

where v is the velocity or in this case the cutting speed, d is the characteristic interaction length or in this case the beam diameter $2w$, and α is the thermal diffusivity.

In laser microcutting of stainless steel with small beam diameter, the power loss by heat conduction is typically insignificant but could become significant if the laser power is not adapted to lower cutting speed conditions.

1.2.2.2. Reactive Fusion Cutting

Oxygen is the process gas used for reactive fusion cutting, and reacts exothermically with the work piece. The fraction of energy supplied by the exothermic reaction with oxygen is typically 60% for stainless steel cutting³⁶ and can be estimated by the energy released during oxidation. According to Herziger³⁵ et al., this value is 4.7 kJ/g. Kannatey-Asibu³⁷ calculates the energy contributed by the exothermic reaction with:



Since iron has a molar mass of 55 mol, each iron mole contains 55 g of iron³⁸. This results in a reactive energy of 4.5 kJ/g, supporting the value of Herziger et al.

The oxidation of iron has an effect on the viscosity of the molten material.

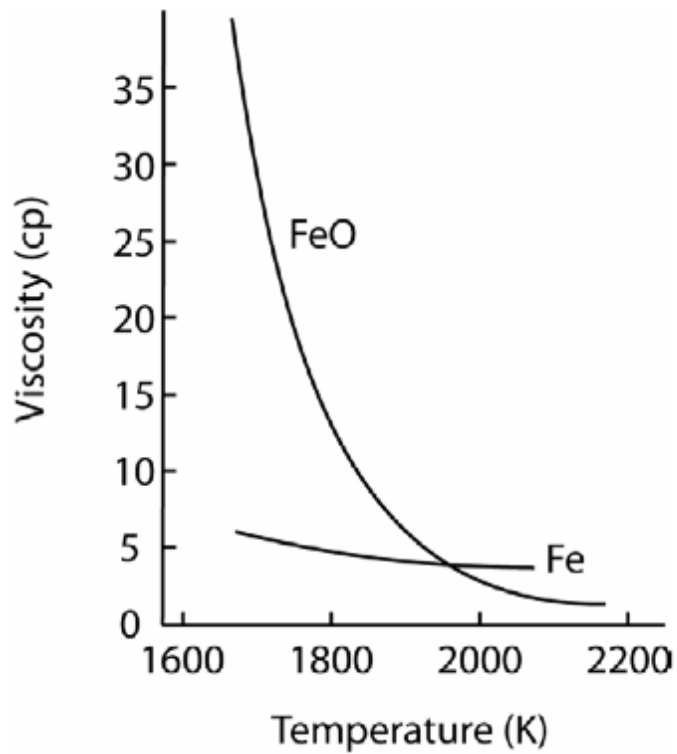


Fig. 12: Relationship between viscosity and temperature for iron and FeO³⁹.

Figure 12 shows how the Fe/FeO mixture expelled from the cutting zone has considerably lower viscosity than molten iron. This effect helps ejecting the molten material through the narrow kerf during the microcutting process⁴⁰.

1.2.3. Focus position

For best cutting results with the smallest possible spot size, the focus position needs to be optimized. Figure 13 shows that the best focus position for microcutting of stainless steel is in the centre of the material.

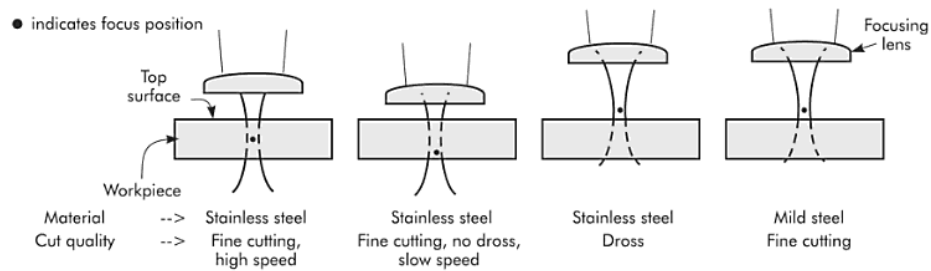


Fig. 13: Focus position and cutting quality⁴¹.

The focus position and the Rayleigh length of the laser beam influences the parallelism of the sidewalls. For a parallel cut, the material thickness should be smaller than two times the Rayleigh range. The Rayleigh range represents a distance in which the beam diameter increases by less than 40%⁴². See Chapter 2.1.7 for the calculation of the Rayleigh range R . Additionally a long Rayleigh range makes the system less sensitive for a focus position misalignment.

1.2.4. Sidewall Striation

The term striation describes ripples on the sidewalls which form during the laser cutting process. The frequency and amplitude of those ripples influences the surface roughness of the sidewalls. Depending on the process parameters, the surface roughness may also vary from the top to the bottom of the kerf.

They are several primary reasons for these striations⁴³:

- 1.) Vibrations in the motion system
- 2.) Fluctuations in laser power or pulsing of the laser system
- 3.) Fluctuations in the gas flow
- 4.) Hydrodynamics of the metal flow

5.) Side wall burning

Vibrations in the motion system, fluctuations in laser power and gas flow can be reduced or eliminated by the design of the laser and the system integration. The material, material thickness, laser parameters (for example focus size, power and pulse frequency), gas type, gas pressure, gas nozzle design, focus position and the cutting speed directly influence the hydrodynamics of the metal flow. These influences are very complex and each parameter can change the striations significantly. A complete study of all parameters would exceed the scope of this review, therefore only the major parameters and their influence on the striations will be discussed.

The striations on the sidewall in figure 14 can be separated into two areas; the cut area and the break area. The cut area typically has a uniform striation frequency. The break area shows a chaotic striation formation with increased surface roughness. Figure 14 describes the formation of striations arising from the laser cutting of stainless steel.

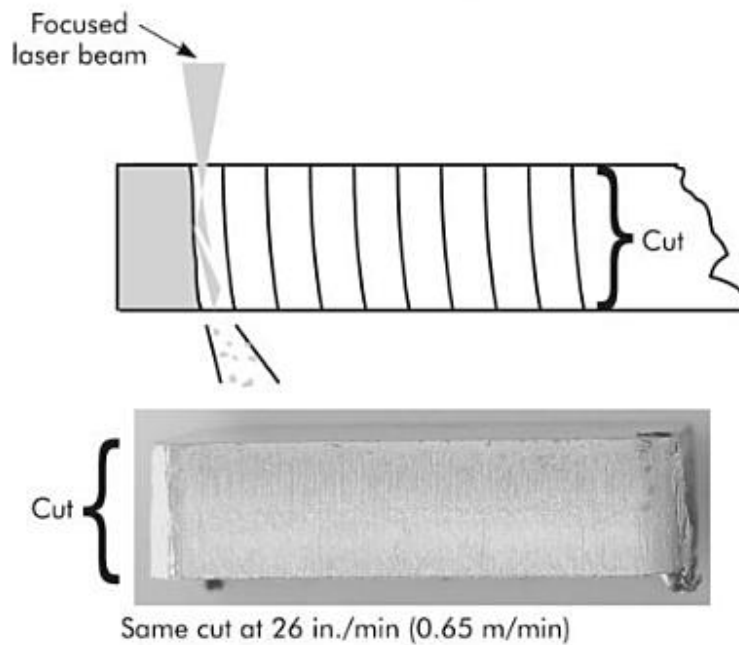
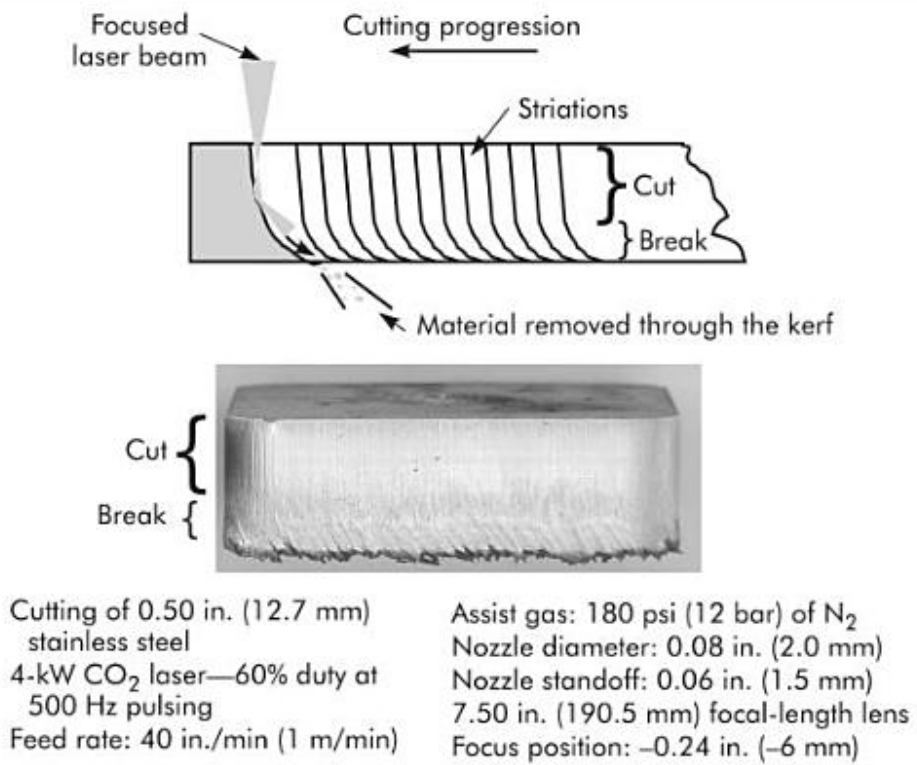


Fig. 14: Walls of the kerf show striations exhibiting cut and break sections⁴⁴.

According to Caristan⁴⁴, the laser melts and vaporizes the metal, creating the kerf. The walls of the kerf show striations exhibiting cut and break sections. The cut-to-break ratio increases when the feed rate to laser power ratio decreases. In his example, a change of cutting speed from 1 m/min to 0.65 m/min eliminates the beak section.

Figure 15 shows an example how the focus position and cutting speed changes the pattern of the striations.

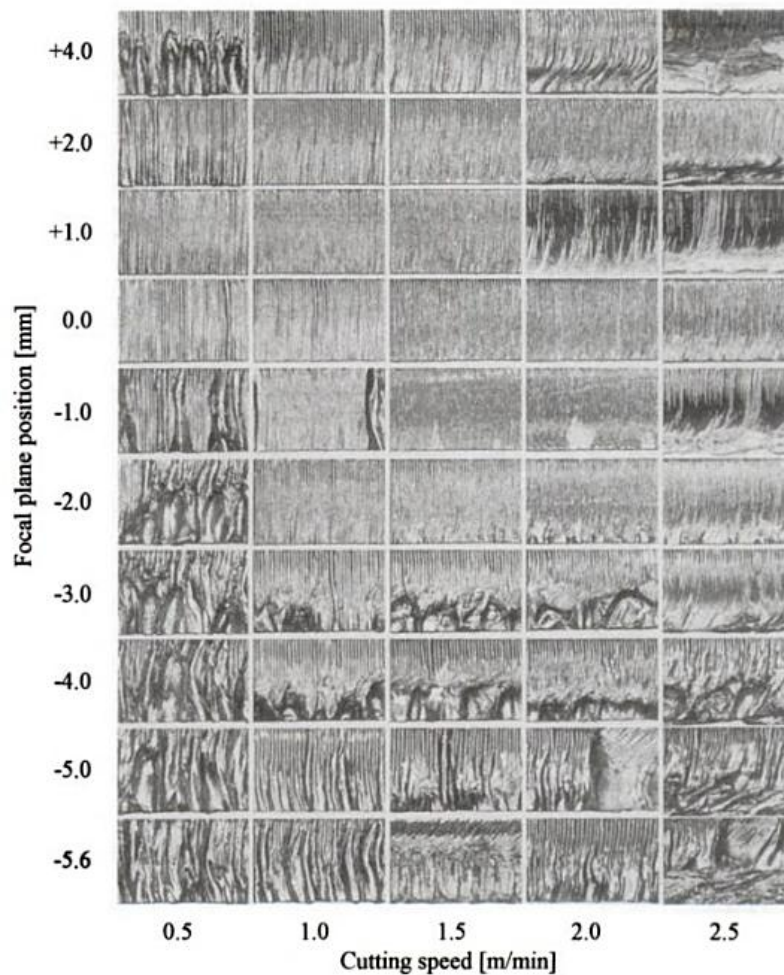


Fig. 15: Cut surface of 6 mm thick oxygen cut mild steel as a function of speed and focal plane position, cut with 1.5 kW CO₂ laser at 3 bar⁴⁵.

The images in figure 15 suggest that processing with the laser focus in the center of the material and low to medium processing speeds create striation patterns with a better surface quality.

The pulsed laser cutting process can also introduce striations due to the low pulse-to-pulse overlap at high cutting speed or low pulse-to-pulse frequency.

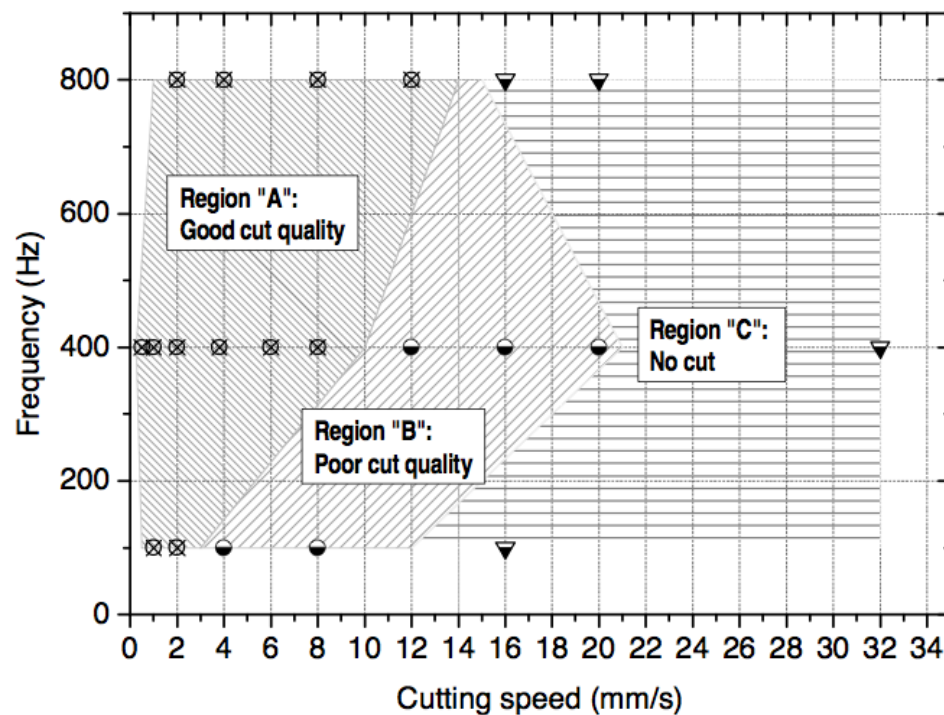


Fig. 16: The effect of cutting speed on cut quality at various pulse frequencies⁴⁶.

Figure 16 shows the microcutting results for a pulsed Nd:YAG laser with 20-50 mm kerf at different cutting speeds and frequencies. The material used for the experiments was 304 steel with a material thickness of 0.4 mm.

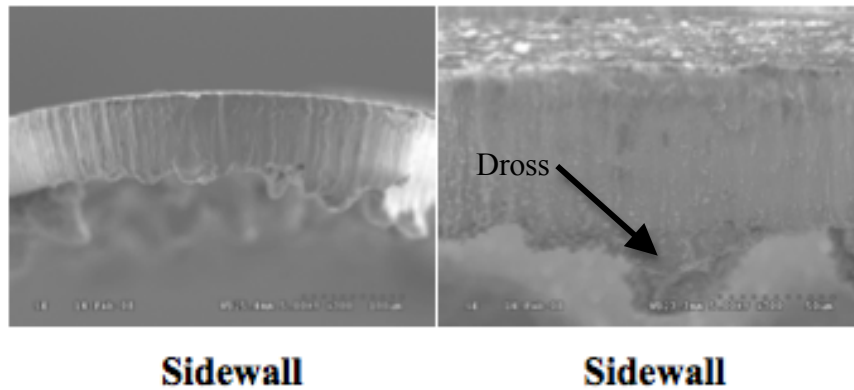


Fig. 17: Sidewall of stent patterns with dross at the bottom of the cut⁴⁷.

On the bottom part of the kerf, the molten material will cool off and can form dross or burrs (figure 17). In most cases this dross needs to be removed in post processing steps. Processing parameters that can reduce the dross are of interest. The two parameters that have a beneficial impact on the dross formation during fusion cutting are the cutting speed and the assist gas pressure⁴⁸.

1.2.5. Laser Microwelding with Solid State Lasers

As with laser cutting, laser welding is a process where a focused laser beam interacts with a moving work piece. The energy of the laser beam is absorbed at the surface and a melt pool forms. The material re-solidifies after the laser beam has passed. Typically, the process area is shielded from oxidation by an inert gas (figure 18). The weld process is influenced by parameters such as laser power, laser wavelength, spot size, weld speed and shield gas. There are two fundamentally different concepts of laser welding interaction; the conduction welding process and the keyhole welding process.

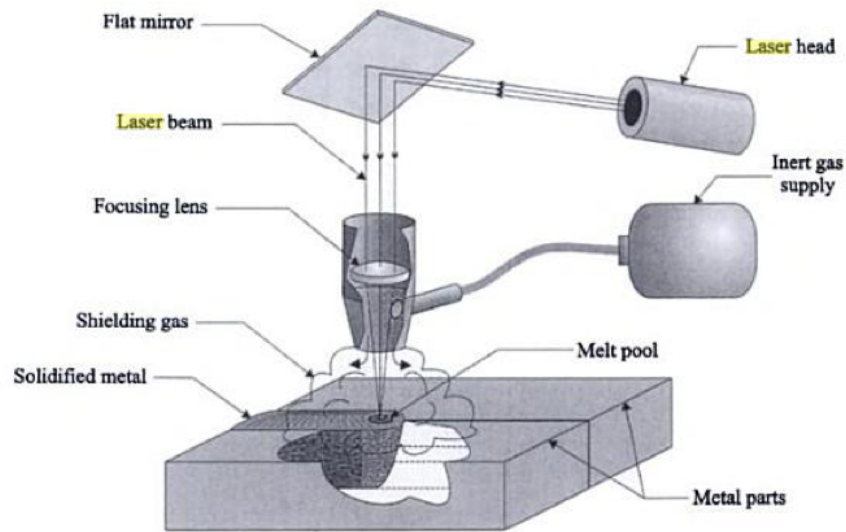


Fig. 18: Laser welding⁴⁹.

1.2.5.1. Conduction Laser Welding

The conduction welding process takes place at relatively low laser power and intensities that are typically below 10^3 W/mm^2 ⁵⁰. The absorption coefficient of the material determines the fraction of the laser energy absorbed by Fresnel absorption on the surface. The absorption coefficient for steel in the $1 \mu\text{m}$ wavelength region is of the order of 0.4-0.6. At the start of the welding process only a thin layer of material is responsible for the absorption of the laser energy. The laser energy is converted into heat and conducted into the depth of the material. The geometry of a conduction weld is wide and shows relatively low penetration as shown in figure 19. The aspect ratio of weld depth to width is typically below 1.

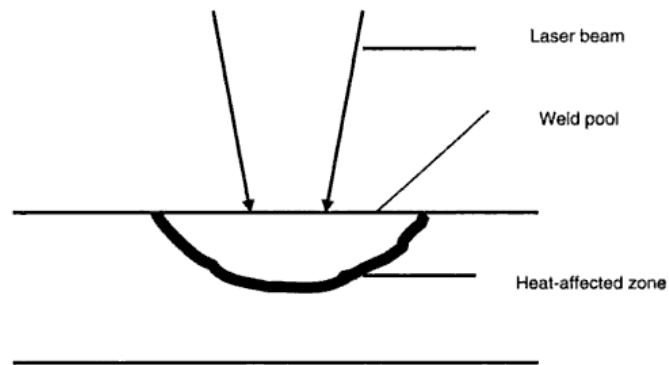


Fig. 19: Conduction Laser Welding.

According to Steen⁵¹ low power density which is insufficient to cause boiling at a given welding speed is the reason for not forming a keyhole during the conduction welding process. The weld pool has strong stirring forces driven by Marangoni type forces resulting from variations in surface tension with temperature.

1.2.5.2. Keyhole Laser Welding

At power density levels above 10^3 W/mm^2 ⁵⁰ keyhole welding can occur. The molten material will start to evaporate and create a hole in the melt pool (figure 20). The hole will stabilize due to the vapor pressure generated in the laser focus. Miyamoto reports that keyhole welding in microwelding will typically start at power densities two orders of magnitude higher.

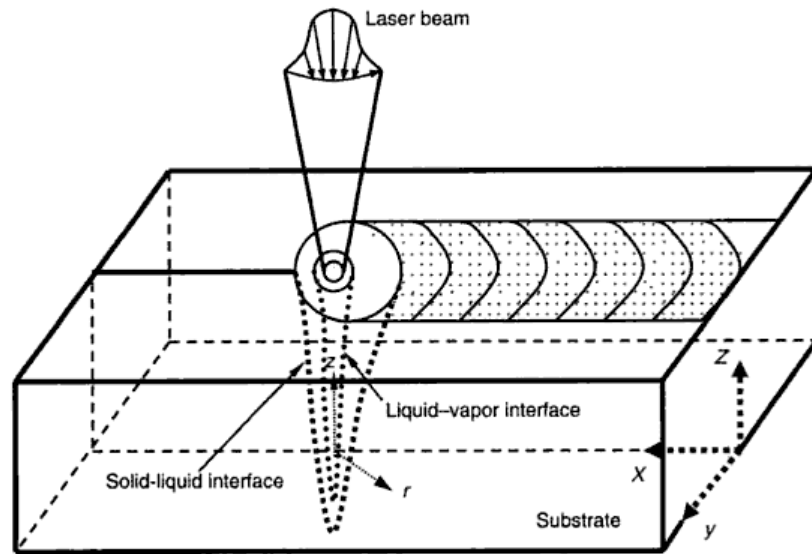


Fig. 20: Keyhole Laser Welding⁵².

The keyhole can extend over the complete depth of the work piece. Multiple reflections of the laser beam in the keyhole and absorption in the vapor due to inverse Bremsstrahlung increases the absorption above 80%⁵⁴. The keyhole welding process enables weld depths that are significantly larger than the width of the weld.

1.2.5.3. Microwelding Laser Parameters

Lasers with small beam diameters and good beam quality enable microwelding applications. The small spot size of single mode lasers allows conduction and keyhole welding at relatively low average power levels. Toenshoff et al.⁵³ showed conduction microwelding results with a 9W continuous wave (CW) fibre laser with a spot size diameter smaller than 25 μm . Miyamoto et al. presented an ultrafine keyhole welding process with a 40W single mode fibre laser⁵⁵.

Pulsed operation allows the power density to stay above the threshold for conduction or keyhole welding and maintain weld depth. It allows

lowering the average laser power in cases where the work piece is sensitive to average power.

As in any other laser welding process, the laser processing parameters such as laser power, focus spot diameter and weld speed influence the micro weld geometry.

According to Herziger et al. the following energy balance equation can be used to model the weld penetration:

$$P_L = P_1 + P_2 + P_3 + P_4 + V \quad (1.7)$$

where P_L is the laser power absorbed by the material

P_1 is the power necessary to heat the volume of the vapor capillary to the vapor temperature

$$P_1 = \rho C_p \Delta T 2r_w t_s v_s \quad (1.8)$$

where ρ is the material density, C_p is the specific heat, $2r_w$ is the focus diameter, t_s is the weld depth and v_s is the welding speed, ΔT is the temperature difference between ambient and vaporization temperature

P_2 is the power necessary for melting the material volume in the capillary.

$$P_2 = \rho \Delta h_m 2r_w t_s v_s \quad (1.9)$$

Where Δh_m is the latent heat of melting.

P_3 is the power necessary for vaporizing the material volume in the capillary.

$$P_3 = \rho \Delta h_V 2r_w t_s v_s \quad (1.10)$$

Where Δh_V is the latent heat of vaporization.

P_4 is the energy loss due to heat conduction from the capillary.

In microwelding, the thermal mass of the region being welded is small enough that conduction is not significant ($P_4 \approx 0$) and most of the absorbed energy is converted to heat within the weld volume⁵⁶.

V is the power loss due to the absorption losses in the vapour plume. For this calculation we assume a complete coupling of the laser power into the process capillary ($V \approx 0$).

Following this analysis, the laser power absorbed by the material is almost proportional to the volume of capillary.

$$P_L \sim v_s 2r_w t_s \rightarrow \frac{P_L}{r_w v_s} \sim t_s \quad (1.11)$$

This relationship is valid for cylindrical beam propagation and can be used to estimate the weld penetration.

The other weld dimension that is of interest is the weld width, but according to Herziger the weld area cross section is more meaningful in regards to the weld performance. Based on (1.11) the melted cross section is directly proportional to the linear laser energy.

$$A \sim \frac{P_L}{v_s} \quad (1.12)$$

In summary, the key factors that determine the weld geometry for a laser welding process are the spot size, the laser power and the speed. The use of a small focus spot should therefore translate into finer weld geometries necessary for microwelding.

Based on the Rosenthal⁵⁷ solution for the moving line source, Steen⁵⁸ has developed an analytic model that can be used for keyhole welding. The model uses the heat transfer analysis by Swift-Hook and Gick, which indicated that for keyhole welding only 48.3% of the absorbed energy is used for melting. The rest of the energy is lost to conduction.

$$0.483 P_L = v_S 2r_W t_S \rho C_P T_M \quad (1.13)$$

where $2r_W$ is the weld width

This model assumes an ultimate fine focus and could be of interest for microwelding with small spot sizes. The fraction of energy used for melting will decrease at lower welding speeds.

1.3. Gas Nozzles for Laser Micro Processing Application

There are two fundamentally different nozzles for laser machining: the laser cutting nozzle and the laser welding nozzle. The laser cutting nozzle needs to supply inert or reactive gas into the kerf. Additionally, the cutting nozzle needs to supply gas with enough shear force to eject the molten material out of the kerf. The role of the laser welding nozzle is to cover the welding area with a blanket of inert gas. Due to the smaller processing area the nozzle orifice can be smaller for micromachining applications.

1.3.1. Laser Cutting Nozzle

The nozzles for laser cutting are typically operated in the pressure range of 1 to 20 bar. Starting at 0.89 bar oxygen gas pressure, the flow will be

supersonic at the nozzle exit. For argon, the pressure needs to be at 1.05 bar to reach Mach 1 at the exit of the nozzle⁵⁹.

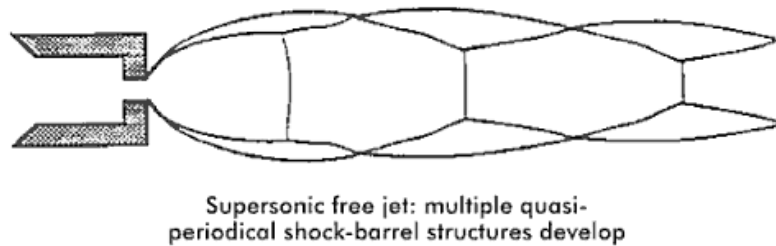
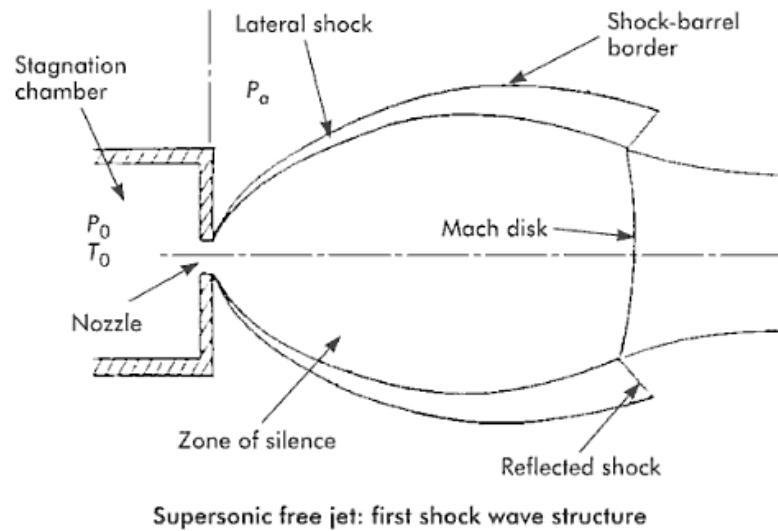


Fig. 21: Supersonic flows colliding with matter always generate at least one shock wave. In free jets, a shock-barrel structure contains a silence zone isolated from ambient atmosphere by a lateral shock barrel and a front shock called Mach disk⁶⁰.

The nozzle standoff should be shorter than the distance to the position of the first Mach disk (see figure 21). A distance of 90% of the nozzle diameter is recommended⁶¹.

Another parameter important for the cutting performance is the purity of the oxygen during laser cutting.

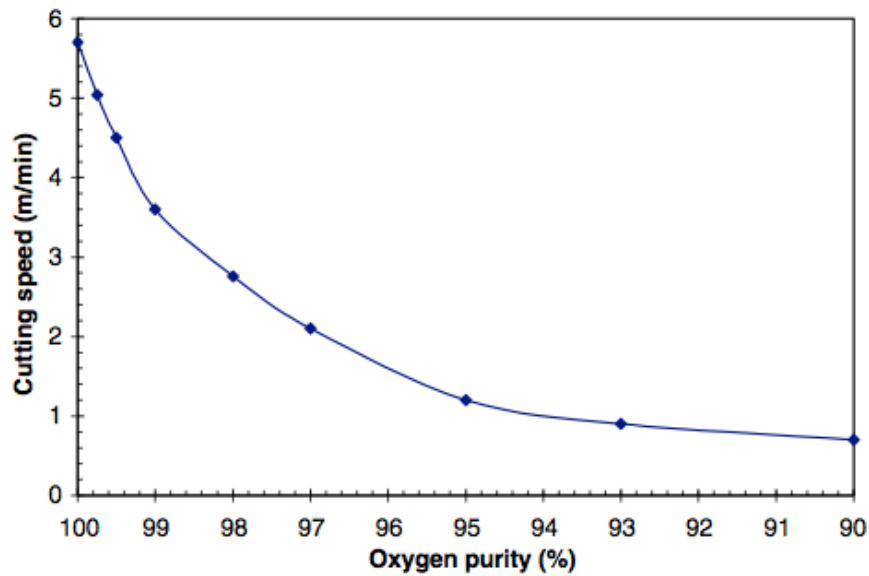


Fig. 22: Cutting speed as a function of oxygen purity in 3 mm mild steel, 1kW fibre laser, 3 bar, ⁶².

As shown in figure 22, the influence of the oxygen purity is significant; for example a 3% drop in purity will reduce the cutting speed by 50%.

1.3.2 Laser Welding Nozzle

The welding nozzle operates at significantly lower pressure and flow rate compared to the cutting nozzle. The nozzle can be off-axis or co-axial with the laser beam. The assist gas pressure and flow needs to be set low enough to avoid Venturi effects that could pull air and oxygen into the process zone. It is important that the assist gas cover extends throughout the active region where the hot or molten material could still oxidize. In many cases back shielding with a second assist gas nozzle is necessary.

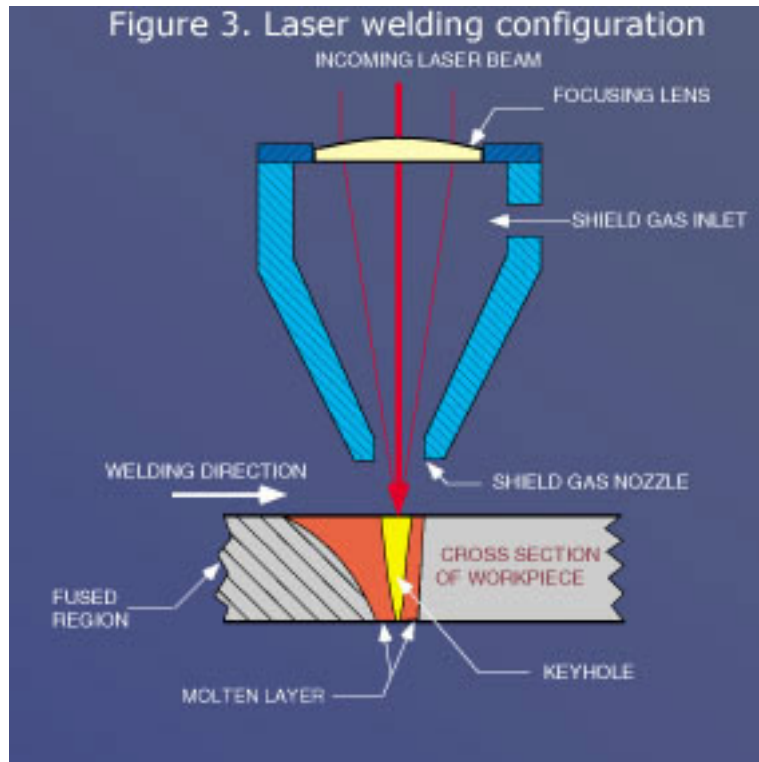


Fig. 23: Laser welding configuration with co-axial shield gas nozzle⁶³.

Argon, helium, CO₂ and nitrogen are commonly used as shielding gas. The use of nitrogen should be avoided for titanium welding, because titanium is highly reactive with nitrogen and can cause embrittlement⁶⁴.

Some mixtures of helium, argon and CO₂ improve the efficiency of the laser and increase the weld penetration. The mixtures are optimized to reduce the plasma in the process area and hence reduce the absorption of laser power in the plasma, resulting in an increased weld performance⁶⁵.

1.4. Lasers for Micromachining Investigated for this Thesis

The two different laser technologies that are investigated in this thesis are the lamp pumped Nd:YAG laser and the fibre laser. The following is a literature review of those two different lasers.

1.4.1. Flash lamp pumped Nd:YAG Lasers

There are many active materials that can be used in a solid-state laser, including Nd:YAG, Nd:YVO, Nd:Glass or Titanium Sapphire⁶⁶. Conventional laser micro-machining systems in medical device manufacturing use lamp pumped Nd:YAG lasers. Nd:YAG is an acronym for neodymium doped yttrium aluminum garnet. In a Nd:YAG laser crystal, around 1% of the yttrium is substituted with rare earth neodymium (Nd), which is the lasing material. These lasers typically emit light at a wavelength of 1064 nm⁶⁷, though they can also operate on several additional transitions with lower efficiency. The wall plug efficiency is typically in the order of 2-3%⁶⁹. Most pulsed solid-state lasers require flash lamps to pump the doped crystal, which typically have a limited life time⁶⁷.

The optical resonator is formed by the highly reflective mirror, the output mirror and the Nd:YAG crystal (see figure 24). A mode aperture limiting the lasing modes can be included into the resonator to improve the beam quality.

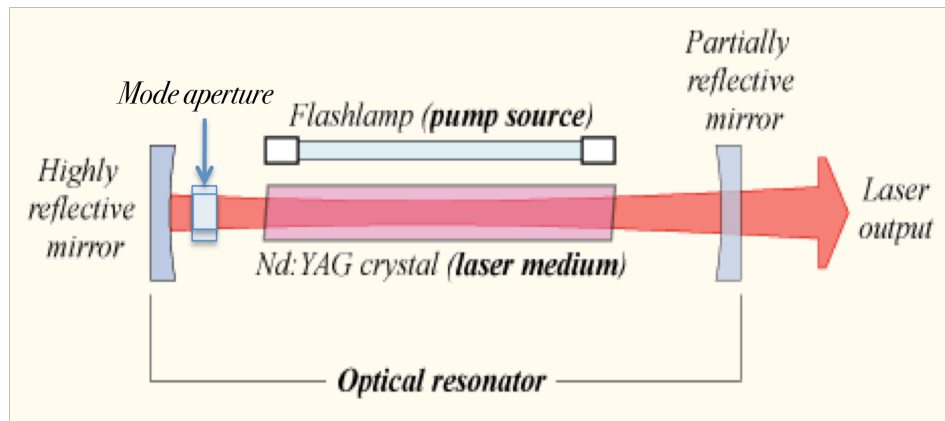


Fig. 24: Schematic diagram of flash lamp pumped Nd:YAG Laser⁶⁸

The optimum mode of operation for micromachining is the TEM₀₀ or diffraction limited operation because it enables the smallest spot size^{70 71}.

TEM is an acronym for Transverse Electromagnetic Mode. Figure 25⁷² shows an irradiance distribution of a TEM₀₀ beam⁷².

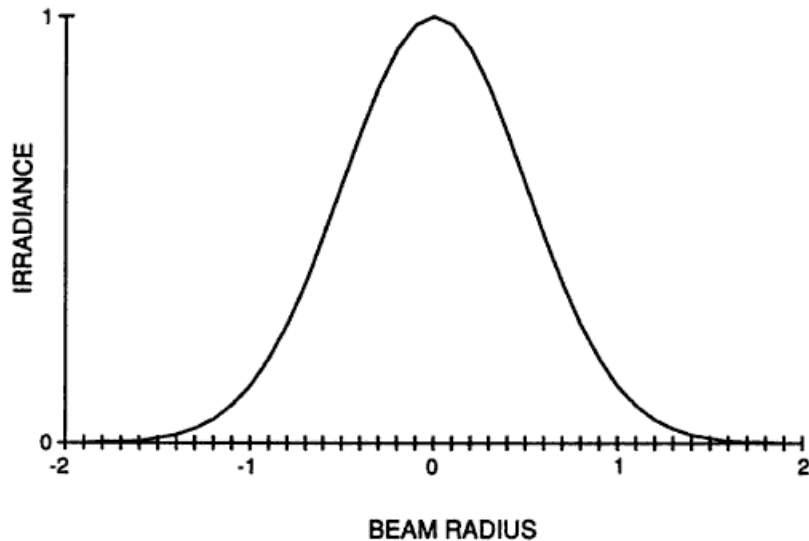


Fig. 25: Irradiance Distribution in a TEM₀₀ beam⁷²

Koechner⁷³ describes the main factors for the beam quality of a laser: the resonator length, the mode size in the active material (Nd:YAG crystal), the pump power and the resulting thermal lens, the aperture size and the curvature of the resonator mirrors.

Another factor that influences the beam quality of an Nd:YAG laser is the thermal load on the crystal. The energy of the pump source will heat the crystal. A cylindrical laser crystal with internal heating from the pump source and surface cooling will have a radial temperature gradient. This temperature gradient creates a thermal lens. The focal length of this positive lens varies with pump power. According to Koechner⁷³, the TEM₀₀ mode volume is reduced by the focusing action of the cylindrical crystal and by thermal aberrations of the Gaussian wave front in the presence of thermal lensing. The resonator design can compensate for

different thermal lensing conditions, but only for a given pump power. For a fixed resonator configuration the power in the lasing TEM₀₀ mode will not necessarily scale linearly with pump power. Higher order resonator modes become above threshold and compete with the TEM₀₀ mode. Those higher modes will cause a change in focus spot size and therefore change the machining results. The thermal lensing can get to a level where the resonator becomes unstable and the output power of the laser diminishes.

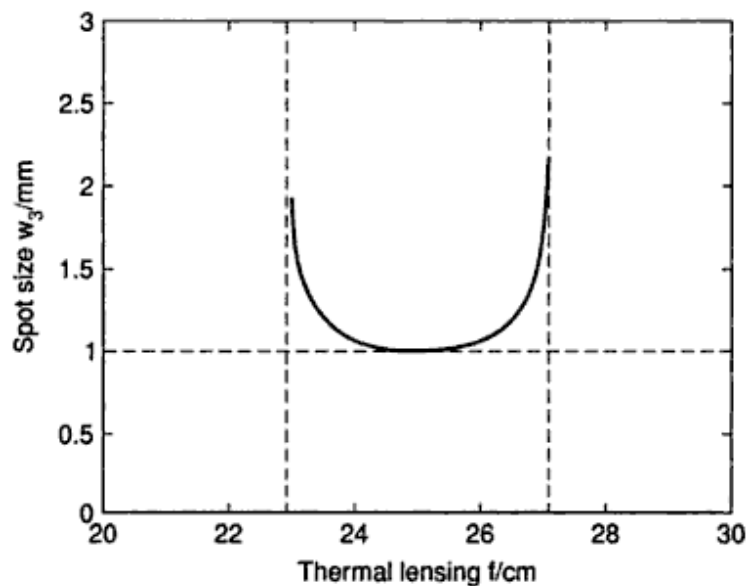


Fig. 26: Fundamental mode dimensions inside the laser rod as a function of focal length of the thermally induced lens⁷³.

Figure 26⁷³ shows how the mode dimensions are changing with the thermal lensing effect. This example of a concave-convex resonator is only stable when the focal length of the thermal lens is between 23 cm and 27 cm. Higher or lower thermal lensing will make the resonator unstable. Even in the stable region between 23 cm and 27 cm the mode size will change significantly. This fundamental behavior is typical for all standard Nd:YAG laser resonators.

According to Hall⁷⁴, a typical lamp pumped Nd:YAG laser resonator operating at 1.064 μm and optimized for TEM₀₀ needs to be approximately one meter long. Such a long resonator is sensitive to mirror misalignment. Koechner⁷⁵ describes how the resonator length affects the sensitivity of the mirror position for a laser resonator with mirrors. In figure 27 the normalized mirror radius is the mirror curvature R divided by the resonator length L. Hall⁷⁴ also states that in general the beam quality of a YAG laser varies with output powers.

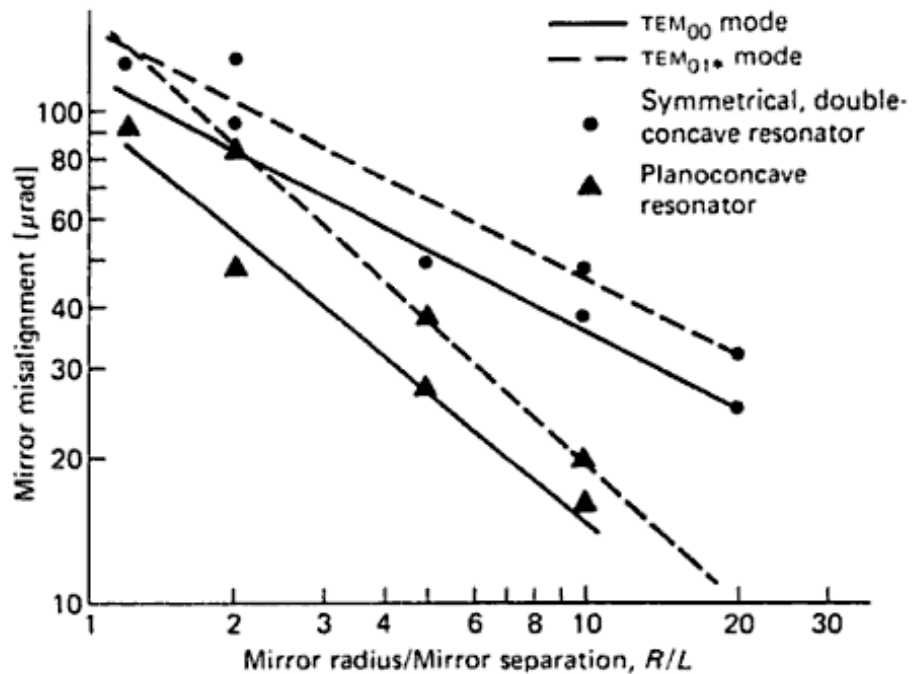


Fig. 27: Mirror misalignment in an argon laser that will produce 10% drop in output power versus normalized mirror radius.⁷⁵

All these factors: wall plug efficiency, lamp life time, thermal lensing, alignment sensitivity and beam quality stability at different power levels are important for the TEM₀₀ operation of a laser. In many cases stable TEM₀₀ operation of a lamp pumped Nd:YAG laser is very difficult to maintain in a production environment. A laser system that could reduce the

sensitivity to these factors would be beneficial for production in the medical device industry.

1.4.1.1. Lamps for Pumping Solid State Lasers

The use of lamps for pumping a solid-state laser has two significant limitations that are important for the use in an industrial environment; lifetime and efficiency. In order to understand the limitation a review of the lamp technology is necessary. There are two fundamentally different lamps for lamp pumped lasers; flash lamp for pulsed solid-state lasers and arc lamps for continuous wave lasers. The design of both lamps is nearly identical. Figure 28⁷⁶ shows the construction of an arc lamp. Two tungsten rods provide the electrical connection between the power supply and the anode or cathode respectively. The lamp is filled with a noble gas and sealed. The tungsten anode and cathode will shrink down with the use of the lamp over its lifetime.

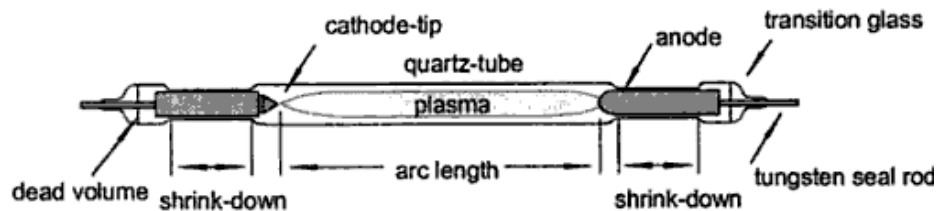


Fig. 28: Typical design of an arc lamp⁷⁶

According to Ifflaender⁷⁶, the operation of lamps can be divided into three phases: The first phase is the ionization where a high voltage is creating a sufficient number of free charge carriers. This phase is followed by the expansion of the plasma to form a stable simmer arc. The last phase is at operation current where at increased lamp current the arc expands until it nearly fills the inner diameter of the quartz tube. The operation current can be supplied in pulsed or cw-mode.

Koechner⁷⁷ notes that end of life for lamps can occur in two modes, catastrophic and nondestructive failures. The catastrophic failure can be contributed to an explosion of the quartz tube due to the shock wave in the gas when the lamp is fired, or to excessive thermal loading. The nondestructive failure is a gradual decrease of light output to a level that is below the necessary requirement of the application. The erosion of the electrodes and the gradual buildup of deposits in the quartz tube cause the reduction of the light output. When operated within the rated pulse or average power the lamps typically fail by nondestructive failure mode. Nevertheless the useful lifetime of a lamp is 500-1000 hours.

The limitation in total efficiency can be illustrated by comparing the emission spectrum with the absorption spectrum of the solid-state laser crystal. The two most commonly used noble gasses used in lamps are xenon and krypton. Krypton is typically preferred due to the better match of the emission and absorption spectrum. The limitation in pump efficiency can be illustrated by plotting the fractional utilization of the krypton lamp spectrum by the Nd:YAG crystal over the pumping path (figure 29).

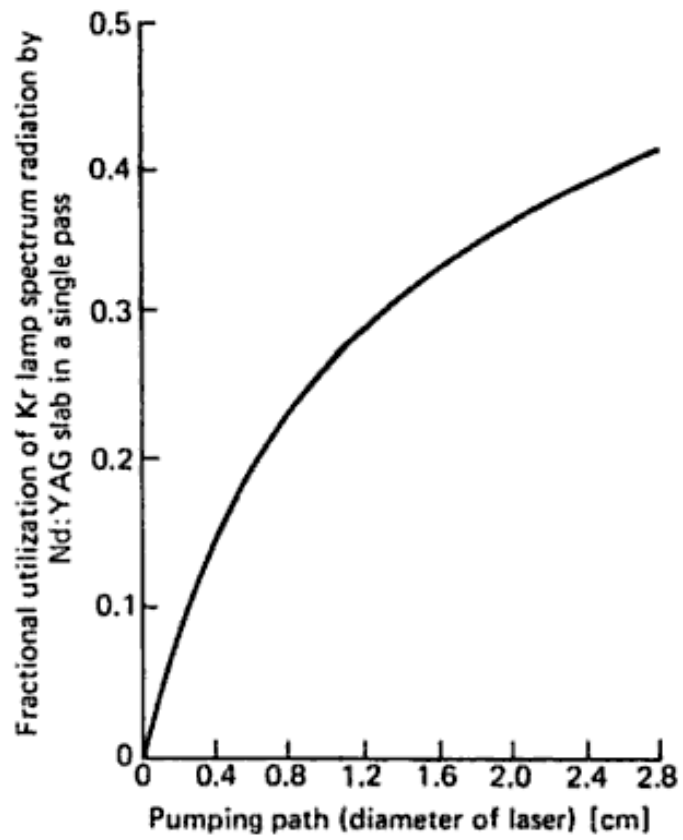


Fig. 29: Fractional utilization of krypton lamp output by Nd:YAG⁷⁵

Koechner⁷⁵ reports a radiation output to electrical efficiency of 45%. The overall efficiency of a lamp pumped Nd:YAG laser is therefore between 2 and 3%.

1.4.2. Diode Pumped Fibre Lasers

The fibre laser technology has the potential to address the factors that limit the use of a lamp pumped Nd:YAG laser in a production environment. At the beginning of Guidant's fibre laser program in 2000, the maximum commercial available power of fibre lasers was in the range of 10-50 W. At that time, fibre lasers were not used for industrial micromachining applications. As previously stated the results shown in this thesis are the first published microcutting results for industrial application with fibre lasers. The following review describes the concept and some of the key features of a fibre laser. The single-mode fibre laser is of special interest because only the fundamental spatial mode will propagate through the fibre by design. The fundamental spatial mode in a fibre is equivalent in beam quality to a TEM₀₀ mode in a free space resonator. The single-mode fibre will not support any higher order modes.

The first fibre lasers used Nd-doped glass fibre as an active medium. They were pumped transversely by coiling the fibre around a flash lamp. Later, end pumping was successfully demonstrated with fibre coupled diode lasers. Ytterbium⁷⁸ doped glass was used to achieve higher laser efficiencies. Duling⁷⁹ et al. demonstrated single mode operation by using a single mode fibre. Duling used free space mirrors to build the resonator. Meltz⁷⁹ et al used an intracore Bragg phase grating to get feedback into the resonator. The intracore Bragg phase grating substituted the resonator mirror and therefore eliminated the alignment sensitivity of single mode laser operation. Early fibre lasers used standard single-clad fibres (figure 30). For a single-clad fibre all the pump light needs to be coupled into the core of the fibre.

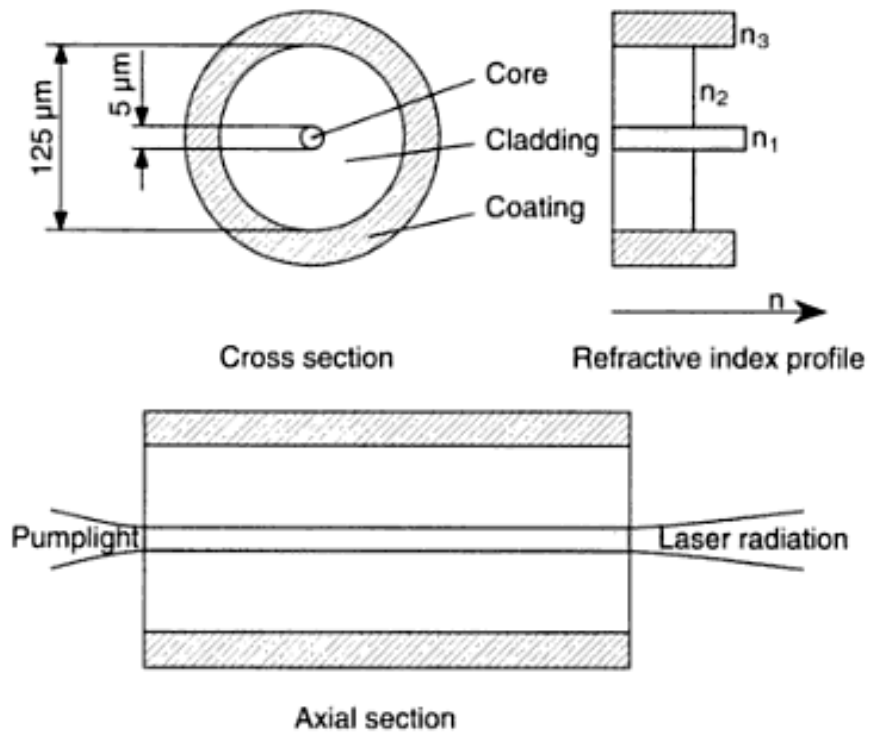


Fig. 30: Single-clad fibre laser geometry. The rare-earth active core is surrounded by a cladding and a polymer coating⁸⁰

The power from single clad fibre lasers is limited by the amount of pump power that can be coupled into the core of the fibre. In order to scale to higher laser power the area into which the pump light can be coupled must be increased. The double-clad fibre made it possible to get several tens of Watts of output power for the first time⁸⁰. Figure 31 shows the geometry for a double clad fibre.

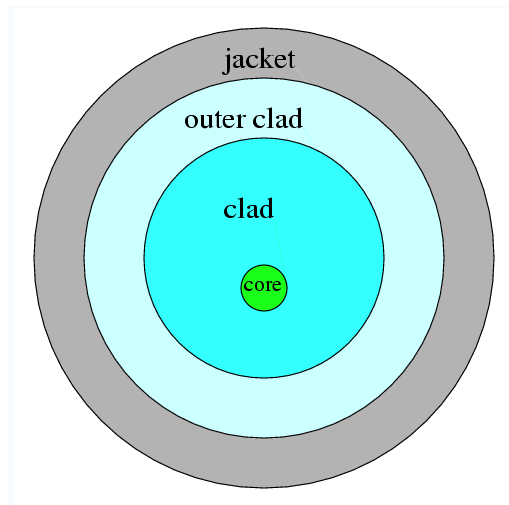


Fig. 31: Double-clad fibre laser geometry. The rare-earth active core is surrounded by a cladding, outer clad and a polymer jacket⁸¹.

A double clad fibre consists of a single mode core which is surrounded by a multi mode guided region. The single mode core confines the laser modes and the double clad surrounding confines the pump light. The multi mode cladding region typically has a much larger area and numerical aperture allowing significantly more pump light to be coupled into the fibre. As the pump light propagates down the inner cladding, it crosses through and is absorbed in the active core. Figure 31 shows the doped core off centre. This design improves the absorption of helical rays of pump light in the inner core⁸⁰. The use of rectangular large size inner claddings serves the same purpose. The diameter of the inner cladding is up to a few hundred micrometers and typically has a numerical aperture of 0.4 to 0.7⁸²
83.

The total reported wall-plug efficiency for commercial fibre lasers is significantly higher than lamp pumped Nd:YAG lasers. Leading fibre laser manufacturers produce fibre lasers with wall-plug efficiencies up to 35%⁸⁴
85. Reasons are the high slope efficiency of fibre lasers (up to 80%⁸³) and

the high optical-electrical efficiency of a pump diode laser (typically up to 60%⁸⁶).

The two most commonly used pumping concepts for modern high power fibre lasers are end pumping and side pumping such as the evanescent field pumping. The end-pumped configuration can be realized by free space coupling of the pump diodes into the fibre laser or by splicing fibre coupled diodes into the fibre laser.

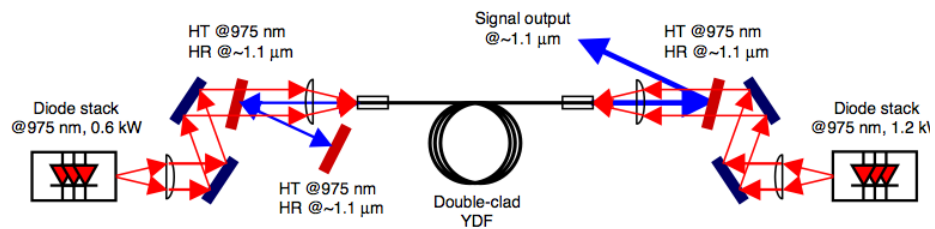


Fig. 32: Fibre Laser arrangement with free space two diode-stack pump sources. HR: high reflective, HT: high transmission⁸⁷.

The setup in figure 32 shows a high power free space fibre laser configuration that enabled up to 1.36 kW continuous wave (cw) single mode laser output at 1100 nm. The configuration is pumped with 1.8 kW diode laser power at 975 nm⁸⁷. The free space coupled diodes have the disadvantage of some alignment sensitivity of the pump diodes to the double clad active fibre.

Figure 33 shows a setup that solves the alignment sensitivity of the pump diodes to the double clad fibre. A number of fibre coupled diodes are combined using a fibre multimode combiner and spliced to both ends of an active fibre. Fibre Bragg gratings are used to form the laser resonator. The Bragg gratings are designed to reflect the fibre laser light, but to transmit

the pump laser light. This configuration enables single mode output laser power levels in excess of 5000W⁸⁸.

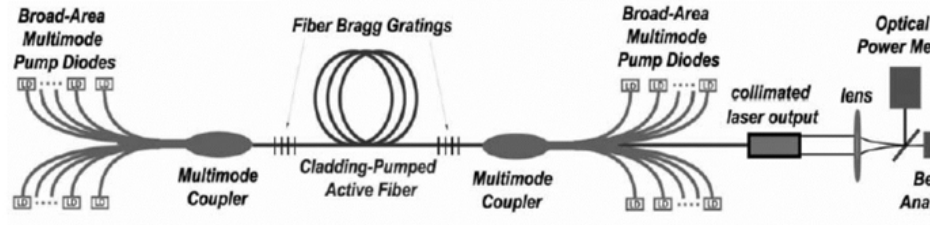


Fig. 33: Fibre Laser arrangement end-pumped with spliced couplers and fibre coupled diodes⁸⁸.

The evanescent field pumping uses a different concept to couple pump power into the fibre. The concept is illustrated in figure 34.

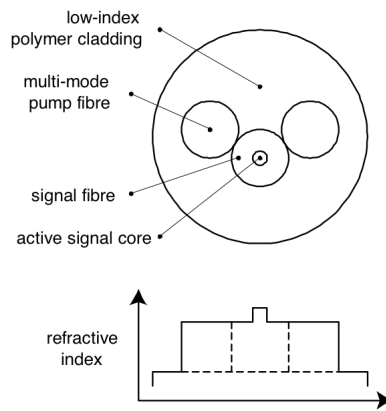


Fig. 34: Concept of a GT wave fibre⁸⁹.

The evanescent field pumped fibre (also called GTWave fibre, trade mark of SPI) is a structure that comprises an active double-clad fibre in contact with one or more multi-mode pump fibres. The diode laser pump light is launched into the multi-mode pump fibres. After a few centimeters, evanescent coupling will distribute the pump power evenly between the

pump fibres and the double-clad fibre. As with end-pumping, the pump light will be absorbed by the active core along the length of the fibre. The asymmetric structure of the fibre enhances the absorption by the doped active fibre. The GTWave fibre concept benefits the manufacturability of the fibre laser, as the pump light and the signal light are in different physical fibres when the polymer cladding is stripped off. The multi-mode pump fibres can be directly spliced to a fibre coupled diode pump, the signal fibre can be fitted with Bragg gratings or other fibre optic components as necessary. This allows easy scaling to multi kW output powers⁸⁹.

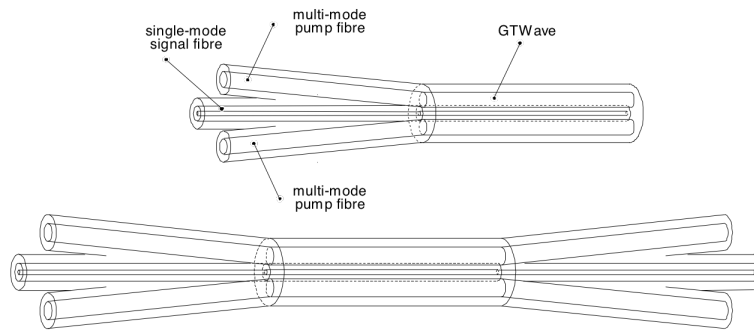


Fig. 35: Structure of an evanescent field pumped fibre laser⁸⁹.

Figure 35 shows how the fibre is broken out into two multi-mode fibres that can be pumped on four ends by fibre coupled laser diodes.

1.4.2.1. Laser Diodes for Pumping of Fibre Lasers

The diodes used by a fibre laser have the same role as the lamps used in a lamp pumped solid state laser. They provide the pump energy for the lasing media. In 1964 it was suggested by Newman that GaAs LED's could be used to excite Nd: CaWO₄ lasers. The first diode pumped laser was demonstrated by Keyes and Quist in 1964⁹⁰.

Laser diodes convert electrical to optical power in a semiconductor waveguide. Compound materials used for semiconductor lasers are for example gallium arsenide, indium phosphate and gallium nitride. In the active region (I region figure 36) electrical power initiates and maintains an electron and hole population.

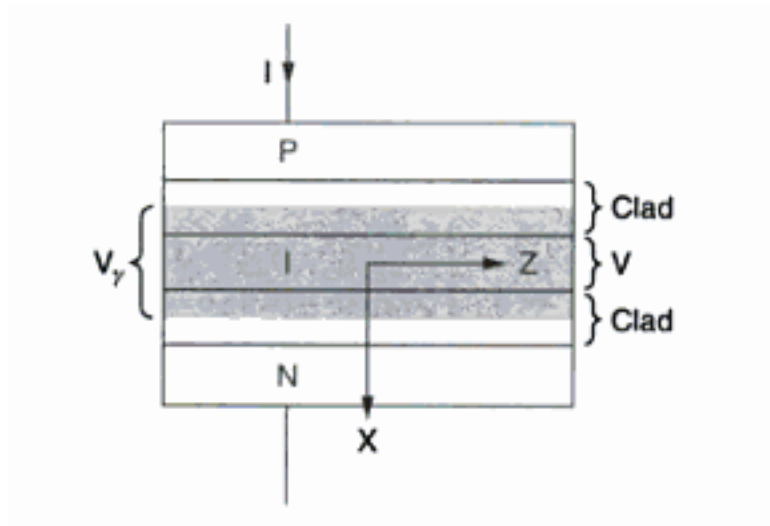


Fig. 36: Structure of a semiconductor laser

The recombination of holes and electrons in the active region generates photons. Spontaneous emission initiates laser oscillation between the two mirrored end faces (in the X-Z plane of figure 36) of the diode structure. This leads to optical amplification where laser radiation escapes through the partial reflective mirror of the diode structure.

Typical electrical to optical efficiency of commercial laser diodes for fibre laser pumping applications can be up to 60%⁸⁶. The remainder of the electrical power needs to be cooled away from the diode laser structure to avoid damage from the heat to the diode and the diode assembly.

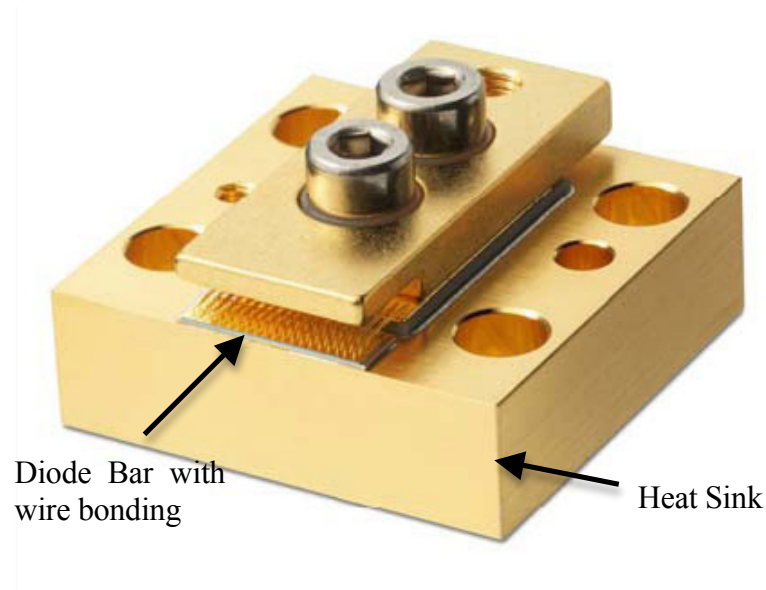


Fig. 37: Laser diode mounted on heat sink (Bookham Product information).

Figure 37 shows a diode laser bar mounted on a passive heat sink. The diode is soldered to the edge of a heat sink and provides one electrical contact. The wire bonding on top of the diode provides the second electrical connection. Some high power diode assemblies use active cooling where water channels in the heat sink improve the cooling of the diode bar.

There are two pump wavelengths that are interesting for ytterbium doped fibre lasers. Figure 38 shows the ytterbium:glass absorption spectrum with the first peak around 910 nm and second higher but narrower peak at around 975 nm. Figure 38 also shows that the emission of a fibre laser is typically in the range of 1020 nm to 1100nm.

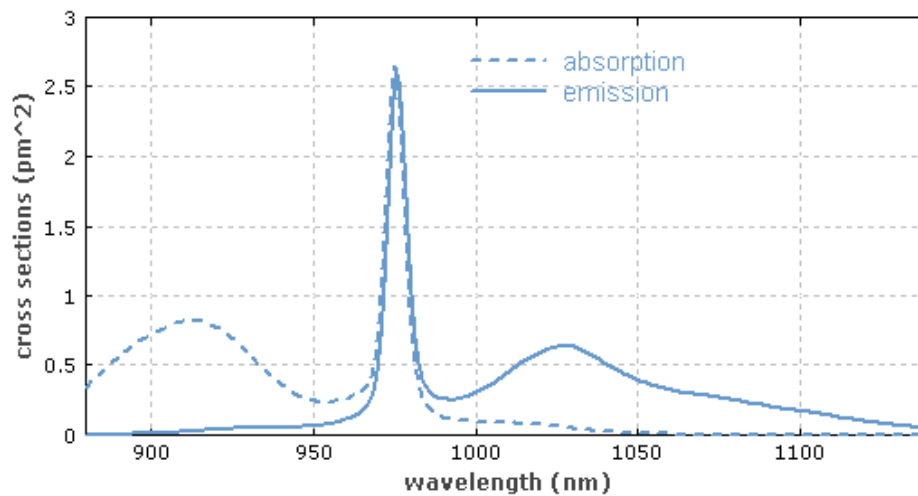


Fig. 38: Pump spectrum of an ytterbium-doped fibre laser⁹².

The slope efficiency is an important factor for the total wall plug efficiency of the laser system. The slope efficiency of pump power to laser power is mostly dependent on the quantum defect between the pump photon energy and the laser photon energy. Having a smaller difference between the pump wavelength and the lasing wavelength reduces the quantum defect⁷⁷. Pumping at 975 nm is preferred and typical for high efficiency operation but requires a good wavelength stabilization of the pump diodes. The larger quantum defect is the reason why a diode pumped Nd:YAG laser pumped at 808 nm and lasing at 1064 nm has a lower efficiency than a typical fibre laser. One other benefit of the laser diode pumping is that the diode wavelength can be tailored to match the absorption spectrum of the active material and therefore will increase efficiency and reduce the thermal load on the active material. Typical reported overall efficiencies for a diode pumped fibre laser is 30-35%. This is a significant improvement compared to the overall efficiency of a lamp pumped Nd:YAG laser of 3-4%.

The lifetime of high power laser diodes used for fibre laser pumping applications is typically between 10,000 and 20,000 hours⁹³. This is significantly longer than lamps that are used in lamp pumped solid state lasers and will reduce the maintenance intervals for a laser production system.

2. Fibre Laser for Microcutting

The flash-lamp pumped Nd:YAG is an established tool for microcutting applications. Certain resonator designs achieve the beam quality and pulse power levels required for microcutting applications. However, as discussed in Chapter 1, conventional flash-lamp pumped solid-state lasers have several disadvantages, such as low wall plug efficiency, high operational costs and poor thermal stability. Great improvements have been made in the thermal stability, but most conventional lamp pumped laser systems on the production floor still require a high level of maintenance. This chapter will compare the beam quality and temporal behaviour of the fibre laser and the lamp pumped Nd:YAG laser, and then compare initial cutting results of the fibre laser and the lamp pumped Nd:YAG laser. An investigation of optimum laser parameters to further improve the cutting results will follow. At the end of the chapter, position synchronized cutting is discussed and the benefits of this technique will be illustrated.

2.1. Experimental Laser Cutting Setup

The cutting systems used for the experiments integrate a CNC motion system, fibre laser, beam collimator and cutting head. For a laser cutting system used in mass production that needs to fulfill market demands and cost targets, the typical throughput has to be 10-20 stents per hour. This requires a reliable and fast motion system with a high degree of precision.

The work described in this thesis uses three different cutting system setups. One system was set up for the stent cutting experiments, one for the flat sheet cutting experiments, while the Nd:YAG laser experiments were performed on the manufacturing line.

Aerotech motion systems (model number A3200) were used in all systems and controlled through a standard personal computer graphical user interface (GUI).

2.1.1. Fibre Laser Stent Cutting System

Figure 39 shows the stent (tubular material) cutting system with one linear stage (Aerotech ATS 1100H) and one rotary stage (Aerotech ADRT-100-85). The stages were mounted on a steel frame. A 50W ytterbium doped single mode fibre laser from IPG (model number PYL 50) was used for the cutting experiments on tubular material. The cutting head was a LaserMech FineKerf™ with 50 mm focusing lens.

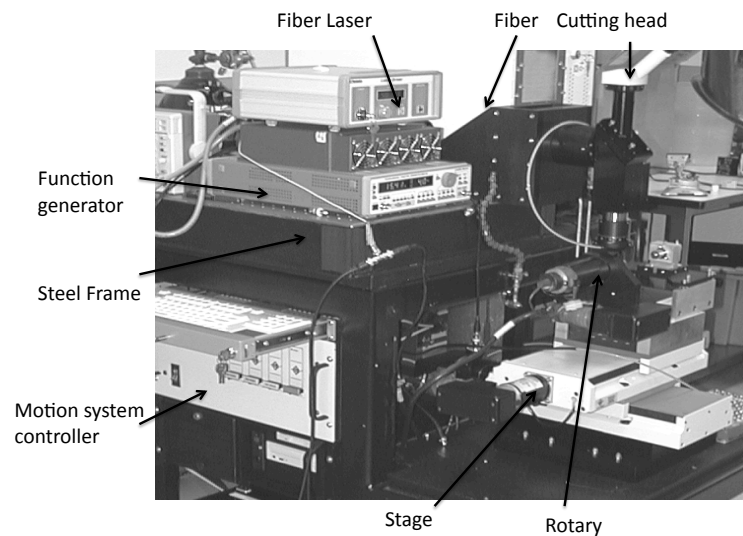


Fig. 39: Experimental fibre laser (IPG PYL 50) cutting system in the laser lab at Guidant for the stent cutting experiment (tubular material).

The IPG PYL 50W fibre laser was forced air-cooled. It was equipped with a 5 m fibre and a collimator at the end of the fibre (see figure 40). The output was collimated by an integrated optic to a 5 mm diameter beam.



Fig. 40: IPG YLM 50W fibre laser with collimator

2.1.2. Fibre Laser Flat Sheet Cutting System

The flat sheet cutting system used a different setup illustrated in figure 41. Originally designed for a high accuracy application, the entire setup is mounted on a granite base with a weight of approximately 300 kg to reduce vibration caused by the rapid movements of the linear stages. The two linear motion stages (ABL 1500 air bearing) were mounted perpendicular to each other. A 100W ytterbium doped single mode fibre laser from SPI (model number SPI 100 C) was used with a LaserMech FineKerf™ cutting head with 50 mm focusing lens.

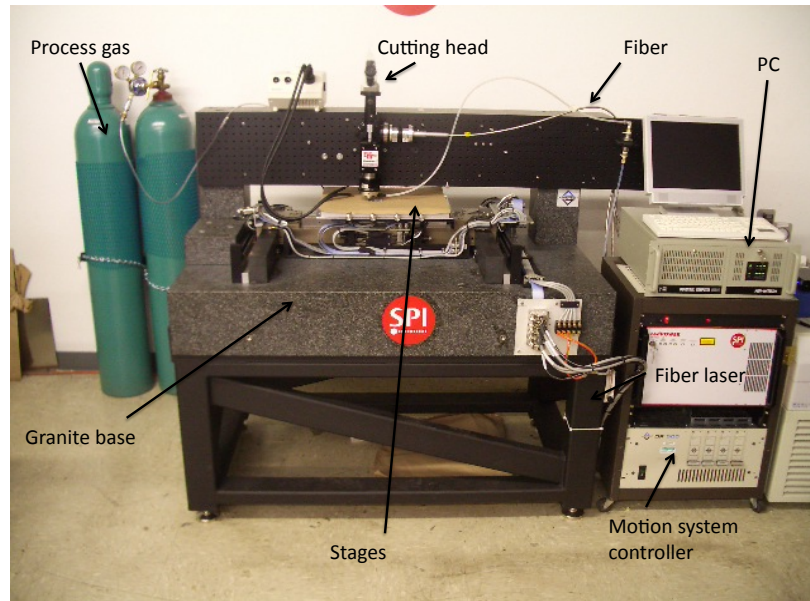


Fig. 41: Experimental fibre laser cutting system with a SPI 100W single mode fibre laser and Aerotech linear stage motion system for the flat sheet cutting experiments.

The SPI fibre laser was water-cooled by a 1 kW water-to-air chiller from Neslab. The SPI fibre laser was operated in a closed loop power control mode. As with the IPG fibre laser used for the stent cutting system, this fibre laser was equipped with a 5 m delivery fibre and a collimator at the end of the fibre (see figure 42). The output beam was collimated to a 5 mm diameter beam.



Fig. 42: SPI 100C fibre laser with delivery fibre and collimator

2.1.3. Nd:YAG Stent Cutting System

The samples for lamp pumped Nd:YAG laser experiments were cut in a regular production environment. The setup was identical to the setup in figure 39 aside from the different laser source (no picture available due to confidentiality agreements).

Figure 43 shows the Nd:YAG laser used for the comparison to the fibre laser process. The Lasag laser (model KLS246FC) was integrated into the stent production systems. This laser used a special resonator setup with two plane mirrors separated by 1.2 m. The output coupler reflected 80% of the signal back into the resonator. The resonator contained a 5 mm Nd:YAG rod and a 1.8 mm mode aperture located 600 mm and 150 mm from the high reflector, respectively. This configuration enables stable TEM₀₀ operation at 4.5 W.



Fig. 43: Lasag KLS 246 FC lamp pumped Nd:YAG laser

The Lasag KLS 246 FC had a resonator housing and a separate power supply. The cutting optic shown in the figure was replaced with the LaserMech cutting optic. Due to low efficiency and resulting high cooling requirements, the Lasag laser used the house water-cooling system.

The Lasag Nd:YAG laser cutting system used an internal pulse generator to set the frequency and pulse length. The laser power was set by the lamp voltage and was calibrated with an external power meter.

2.1.4. Motion System for Laser Cutting

The motion system was programmed using standard G-Codes. The user interface software of the CNC system GUI enabled easy variation of the cutting pattern and cutting speed.

The fibre lasers used an external pulse generator to trigger the laser output pulse. A function generator (HAMEG 8130) was used to set pulse frequency and pulse length.

More complex temporal pulse control, such as a ramp-up or ramp-down pulsing, was realized with an arbitrary function generator from Wavetek (model number 175). This function generator provided a block resolution of 8 bit for the power and time domain, allowing 255 programmable levels in both the power and time domain in each block. Due to the low duty cycle of the laser cutting process only a few steps are available for the laser cycles on-time. The vast majority of the programmed power steps were set to zero. This low resolution for the on-time would result in a step like pulse shape. To use the full resolution (255 steps) of the arbitrary function generator each pulse needs to be triggered by an additional function generator (HAMEG 8130). The second function generator ensures that the arbitrary function generator is only triggered during the on-time of the laser. This technique enables the resolution necessary for a smooth power transition during the laser pulse.

An important feature of the motion system (A3200) is the position synchronized output (PSO). This operation mode generates a frequency modulated output synchronized with the processing speed. This output can be used as a trigger signal for laser pulses for cutting or welding. The PSO logic is illustrated in figure 44. For position synchronized operation the motion systems controller set the laser pulse frequency and pulse length. This feature was only enabled and available for the fibre lasers experiments since the Nd:YAG laser resonator did not have the same stability in the laser parameters (see chapter 1.4.1).

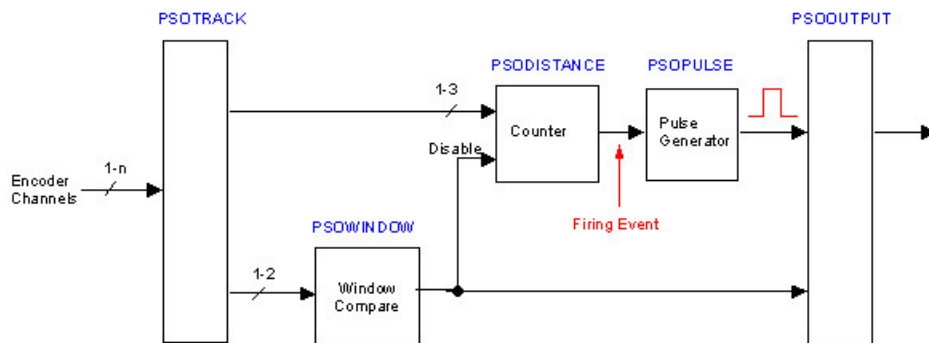


Fig. 44: PSO Control logic⁸²

The “PSO track” defines the encoder input channels. The “PSO distance” defines the distance between each trigger event. In the case of laser machining it is the laser pulse spacing. The “PSO pulse” defines the pulse sequence. The “PSO output” fires the trigger signal for the laser and the “PSO window” defines the area that will be controlled by PSO.

The position error accuracy needs to be maintained during the dynamic motion at a given production speed. Therefore control parameters need to be tuned by the motion systems controller at production speed⁸². The motion system is tuned by monitoring the position error and adjusting the motion system control parameters (K_p , K_i and K_d) appropriately.

2.1.5. Laser Cutting Head

LaserMech manufactured the cutting head for the stent and flat sheet cutting system. Figure 45 shows a drawing of the cutting head. The first cutting head was specially developed for this project. Presently LaserMech offers a standard product based on the design inputs of the project.

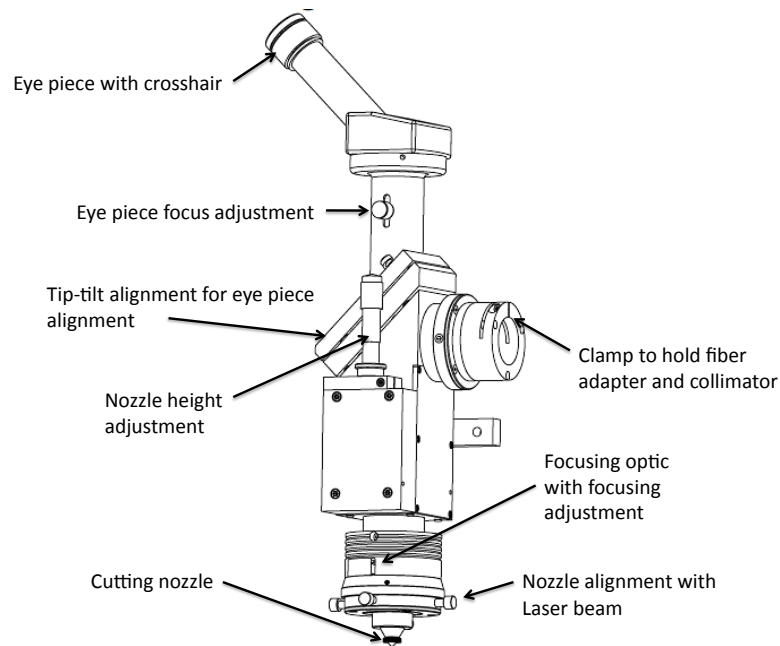


Fig. 45: LaserMech™ Cutting Head

The cutting head includes a focusing optic and an assist gas nozzle. The focusing optic was a 50 mm focus length achromatic doublet from Opto-Sigma serial number 026-0990. The diameter of the cemented achromatic was 50 mm. The optic was coated with an anti-reflection coating in the range of 1000-1200 nm. The nozzle exit hole diameter was 0.5 mm. Nozzle standoff and diameter was kept constant for all cutting experiments. The current nozzle configuration provided the best results if the standoff between the work piece and the nozzle orifice was kept as small as possible, minimizing possible contamination from the cutting process. The practical optimum standoff for this experimental setup was 0.4 mm. This distance is less than the distance to the first Mach disk and gas pressure fluctuation of the ultrasonic gas flow should not influence flow in the kerf. A standoff distance less than 0.4 mm could create the risk of nozzle orifice contamination with splatter from molten or vaporized metal at the process

area. Those contaminations will build up and restrict the assist gas flow. Even at this standoff, a periodic cleaning of the nozzle (every 2-3 days during production) is necessary.

The alignment of the collimated beam to the focusing optic is very important. The collimated beam needs to be in the centre and normal to the focusing optic otherwise a coma effect will move the focus spot, increase the focus diameter and distort the beam profile. The following figure 46 shows the effect of an angular misalignment of the collimated beam to the focusing optic.

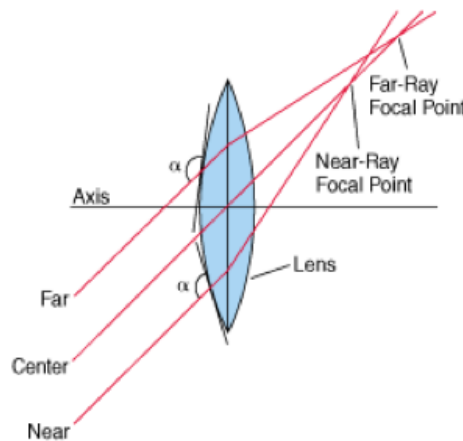


Fig. 46: Coma appears in the focus because of off-axis rays focus at different points⁹⁴

The beam was aligned by first replacing the focusing optic with a cross hair and imaging the beam on a detector plate. The shadow of the cross hair on the detector plate shows if the beam is in the centre of the optic holder (see figure 47). The beam was centered by the tip-tilt alignment (see figure 45). To check the angular alignment, the focusing optic was placed back into the optic head and the position of the focus and the collimated beam on the detector plate was compared. If the focused spot was in the centre of the collimated spot (recorded without the focusing optic) the

angular alignment was considered as acceptable. The detector plate was from Kentek (View-it ®). The stimulated range was 800-1700 nm with an emission colour of 530 nm (visible green).



Fig. 47: Laser beam on View-it ® from Kentek Inc.

The next step in the alignment procedure was the nozzle centering with the nozzle adjustment screws. For this alignment, the laser was fired for one pulse and the nozzle orifice was visually centered to the burn mark on the work piece using the eye-piece.

The primary benefit of the focusing head design was that the nozzle standoff could be adjusted separately from the focus lens alignment (see figure 45). The nozzle standoff was adjusted with the help of a feeler gauge and locked for that experiment at 0.4 mm. The focus was adjusted by cutting a few lines into a specimen and recording the focus spot position for each line. Later the optimum focus position was selected by visually inspecting the kerf width over the range of focusing optic settings.

Due to the low average power for micromachining, the laser cutting head had no active cooling. Thermal lensing in the cutting head at less than 100 W laser power levels was not a concern.

2.1.6. Material and Assist Gas for the Cutting Experiments

The cut samples were 316 series stainless steel. Grade 316 is standard molybdenum grade austenitic stainless steel. The chemical composition is:

Fe, < 0.03% C, 16-18.5% Cr, 10-14% Ni, 2-3% Mo, < 2% Mn, < 1% Si, < 0.045% P, < 0.03% S

Due to the excellent biocompatibility this material is the standard material used for medical devices such as the stent.

The process gas for all the cutting experiments was cylinder supplied 99.99% pure oxygen. The two-stage gas regulator allowed a gas pressure range of 1 to 10 bar with 0.1 bar resolution.

2.1.7. Beam Diagnostic Setup of YAG Laser and Fibre Lasers

The beam quality is an important factor for lasers used for micromachining applications. The most commonly used approach to characterize beam quality is the M^2 concept. M^2 is the ratio between the divergence of a Gaussian beam and the divergence of the actual laser beam. M^2 is also described in the literature as $1/K$ and is by definition always greater than 1.

According to Steen⁶⁷ M^2 is:

$$M^2 = \frac{D_0 \theta_\infty \pi}{4\lambda} \quad (2.1)$$

where D_0 is the beam minimum waist diameter and θ_∞ is the far field divergence. According to ISO/DIN 11146⁹⁶ it is not possible to calculate the beam quality from a single beam profile measurement. It is essential to

make several beam width measurements in the beam waist and several in the far field. The measurements in the focused beam will determine the minimum beam waist D_0 and the measurements in the far field will calculate the far field divergence θ_∞ . According to the ISO/DIN 11146 at least 5 measurements are required in the beam waist and in the far field regions.

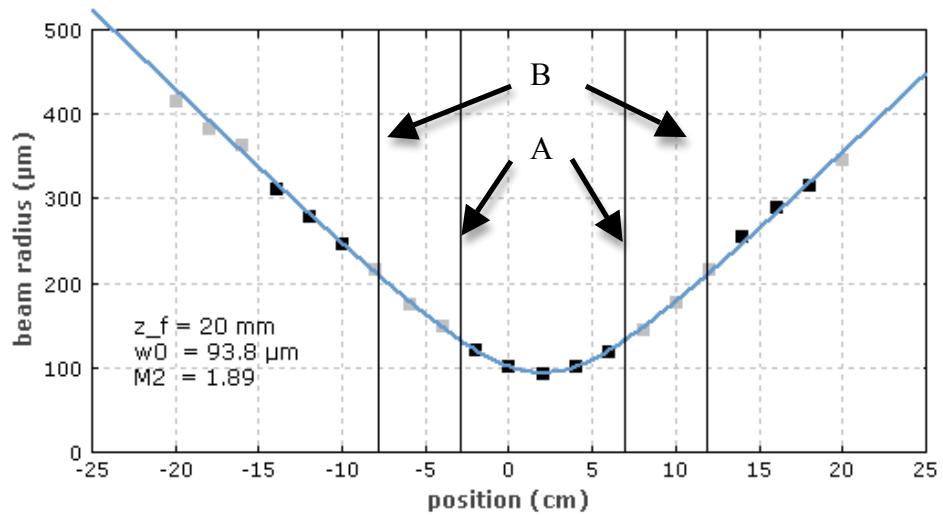


Fig. 48: Calculation of beam quality from measured caustic.

Figure 48 shows a beam propagation profile, also called a caustic, according to ISO/DIN standards. The black points are those used for the fitting procedure to calculate the beam waist and the far field divergence. In this example the beam quality is $M^2 = 1.89$.

The inner two vertical lines (A) in figure 48 indicate the Rayleigh length. Those data points are used to calculate the minimum beam waist. The far field starts after the Rayleigh length. The next set of vertical lines (B) defines the beginning of the area used to collect data points for the far field divergence calculations.

The Rayleigh length can be calculated with:

$$R = \frac{D_0^2 \pi}{4M^2\lambda} \quad (2.2)$$

R is the distance at which the beam diameter increases to $\sqrt{2}$ times the beam diameter in the focus (minimum beam waist).

ISO/DIN 11146 requires that the beam width is based on the second moment or $D4\sigma$ method. $D4\sigma$ stands for 4 times σ , where σ is the standard deviation of the horizontal or vertical marginal distribution. This method is very sensitive to noise in the base line. The imaging system employed a special algorithm to limit the effect of the noise on the measurement.

The beam width can be measured in many different ways. The four main types of beam profiling are camera-based systems, knife-edge scanners, slit scanners and pinhole scanners. The camera-based system was used for the work described in this thesis. The benefit of the camera-based system was that it detects and displays any structure that exists on the profile. The primary disadvantage was that the pixel size (0.005 to 0.01 mm) limits the minimum beam diameter to 0.06 mm to have enough pixels to measure the beam width⁹⁷. Another disadvantage was that the laser power needed to be carefully attenuated to avoid any damage to the CCD camera.

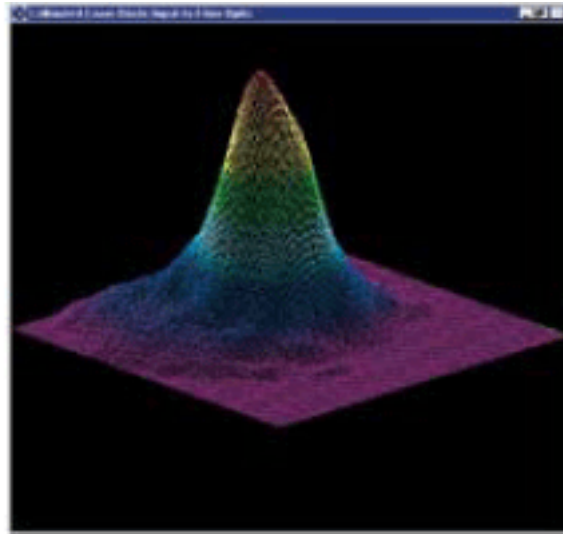


Fig. 49: Typical Beam Profile of a single mode Nd:YAG laser measured with the M200 from Spiricon™.

Figure 49 shows a typical beam profile with a CCD camera based system. The ISO standard requires that a beam profile needs to be acquired for each data point on the caustic to calculate the beam quality. The next figure (figure 50) shows the layout of the M200 beam quality measurement system from Spiricon.

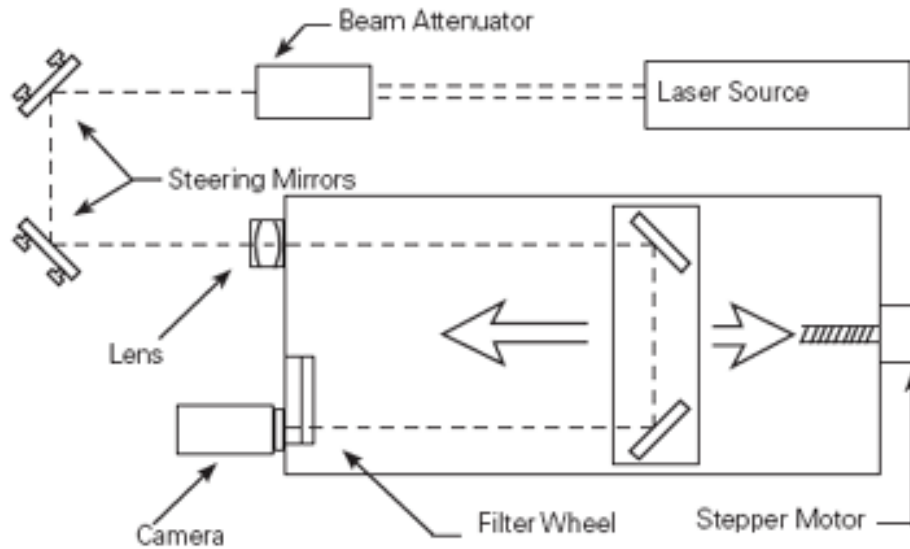


Fig. 50: Beam quality measurement setup M200 from Spiricon™.

To avoid damage to the CCD chip in the camera, the beam attenuator lowers the incident power. The two steering mirrors align the beam into the device. A 500 mm long focus length lens focuses the beam on the camera. The stepper motor moves the two mirrors on the stage thereby changing the beam path length to the predefined position shown for the example plot in figure 48.

2.1.8. Laser Pulse Measurement

The temporal behavior of the fibre laser pulse and the output signal of the function generator were monitored and measured with a Tektronix TDS 3012 100 MHz digital oscilloscope and a Thorlabs (DET410/M) InGaAs photo diode. The 100 mega sample oscilloscope, in combination with the 5 ns minimum rise and fall time of the biased photo diode signal, provided sufficient resolution for the measurement of the temporal behavior. The spectral response of this InGaAs diode seen in figure 51 was 700-1800 nm and covered the wavelength of the lasers used for this thesis.

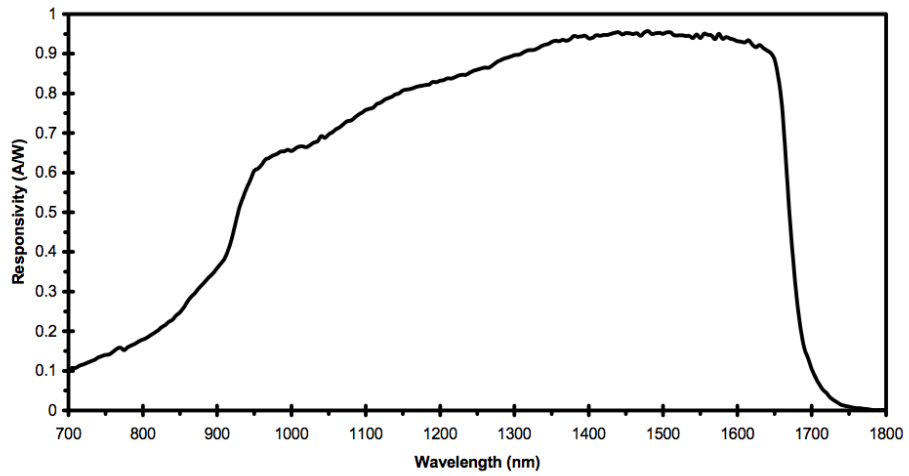


Fig. 51: DET410 Spectral responsivity curve⁹⁴

The photo diode cannot be placed directly into the laser beam because the damage threshold is only 100mW. Figure 52 shows a sketch of the setup for the measurement of the temporal behavior of the laser pulse. The diode detects the light from the diffuse reflection from a piece of white ceramic. The laser power level of diffuse reflection is below the damage threshold of the diode.

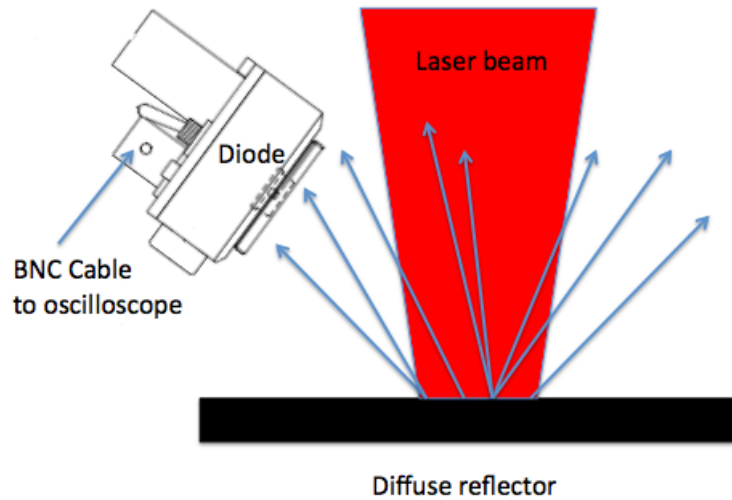


Fig. 52: Photo diode measurement setup.

2.1.9. Surface Roughness Measurement

The surface roughness was measured with an optical interferometric profiler from VEECO (model number 3300 N, see figure 53) with a measurement field of view of 0.2 by 0.25 mm. This system offers a sub-nanometer resolution and a measurement range from 1 nm to 10 mm. The measurement records the average surface roughness Ra . This profiler detects interference fringes that are formed by light waves interfering with each other. The profiler counts the interference fringes generated between a plane wave and a beam reflected from the surface of the specimen. The amount of light reflected from the surface limits the use of this technique and prevents the use with samples that have a high depth-to-width ratio. For the experiment evaluation the sidewall was divided into three sections and the measurements were taken in the centre of each section.



Fig. 53: Veeco™ Optical Profiler 3300N at Guidant.

Figure 54 shows screen-shot for one of the surface roughness measurements for this work.

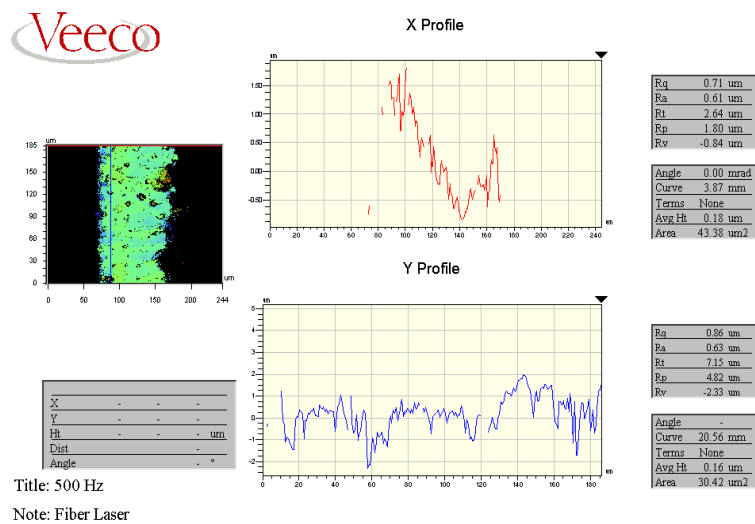


Fig. 54: Veeco™ Optical Profiler 3300N screen-shoot.

2.2. Comparing Pulsed Fibre Lasers with Traditional Flash Lamp Pumped Nd:YAG Solid State Lasers

The fibre laser and Nd:YAG laser systems were set up with special care to accomplish a valid comparison independent from all cutting parameters beside the two different laser sources. In the following investigation, the beam quality and the temporal behavior of the laser were of special interest. The comparison concludes with presenting initial cutting results for the fibre and pulse Nd:YAG laser.

2.2.1. Beam Quality Measurement

The beam quality of the fibre laser and Nd:YAG laser was measured with a SPIRICON M200 beam quality measurement system. Section 2.1.7 outlines the concept of this device. For the beam quality measurements, the output of the fibre laser was collimated to a beam diameter of 5 mm and aligned into the beam quality measurement device.

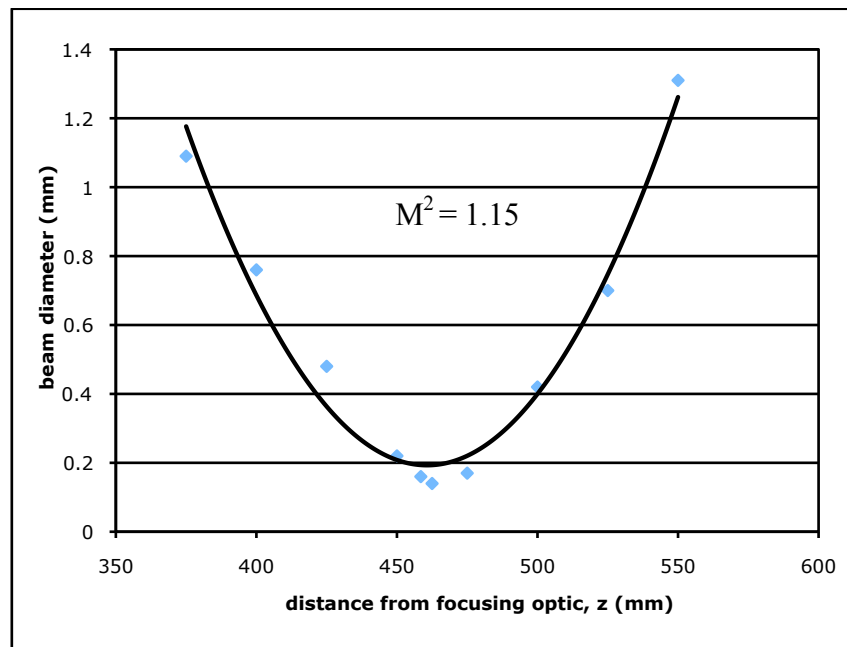


Fig. 55: Beam propagation for fibre laser after collimator, at 4.5 W with 0.1 ms pulse length and 1500 Hz pulse frequency. $M^2 = 1.15$ for a 500 mm focusing optic.

As expected the single mode fibre laser beam had a beam quality close to the diffraction limit. Based on the beam propagation shown in figure 55 the beam quality M^2 of the fibre laser was 1.15 at 4.5 W average laser power setting.

The variable beam expander of the lamp pumped pulsed Nd:YAG lasers was set to a 5 mm collimated beam diameter. Resonator length and mode aperture in the resonator were adjusted to get close to diffraction limited beam quality output for the 4.5W average laser power level. Based on beam propagation measurements shown in figure 56 the measured beam quality of the lamp pumped pulsed Nd:YAG laser M^2 was 1.14.

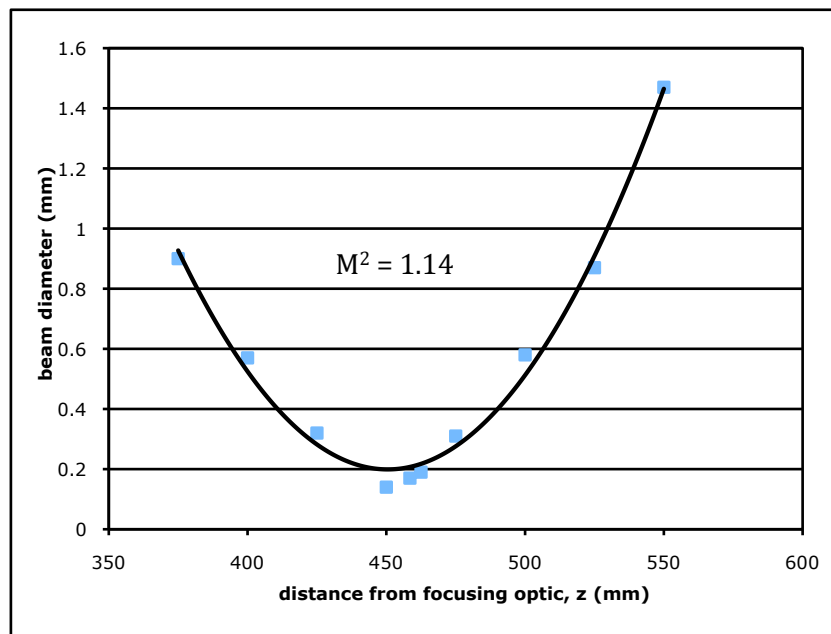


Fig. 56: Beam propagation of lamp pumped pulsed Nd:YAG laser after collimator, at 4.5W with 0.1 ms pulse length and 1500Hz pulse frequency, $M^2 = 1.14$ with a 500 mm focusing optic.

Due to the fact that the beam quality of the Nd:YAG laser and the fibre laser at 4.5 W average laser power was similar, the actual kerf width for both lasers should be the same if the same cutting head and power settings were used.

The measurement of the beam quality was repeated at several power levels for the fibre laser and the Nd:YAG laser and was recorded in the table below.

Average Laser Power	Beam Quality M^2	Beam Quality M^2
	Fibre Laser	Nd:YAG Laser
2.0 W	1.13	1.72
2.5 W	1.14	1.53
3.0 W	1.16	1.41
3.5 W	1.13	1.17
4.0 W	1.15	1.13
4.5 W	1.15	1.14
5.0 W	1.14	2.31
6.0 W	1.13	no laser output

Table 2.1: Variation of beam quality with laser power for fibre laser and lamp pumped Nd:YAG laser

The above table shows that the fibre laser beam quality was constant for different laser output powers. The lamp pumped Nd:YAG laser on the other hand showed a significant variation in beam quality for different laser output powers. The reason for this was that the Nd:YAG laser has thermal lensing effects in the active media that changes the resonator and results in a variation of beam quality with output power. At elevated pump power the Nd:YAG laser became unstable and was not able to reach the 6 W average laser power level. To match the beam quality and spot size of the fibre laser the Nd:YAG laser can only operate between 3.5 and 4.5 W average output power.

2.2.2. Temporal Behavior

The temporal behaviour of the fibre laser and the lamp pumped Nd:YAG laser was different. Pumping scheme and resonator layout are the reason for this. The following paragraphs will show and describe those different temporal behaviours of fibre laser pulses and lamp pumped Nd:YAG laser pulses.

2.2.2.1. Temporal Behavior of Fibre Lasers

An external pulse generator was used to set the pulse frequency and the pulse length of the fibre laser. The pulse frequency was 1500 Hz and the pulse length was set to 0.1 ms. The 30 W pulse power was preset by the power supply of the fibre laser.

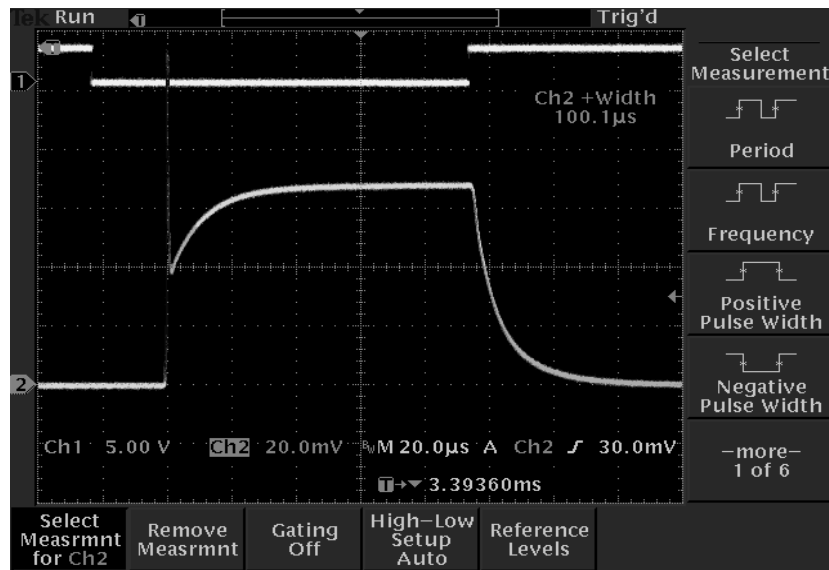


Fig. 57: Screen shot of typical Fibre Laser Pulse Shape measured with a Tektronix 100 MHz digital oscilloscope and a Thorlabs (DET410/M) InGaAs photo diode with a 0.5 ns response time.

The top trace in figure 57 shows the gating signal from the pulse generator and the bottom trace shows the temporal development of a typical laser pulse used in this work measured with a photo diode. The ytterbium-doped

fibre laser started to generate output power 0.025 ms after the trigger signal. This delay needs to be factored in when setting the pulse length of the fibre laser output. This delay could be explained by the response time of the laser power supply to provide the necessary pump diode current and the time constant to provide sufficient inversion population in the gain media of the fibre laser. This delay is dependent on the pulse power level and is shorter for higher power levels than for lower power levels. This behaviour supports the hypothesis that some of the delay results from inversion effects. These relatively long delays are possible because the 1/e fluorescence decay time in an ytterbium (Yb) double-clad fibre laser could be as long as 0.8 ms⁹⁸. The laser output power then stabilizes at a stationary value after an initial spike caused by relaxation oscillation⁷³. The initial spike of the relaxation oscillation was < 0.001 ms. The energy in this spike appears to be insignificant compared with the total energy in the pulse. Therefore in this work the pulse power was defined as the stabilized power during the pulse (figure 57). Different pulse frequencies and pulse durations result in a different relaxation oscillation behaviour. Lower duty cycles typically result in a high peak at the start of the pulse. Higher duty cycles result in a lower peak. The magnitude of the peak at the beginning of the pulse is caused by the amount of stored energy in the active material, in this case the Yb-doped fibre of the fibre laser.

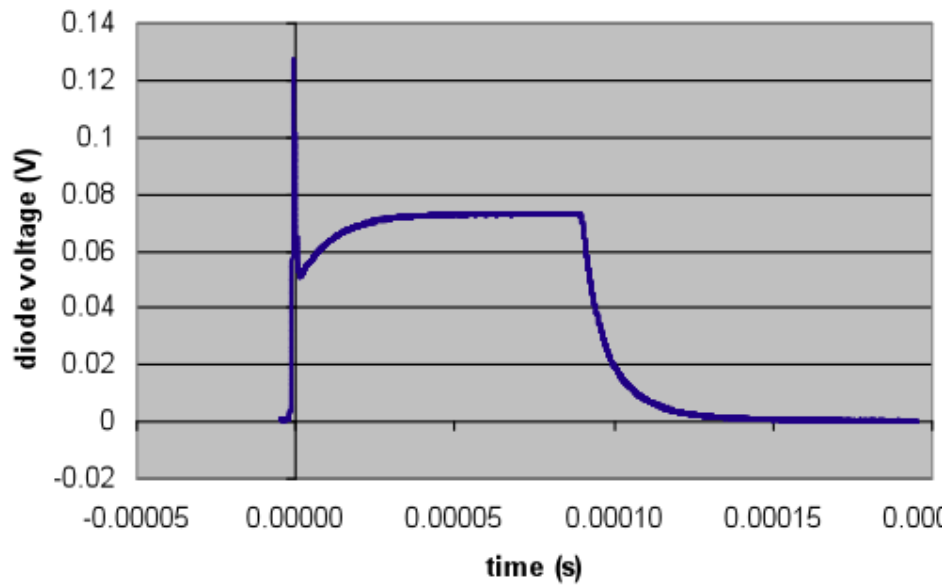


Fig. 58: Temporal behaviour of a typical fibre laser pulse exported of a Tektronix 100 MHz digital oscilloscope measured with a Thorlabs (DET410/M) InGaAs photo diode with 0.5 ns response time.

Figure 58 shows the data after it was exported into an Excel spreadsheet. Unlike the lamp pumped solid-state laser pulse (figure 59) there are no addition spikes or oscillations observable. The fibre laser pulse showed a rise time of less than 500 ns and a fast decay of 0.02 ms at the end of the gate signal.

2.2.2.2. Temporal Behavior of Flash Lamp Pumped Nd:YAG

Lasers

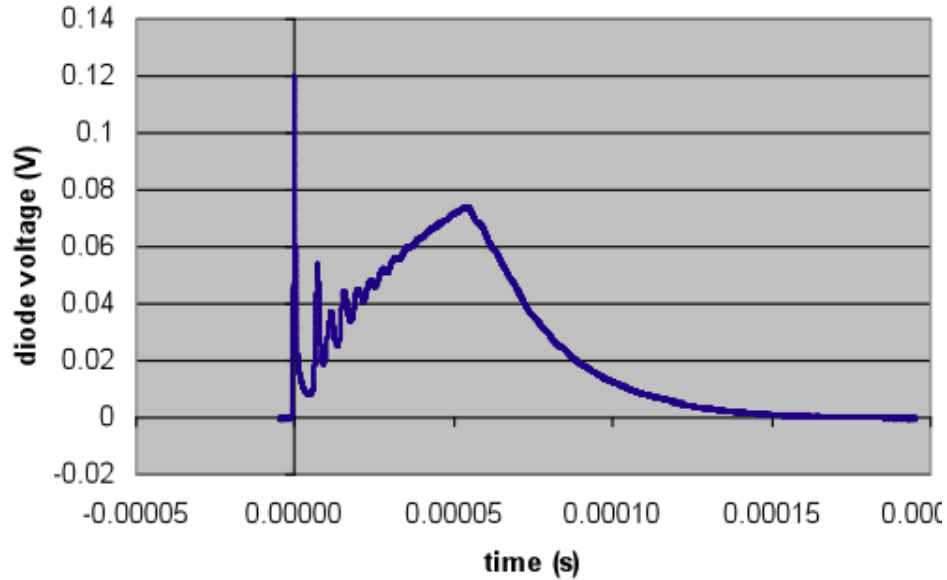


Fig. 59: Temporal behaviour of a lamp pumped Nd:YAG laser exported of a Tektronix 100 MHz digital oscilloscope measured with a Thorlabs (DET410/M) InGaAs photo diode with 0.5 ns response time.

Figure 59 shows the temporal behaviour of the pulse of a lamp pumped Nd:YAG laser. The laser power supply sets the pulse length for the Nd:YAG laser output. The Nd:YAG laser was set to 0.05 ms and 1500 Hz pulse frequency for this measurement. This pulse in the lamp pumped solid-state laser case was dominated by several spikes caused by temporal modes and relaxation oscillations⁷³. The rise time was in the 500 ns range like the fibre laser but the decay time of 0.1 ms was significantly longer.

2.2.3. Comparing the cutting results of the Fibre Laser Cutting Process with the Flash Lamp Pumped Nd:YAG Laser

Cutting results with a 50 W ytterbium doped fibre laser (IPG, model number PYL 50 Series). In the cutting experiments presented here the laser was collimated to a 5 mm diameter, and then focused with a 50 mm focusing optic. The oxygen assist gas pressure for the fibre laser cutting was set at 6 bar.

The user interface of the Lasag lamp pumped Nd:YAG laser was used to set frequency, pulse length and lamp current. Typical cutting parameters for the Nd:YAG laser for micromachining are 1500 Hz pulse-to-pulse frequency, 0.1 ms pulse length. The power meter reading for the initial cutting experiments read 4.5 W. After considering the duty cycle of 6.6 % the pulse power was 30W. The fibre laser was set up with the same laser parameters as the Nd:YAG laser. Both lasers employed a 5 mm collimated beam and a 50 mm focusing optic. The oxygen assist gas pressure was set at 6 bar. The cutting speed was set at 4 mm/s.

The beam quality formula is ⁶⁷:

$$M^2 = \frac{D_0 \theta_\infty \pi}{4 \lambda} \quad (2.3)$$

where,

d_0 is the focus diameter

θ_∞ is the far field beam divergence

λ is the wavelength

Based on the beam quality formula the spot diameter should be:

$$D_0 = \frac{M^2 4 \lambda}{\theta_\infty \pi} \quad (2.4)$$

The 50 mm focal length optic (f) in the cutting head in combination with a 5 mm collimated beam (D_C) creates a far field divergence of:

$$\theta_{\infty} = \frac{D_C}{f} \quad (2.5)$$

where D_C is the collimated beam size.

With the given values and due to the fact that the beam quality and the wavelength are very close to each other the theoretical spot size D_0 should be in the range of 0.015 mm for both lasers.

The Rayleigh range can be calculated with the following formula:

$$R = \frac{D_0^2 \pi}{4M^2\lambda} \quad (2.6)$$

Based on this formula the Rayleigh range R is 0.15 mm.

The actual kerf width in the 0.100 mm steel samples was measured and was in the range of 0.018 to 0.020 mm for fibre laser. The side-wall showed only limited taper. This suggests that a material thickness well inside the Rayleigh range limits the influence of the beam caustic on the laser cut kerf width.

The following two figures 60 and 61 are SEM images of sidewalls with the fibre laser cutting system and the pulsed lamp pumped Nd:YAG laser at those laser settings.

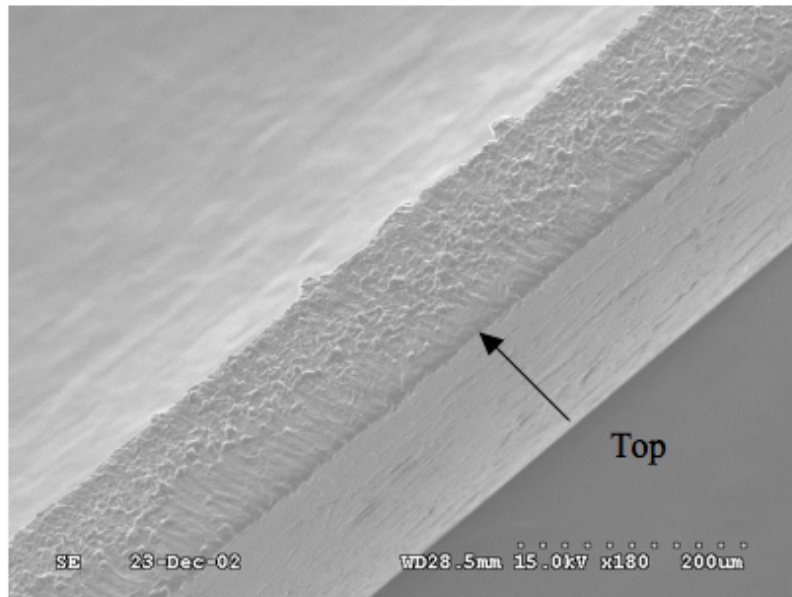


Fig. 60: SEM picture of a laser cut sidewall with a pulsed fibre laser.

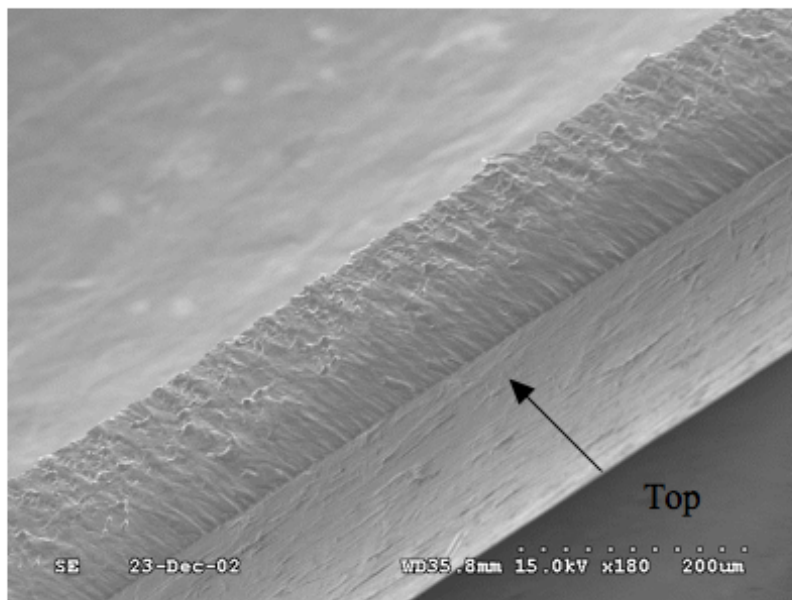


Fig. 61: SEM picture of a laser cut side-wall with a pulsed lamp pumped Nd:YAG laser.

The SEM pictures showed a sufficiently good cutting quality for both laser systems. The striations were similar with a minimum burr at the bottom of the sidewall. To make a quantitative statement on the surface roughness of the sidewall an investigation with an optical profiler was necessary. For the following measurement the optical beam profiler was averaging the surface roughness over the entire sidewall of the cut surface. For this surface roughness measurement a VEECO 3300 N optical profiler with a measurement field size of 0.2 by 0.25 mm was used.

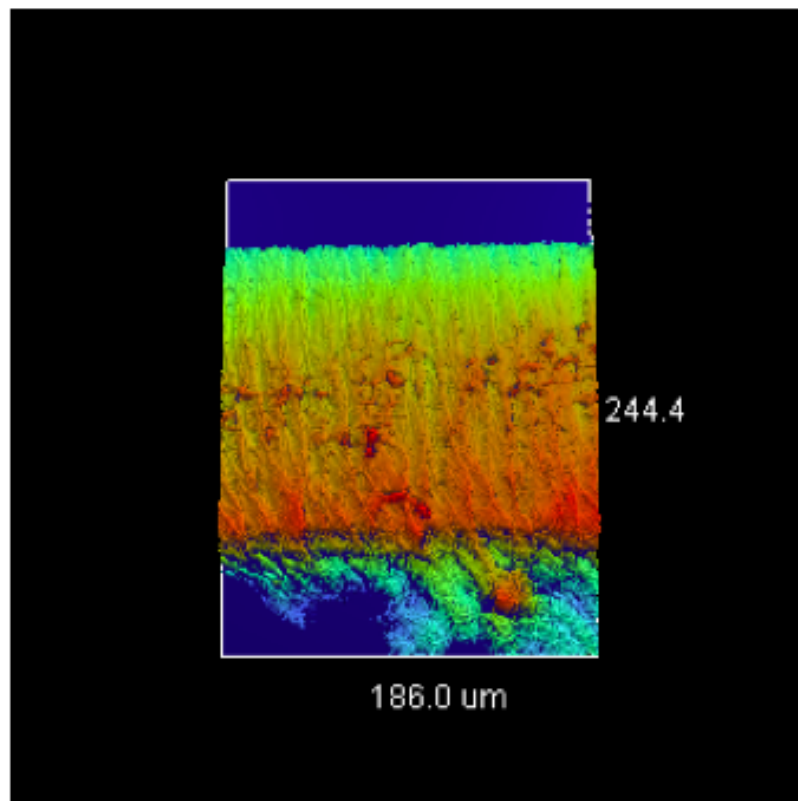


Fig. 62 Optical profiler picture of a laser cut side-wall for a pulsed fibre laser.

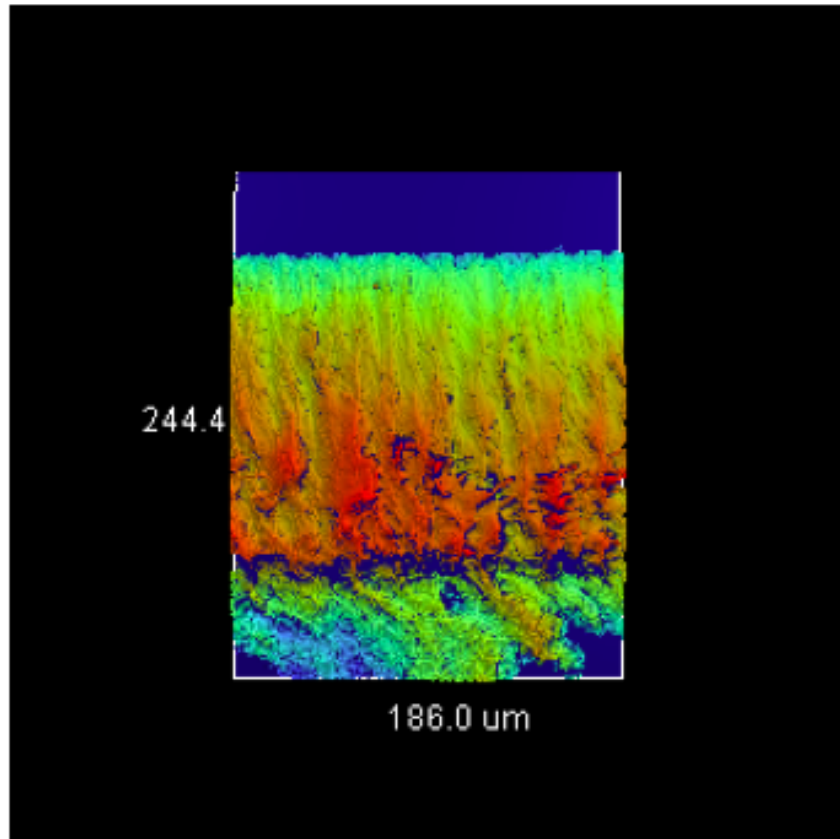


Fig. 63: Optical profiler picture of a laser cut side-wall for a pulsed lamp pumped Nd:YAG laser.

The different heights on the surface are colour coded for a better visualization of the surface profile. The optical profiler measured a surface roughness of Ra of $0.48 \mu\text{m}$ for the pulsed Nd:YAG laser (figure 63) compared to $0.44 \mu\text{m}$ with the fibre laser (figure 62).

The following table shows a series of experiments were performed to compare the surface quality of the fibre laser with the Nd:YAG Laser. The laser settings are identical for all measurements.

Experiment	Surface Roughness Ra μm	Surface Roughness Ra μm
	Fibre Laser	Nd:YAG Laser
1	0.48	0.44
2	0.49	0.45
3	0.56	0.42
4	0.45	0.55
5	0.54	0.55
StaDev	0.0451	0.063
average	0.504	0.482

Table 2.2: Surface roughness for fibre laser and lamp pumped Nd:YAG laser

The difference in the average surface roughness between the fibre laser and the Nd:YAG laser was significantly smaller than the standard deviation of the measurements. Therefore, the average surface roughness measurement data showed no significantly statistical variance between the fibre and the Nd:YAG laser cutting process.

2.2.4. Conclusion on initial experiments to compare Nd:YAG Laser and Fibre Laser cutting

1. After carefully tuning the lamp pumped Nd:YAG laser system the beam quality matched the beam quality of the fibre laser system at the 4.5 W output power level.
2. The fibre laser did not change beam quality with output power (in the 2-6W range). The Nd:YAG laser did change the beam quality with output power due to thermal lensing effect in the resonator. This limits the use of the Nd:YAG laser to a narrow laser output power range and therefore, limits the selection of laser cutting parameters for microcutting.
3. The cutting quality and performance based on surface roughness measurements of the pulsed fibre laser was similar to the cutting

quality of the Nd:YAG Laser. The surface roughness measurements did not show a statistical significantly difference.

4. The temporal laser pulse behavior of the fibre laser and the lamp pumped Nd:YAG laser was similar but not identical. The differences in temporal behavior did not influence the cutting quality; specifically the surface roughness was identical.

2.3. Pulsed Fibre Laser Cutting Process Optimizations

After establishing that the fibre laser provides similar cutting results to that of the Nd:YAG laser, further investigations of the laser parameters were of interest to improve and optimize the cutting results with the fibre laser. A closer look at the laser pulse parameters such as pulse length, pulse frequency and pulse power was necessary. The specific application that the system was optimized for was the cutting of medical stainless steel (316 grade) stents.

The key requirement was a narrow consistent kerf that demands constant beam quality with excellent laser power stability. To reduce post-processing of the stent the kerf sidewalls need to have a good surface quality with a minimum amount of slag and burr. Similarly, the heat affected zone (HAZ), which consists mostly of molten material recast, needs to be minimized. Figure 64 shows an SEM picture of a typical stent after cutting and cleaning in an ultrasonic bath.

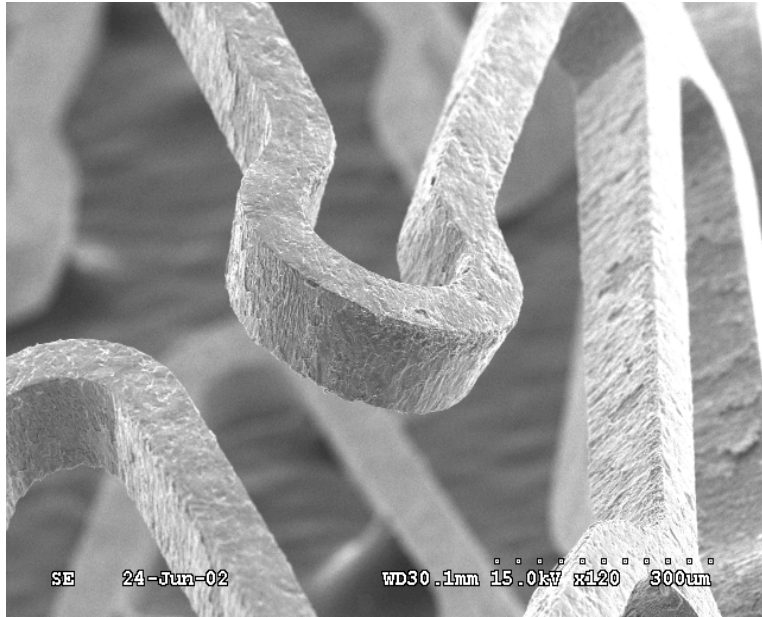


Fig. 64: SEM picture of a stainless steel stent delivery system after ultra sonic cleaning.

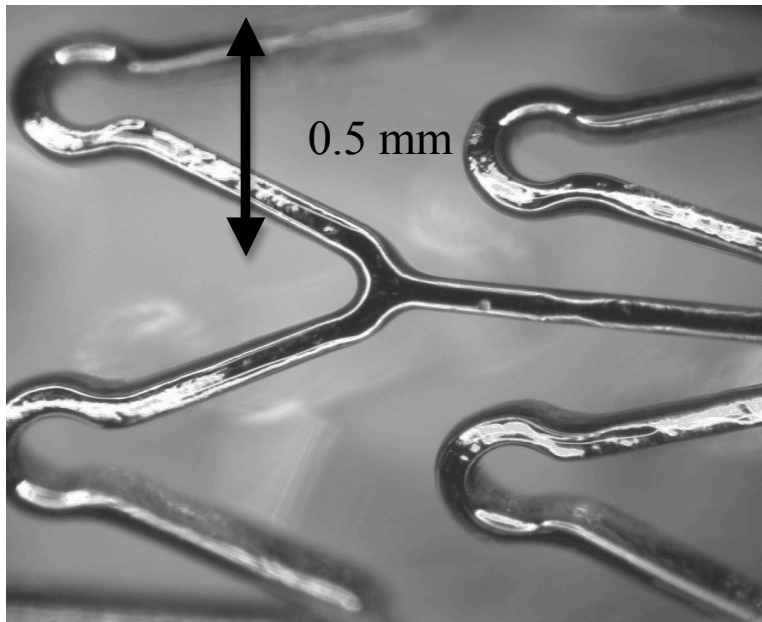


Fig. 65: SEM picture of a stainless steel stent after electro polishing.

After removing the slag and most of the burr, the stents are electro-polished to achieve a smooth surface finish and to remove the recast layer. It is important to remove the stainless steel slag completely from the material surface since it is not conductive and would not be affected by the electro polishing process. Besides smoothing the surface, the electro-polishing process also removes the recast layer to ensure the mechanical properties of the implant. Figure 65 shows a picture of a typical stent after electro-polishing. Additionally, laser settings that enable cutting at the lowest possible average laser power were investigated. This was necessary in order to reduce the possibility of laser introduced damage to the opposite tube wall during the stent cutting process out of a 2-3 mm diameter stainless steel tube.

2.3.1. Fibre Laser Cutting Experiment Scope

This investigation shows cutting results with a pulsed fibre laser for different laser pulse parameters. The goal was to find operating conditions that minimize the heat affected zone and surface roughness.

As in the previous experiments the focus position and assist gas nozzle standoff were kept constant during the experiment. The standoff was 0.4 mm with a focus position optimized to achieve a minimum kerf width. Due to the fact that the fibre laser has no thermal lensing effect, the beam distribution did not change with the variation of the pulse length, pulse power and frequency of the laser pulses. 99.99% pure oxygen was used as the assist gas for the experiments.

2.3.2. Effect of Laser Peak Pulse Power on Surface Roughness

In order to investigate the effect of peak pulse power on the surface quality several cuts were made at constant frequency, pulse width, cutting speed and oxygen pressure. The material was 0.1 mm thick series 316 stainless steel.

Figure 66 shows the relationship between the average surface roughness and the peak pulse power. The cutting parameters for this experiment were 1500 Hz pulse frequency, 0.1 ms pulse length, 6 bar assist gas pressure (O₂) and 4 mm/s cutting speed. The surface roughness measurements were from the top, mid and bottom section of the specimen. Each data point was the average of three to four measurements on each sample.

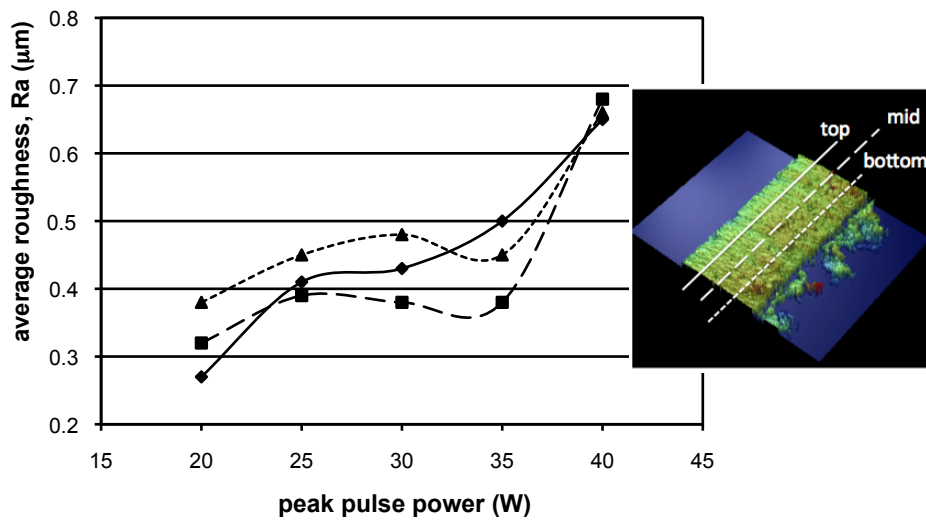


Fig. 66: Average surface roughness as a function of laser peak power with indication of measurement location.

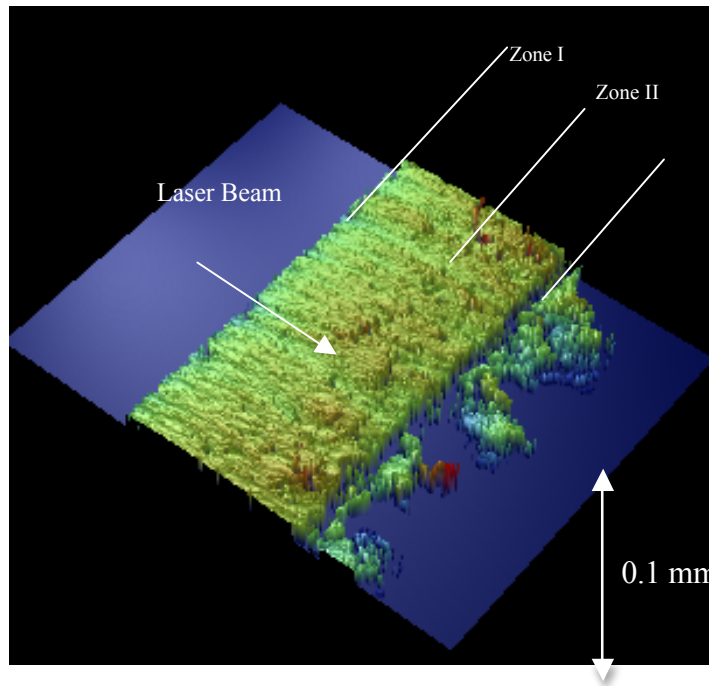


Fig. 67: Optical Profiler Image for Laser Cut Sidewall at 20W Laser Peak Power. At 1500 Hz pulse frequency

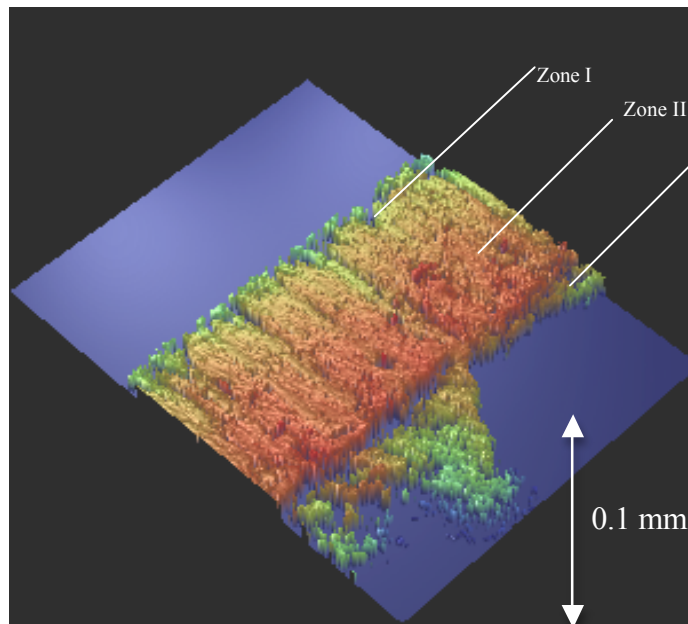


Fig. 68: Optical Profiler Image for Laser Cut Sidewall at 40W Laser Peak Power. At 1500 Hz pulse frequency.

The peak pulse power applied to create the cut shown in figure 67 was 20 W. It had a typical cutting edge that appears to have two distinct zones. Zone I shows regular striations starting from the top edge of the laser cut. In zone II no or indistinct striations can be observed⁹⁹. Figure 68 shows the edge of a cut that was made with a pulse power of 40 W. The higher peak pulse power increased the striations in zone I, only at the very bottom did the cut edge have no striations. At lower peak pulse power the surface quality degraded from the bottom to the top edge of the cut edge. In Zone II (also called the melt shear zone) the cut was dominated by the dynamics of the molten metal flow. At lower peak pulse power the surface roughness of the striations in zone I was lower than the surface roughness in zone II. Figure 68 shows that the surface roughness was increasing with higher peak pulse power due to deeper natural striations along a wider area on the cut edge. The laser pulse frequency was significantly higher than the striation frequency observed in zone I. This effect could be explained by the fact that the individual laser pulses at this frequency did not have sufficient energy to affect the striations and that the natural striation frequency was overriding the pulsing effect of the laser¹⁰⁰.

2.3.3. Effects of Laser Pulse Frequency on Surface Roughness

Figure 69 shows the relationship between the average surface roughness and the laser pulse frequency. Each data point was an average of three to four measurements. The measurements were taken at the top, mid and bottom sections of the specimen.

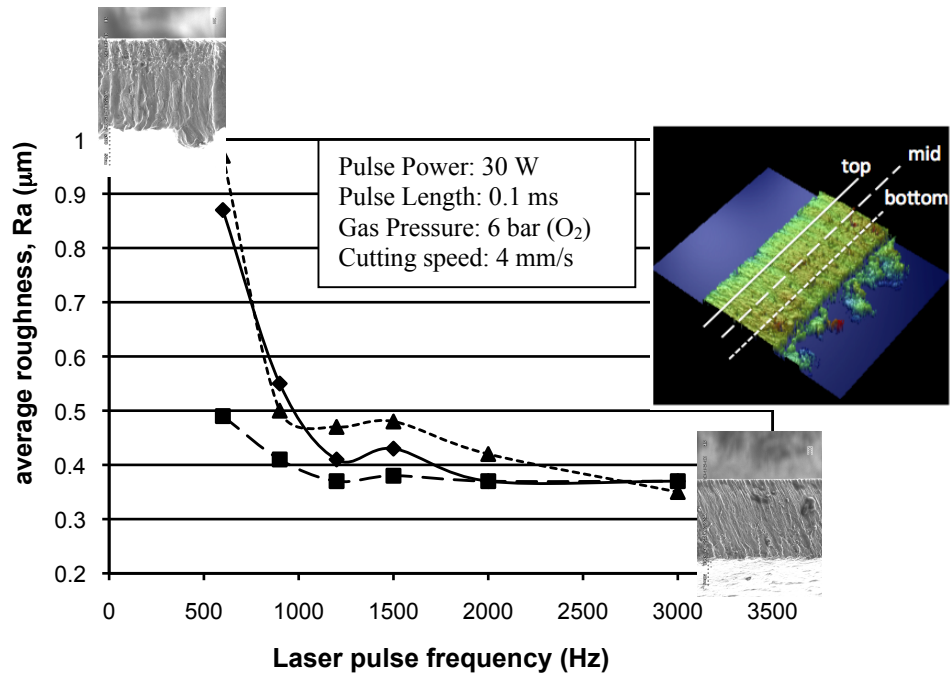


Fig. 69: Average Surface Roughness as a Function of Laser Pulse Frequency. SEM Pictures for 600Hz and 3000Hz.

The surface roughness varied from top to bottom of the kerf due to different material removal mechanisms¹⁰¹. At low pulse frequencies with lower pulse-to-pulse overlap, individual laser pulses affected the surface roughness.

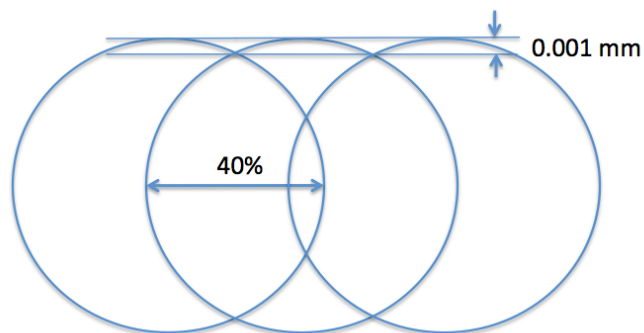


Fig. 70: Theoretical surface roughness caused by overlapping laser pulses at 600Hz.

Figure 70 shows the geometrical pulse-to-pulse overlap at 600 Hz. At this frequency the pulse-to-pulse overlap is 40%. The calculated surface roughness by the overlapping pulses is 0.001 mm. This value is actually matching the actual surface roughness measurement at the top and the bottom of the kerf on the specimen (see figure 69). At higher frequencies the surface roughness improved due to the higher pulse-to-pulse overlap. The surface roughness appeared to level off at 85% pulse-to-pulse overlap. Further improvements of the surface quality with higher pulse frequencies were not significant. At higher laser pulse frequencies (>1000 Hz) the effect of the natural frequency of the striations may have been overriding the effect of pulsing the laser¹⁰⁰.

2.3.4. Effect of laser cutting parameters on recast layer thickness

The recast layer was measured by cross-sectioning, polishing and etching the sample to make the grain structure visible. The recorded value for the HAZ was averaged from three measurements evenly distributed along the cross section of the sample (see small picture in figure 66 for measurement locations). The heat affected zone (HAZ) in stainless steel consists mostly of recast. Due to the high thermal diffusion coefficient there is no visible modification of grain structure in the material that was not molten.

In order to investigate the influence of laser parameters on the recast layer (see figure 71) a variation of pulse length, pulse frequency, cutting speed and assist gas pressure was conducted. For this experiment it was important to note that the average laser power was set to the minimum for a continuous cutting process.

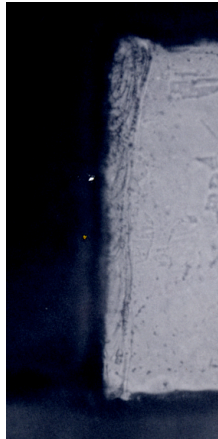


Fig. 71: Cross-section of stainless steel sample. The recast layer is visible on the left side of the sample (sample is chemical etched to make grain boundary visible).

An efficient way to determine the significant parameters that influence the recast layer was a DOE (Design Of Experiments) approach. The two-level DOE design with 4 factors is listed in the following table.

Factor	High level	Low level
Frequency:	2000 Hz	1500 Hz
Pulse length:	0.12 ms	0.060 ms
Assist gas pressure:	7.0 bar	3.5 bar
Cutting Speed:	7 mm/s	4 mm/s

Table 2.3: High and low levels for the DOE

The pulse frequencies for high and low level were set at 1500 Hz and 2000 Hz. This range was selected because it gave the good cutting quality and surface roughness in the previous experiment. The pulse length levels were set at 0.06 ms and 0.12 ms. Using shorter pulse length than 0.06 ms did not cut the material at low pulse frequency level. Pulse length longer than 0.12 ms in combination with high frequency created average laser power levels that caused overheating of the machined specimen. The pressure range was set to 7 bar on the high level and 3.5 bar on the low level. Pressures over 7 bar pushed the specimen in and out of focus at high frequency and caused

an uneven cut. At the low level below 3 bar the pressure was not high enough to remove the molten material out the kerf. The cutting speed was set at between 7 mm/s and 4 mm/s. Using a cutting speed over 7 mm/s did not cut a sample with the necessary position accuracy for a stent cutting application. The low level of 4 mm/s was the minimum acceptable cutting speed used in production to meet the throughput requirements.

The analysis of variance (ANOVA) is a statistic procedure to test for significant difference between means of variables. It is especially useful if testing more than two factors. The ANOVA does that by analyzing the variance by partitioning the total variance into the components that are random error and components that are caused by the differences between the means of the variables. The components of variance are later tested for statistical significance.

After running an analysis of variance (ANOVA analysis using statistical analysis software Statsoft™) the suggested significant model terms for this experiment were laser pulse length, assist gas pressure and cutting speed.

Model graphs based on a two level DOE are shown in the following two figures. Figures 72 and 73 shows the influence of pulse length and cutting speed on the recast at the low level (figure 72) and high level (figure 73) assist gas pressure, respectively.

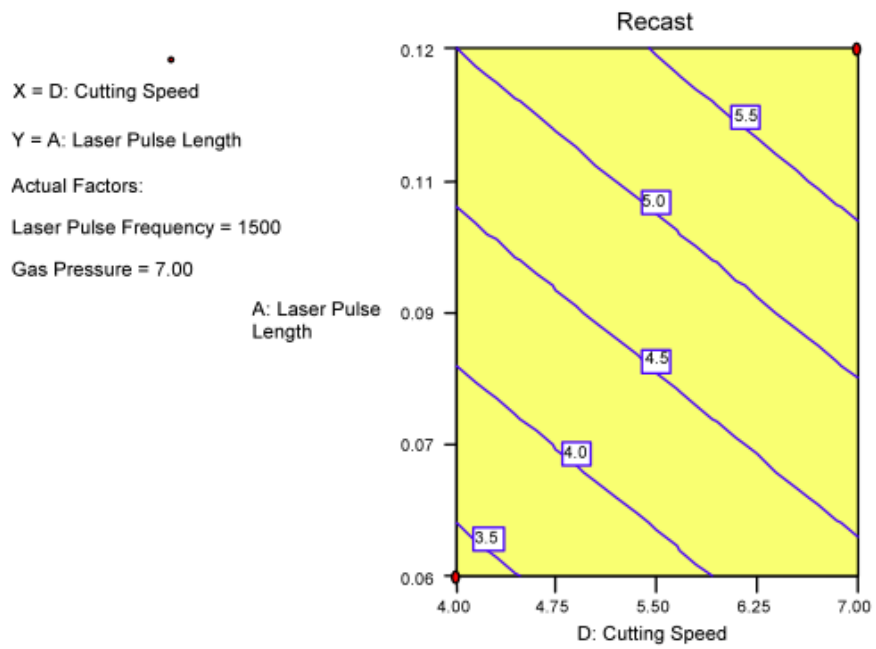


Fig. 72: Influence of laser pulse length and cutting speed on recast layer thickness (in μm) at 7 bar assist gas pressure. The recast layer thickness is labeled on the contour line.

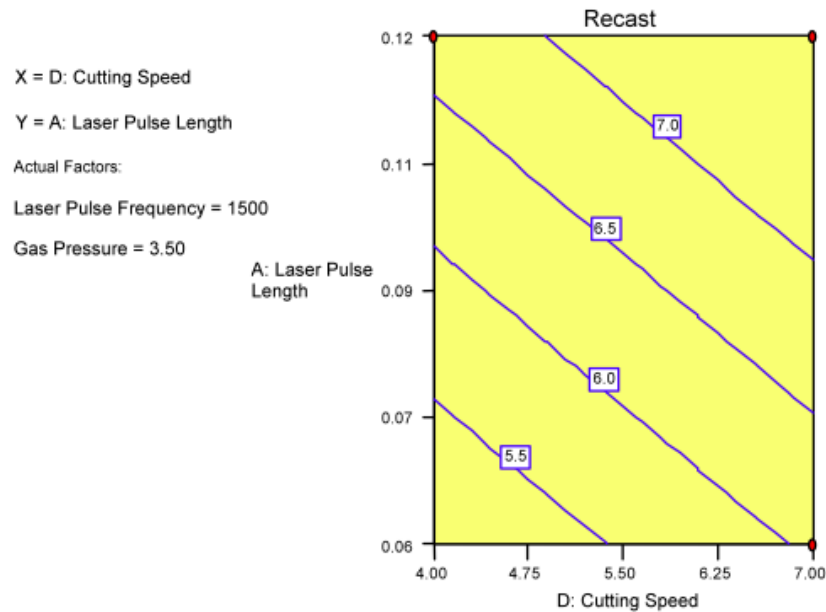


Fig. 73: Influence of laser pulse length and cutting speed on recast layer thickness (in μm) at 3.5 bar assist gas pressure.

Comparing the graphs of the two statistical models of figure 72 with figure 73 suggests that high assist gas pressure reduced the recast layer thickness significantly. The additional exothermic energy and the increased gas flow at increased oxygen pressure may remove material from the kerf before recast was formed. Figure 72 and figure 73 also suggests that shorter pulses and slower cutting speed were reducing the recast layer thickness. It needs to be noted that the average power necessary to cut at shorter pulse length or slower cutting speed was lower than at longer pulses or faster cutting speed (figure 74). This leads to the assumption that the average power level was the major contributing factor to the recast layer thickness.

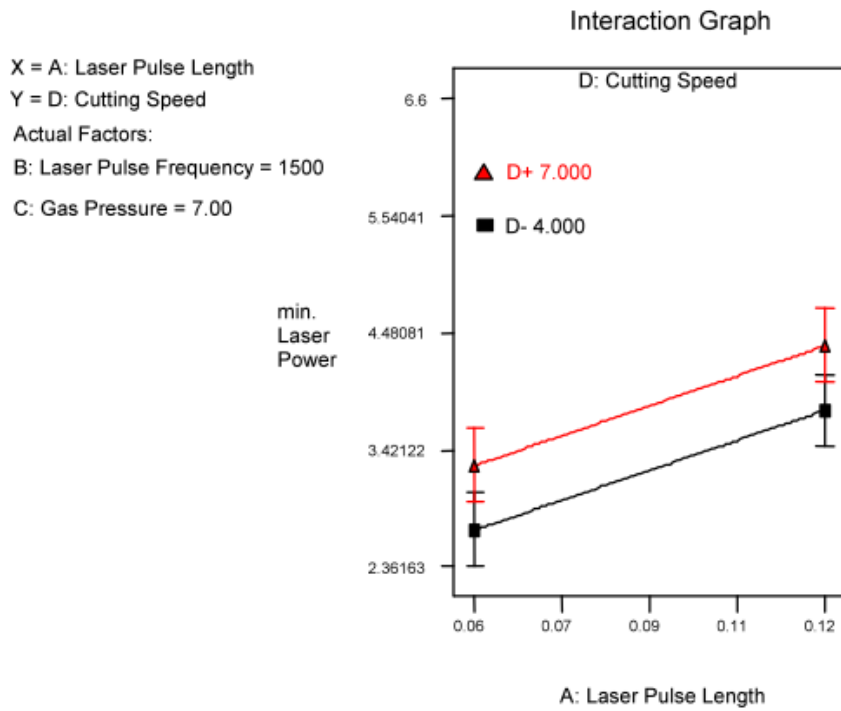


Fig. 74: Influence of Laser Pulse Length and Cutting Speed on Necessary Minimum Average Laser Power.

The two parameters that have a significant influence on the minimum power required in the experiments to cut through the 0.1 mm thick stainless steel specimen were the pulse frequency and the peak power.

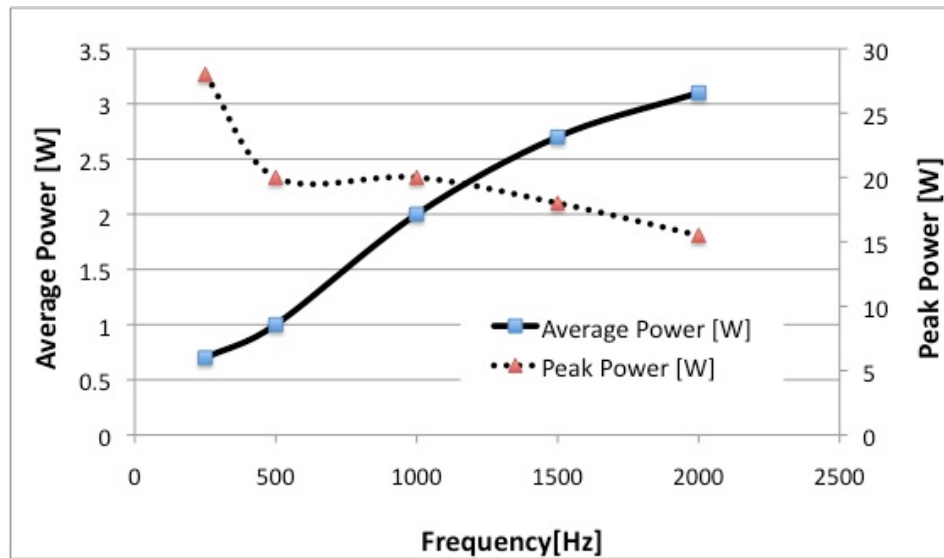


Fig. 75: Influence of frequency on minimum average power and peak power for 0.1 mm stainless steel at 6 mm/s, 6 bar oxygen pressure and 0.1 ms pulse length.

Figure 75 shows the relationship between minimum average power and peak power as a function of laser pulse frequency for the lowest average power necessary to cut through the sample. The lowest average power necessary to cut the 0.1 mm thick stainless steel sample was at low frequencies. The lowest frequency used in this experiment was 250 Hz. At this frequency the laser pulse overlap was not high enough to create a continuous cutting path and the side-wall surface quality degraded to an unacceptable level. At higher frequencies the necessary average power increased and seemed to level off at 2000 Hz. The level off of the average power at higher frequency could be explained by looking at the peak power that was used to cut at the different frequencies. At low frequencies each pulse had enough energy to cut through the specimen. At high frequencies the peak power drops to a level where more than one pulse was necessary to cut through material. This suggested that high peak power laser pulses had a better energy coupling efficiency into the cutting process.

2.3.5. Conclusion on Pulsed Fibre Laser Cutting Parameter Optimization

The results of the optimization lead to the following six statements:

- The surface quality and the thickness of the recast layer of stainless steel can be improved by optimizing the cutting parameters of the fibre laser.
- Cutting at high pulse-to-pulse frequencies that have higher pulse overlap did improve the cut quality but higher average laser power was needed to cut through the 0.1 mm thick stainless steel specimen. However, this higher average power resulted in an undesirable increase of the recast layer thickness. A good compromise of low average power and best surface roughness was at a frequency of 1500Hz, using 6 bar oxygen pressure, 6 mm/s cutting speed, 0.1 ms pulse length and 22W peak power.
- There was no significant improvement of surface roughness beyond 85 % pulse-to-pulse overlap.
- The design of experiment (DOE) of significant laser parameters suggested that shorter laser pulse length and higher assist gas pressures reduce the recast layer thickness.

2.4. Influence of Pulse Shape on Fibre Laser Cutting Results

Previous investigation showed the optimization of fibre laser microcutting parameters by adjusting pulse frequency, pulse length and laser peak power. This sub chapter shows the influence of the pulse shape on the cutting performance of the fibre laser system.

Previous experiments are also leading to the conclusion that the average power level is the major contributing factor to the recast layer thickness⁷. This could lead to the assumption that an efficient laser cutting process will create a small recast layer. Laser operation that achieves the most efficient cutting process was therefore of high interest.

2.4.1. Cutting System Setup for Pulsed Shaped Cutting

The fibre laser used for the experiments was a FL 50 from IPG. The fibre laser system was equipped with termination module that includes a collimator. The collimated beam diameter was 5 mm. The maximum continuous wave laser power was 50 W. The fibre laser had a wavelength of 1070 nm and a beam quality factor (M^2) of 1.15. The theoretically calculated focus beam waist was 0.015 mm. The actual kerf width in the 0.100 mm steel samples was measured and was in the range of 0.018 to 0.020 mm.

Due to the fact that the fibre laser has no thermal lensing effect in the active single mode fibre, the beam propagation does not change with variation of the pulse length, pulse power and frequency of the laser pulses. This will ensure that the beam waist will be at the same position during the experiments. Additionally absence of thermal lens enables power level variation during the laser pulse without changing the spot size.

The temporal pulse control was realized with an arbitrary function generator from Wavetek model 175. This function generator provided a block resolution of 8 bit for the power and time domain, allowing 255 power levels and controlling each pulse in 255 steps in each block. The fibre laser power supply uses a 0-4 V analog input to set the laser diode current from 0-4 A. The output levels of the pump diodes modulate the output power level of the fibre laser in the range of 0 to 50 W.

For the following experiments the minimum necessary average power was recorded. The definition for the minimum necessary average laser power was the power level that will enable the laser micromachining system to cut the material with given processing parameters. Previous experiments had suggested that keeping the average laser power as low as possible would result in the smallest thickness of the recast layer.

2.4.2. Influence of laser pulse shape on cutting quality

Two fundamentally different pulse shapes besides the rectangular pulse were investigated; the ramped-up and the ramped-down laser pulse. Figures 76 and 77 show the signal of the function generator input into the laser power supply and compares them with the laser output of the fibre laser for the ramped-down pulse and ramped-up pulse shape. Figure 58 previously discussed shows the same for the rectangular pulse shape.

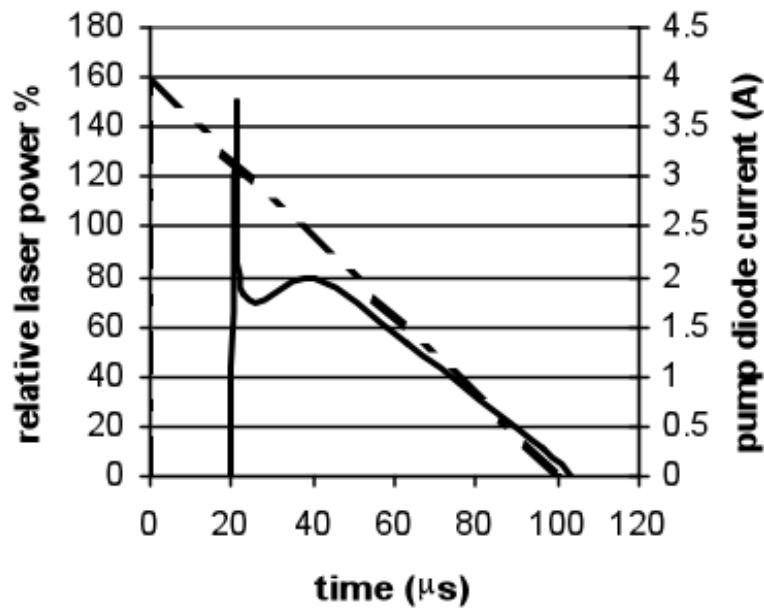


Fig. 76: Response of the fibre laser output (solid line) to ramped-down diode pumping

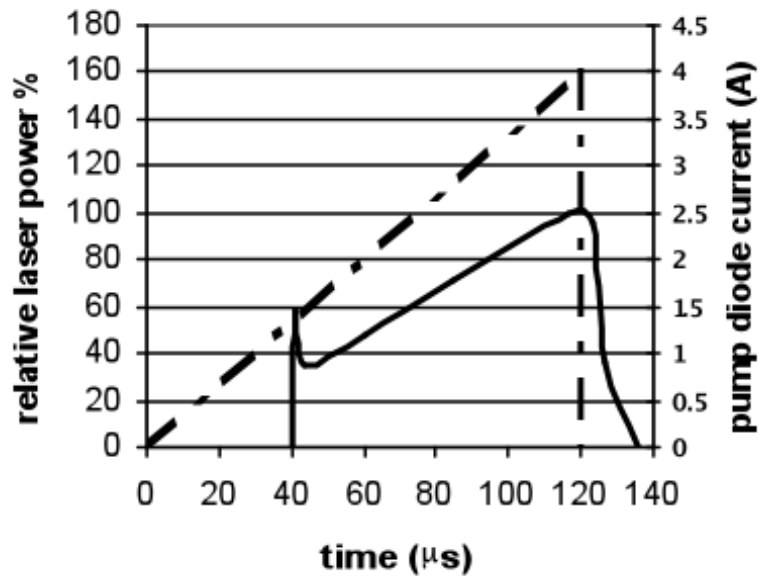


Fig. 77: Response of the fibre laser output to a ramped-up diode pumping

Similarly to the already discussed rectangular pump pulse, the ramped-down pulse in figure 76 shows the same delay and overshoot. Once stabilized the laser output power follows the pump diode current. The laser output power response in figure 77 shows a longer delay for the ramped-up pulse. This delay is caused by the increased time to get to the inversion population density necessary for the fibre laser emission at the relatively lower diode pump power during the beginning of the ramped-up pulse. The low pump power at the beginning of the laser ramp-up pulse creates less population inversion and shows therefore a similar but lower overshoot compared to the rectangular or ramped-up pulse. Once stabilized the laser output power follows the pump diode current in the same way as the other two pulse shapes.

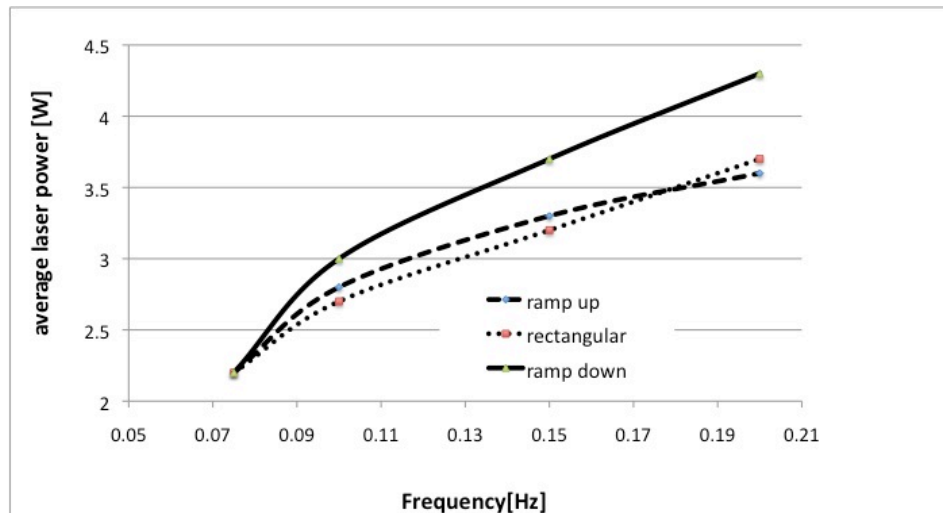


Fig. 78. : Minimum average required laser power as a function of laser pulse length for the three different pulse shapes

Figure 78 shows that the ramped-up and rectangular pulse have almost the same laser power requirement. This could be resulting from the fact that the ramped-up pulse does not start from zero laser power. After reaching a pump level where the doped fibre reaches inversion density the laser pulse starts with a spike and then continues with a certain power level (see figure 77). The ramp down pulse (see figure 76) on the other hand requires a higher average laser power. The fibre laser output in this case follows the ramp down of the diode pump and reaches a power level where it is below the damage threshold of the material in the process area. At this point the laser power is just heating up the surrounding area next to the process zone and increases the possibility of creating additional HAZ.

Laser parameters that will enable parallel sidewalls with a minimum taper are of interest. An improvement was not seen in surface finish during the evaluation of several samples cut with the different pulse shapes. A 25% reduction of the taper for the ramped-up pulse was found. The graphs in figure . 79, below, show the influence of laser pulse shape on the taper of the sidewall.

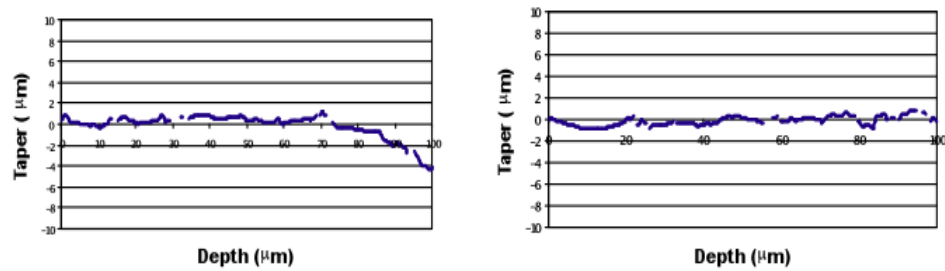


Fig. 79. : Influence of ramp-down (left) and ramp-up (right) pulses on taper.

The plots in figure . 79 were made with the optical profiler. The top or laser entrance side is at position $X=100 \mu\text{m}$ the bottom or laser exit side is at position $X=0 \mu\text{m}$. This is consistent with observations reported in other papers that a lower taper results from a linearly increasing pulse energy pattern ¹⁰⁷.

2.4.3. Conclusions on Pulse Shaping

The investigation of different pulse shapes for pulsed fibre laser cutting did not indicate that pulse shape has strong effect on the cutting and surface quality. This section concludes with only two statements:

1. Unlike the lamp pumped Nd:YAG laser it was possible to fully control the pulse shape of the Yb fibre laser with a fine resolution by the modulation of pump diode current during the laser pulse.
2. Ramping up laser pulse power during the laser cutting process reduces the taper of the sidewalls.

2.5. Position Synchronized Fibre Laser Cutting Process

The diode pump concept of the fibre laser offers excellent controllability of the laser pulse length and frequency, and the fact that the beam is generated in a single mode active fibre means that there is no change in beam quality, focus spot and focus position when output power and pulse parameters are

changed. Previous work presented in the thesis shows ways to reduce the heat affected zone (HAZ) during the laser cutting process, but this optimization was done at constant cutting speed. The speed at which the motion system moves the part will actually vary during the microcutting. This variation will be caused by the limitation of the motion system to accelerate and decelerate the mass of the motion tables, tooling and the work piece. The ability to ensure spatially uniform laser pulse separation during the cutting process could be beneficial and could lead to a more uniform HAZ. Many motion control systems offer position-synchronized outputs (PSO) that provide a pulse trigger signal proportional to the position and feed rate. This section investigates and models the effects of laser power and cutting speed on the HAZ with the novel flexibility of fibre lasers. Furthermore, it will present laser microcutting results in stainless steel using a PSO enabled motion system in combination with a single mode fibre laser.

2.5.1. Position Synchronized Fibre Laser Cutting System Setup

This section will apply the findings of the theoretical model to a real laser cutting application. The discussed application will cut small parts (in this case squares) out of a thin sheet of stainless steel.

The PSO enabled cutting system used for the experiments integrates an Aerotech X-Y motion system, fibre laser, beam collimator and a cutting head (figure 41). The cutting head incorporates a focusing optic, an assist gas nozzle and coaxial viewing optics. The output of the fibre laser was collimated to a 5 mm diameter and focused with a 50 mm focal length optic. The measured beam quality (M^2) of the fibre laser was 1.15. The focus diameter with the 50 mm focusing lens was 0.015 mm. The focus position during the experiments was experimentally set for a minimum kerf

width. The cutting process was supported by a co-axial flow of argon at 10 bar.

Figure 80 shows the schematic setup of the laser setting system used in the experiments. The main difference to the previous setup was that the pulsing of the fibre laser was controlled by the motion system controller to deliver the pulses at a consistent spatial separation.

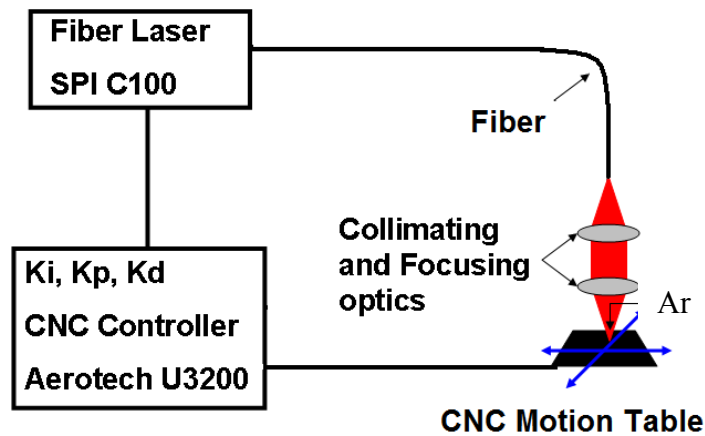


Fig. 80: Block diagram of the experimental fibre laser cutting systems with a SPI Laser 100W single mode fibre laser and Aerotech linear stage motion system with a feedback between the motion system and the fibre laser system.

2.5.2. Position Synchronized Fibre Laser Cutting Calculations and Modeling

This section will present a model to calculate the heat penetration into the sidewalls during the laser cutting process. The model is based on the energy balance of the laser cutting process by using the laser power loss due to heat conduction to estimate the heat penetration. Typically in laser melt blow cutting the laser will heat the material to the melting point and a

co-axial assist gas flow will remove the material out of the kerf. To simplify the model a stationary melt blow process is assumed. In a perfectly efficient cutting process 100% of the laser energy would be used to melt the material in the kerf. However, the efficiency of a real cutting process is limited by the loss of energy conducted into the sidewalls. Not only is this energy lost but it also creates an undesirable heat affected zone.

According to Weber and Herziger¹⁰² the minimum power to cut the material can be determined by formulating the energy balance.

$$P_{FC} = AP_L + P_R - P_{HL} - P_{PT} \quad (2.7)$$

P_{FC} is the laser power contributed to the cutting process. P is the average laser power delivered, P_R is the power that is delivered by the reactive gas and P_{PT} is the power transmitted through the kerf. The assist gas in this experiment is inert and therefore P_R is zero. P_{HL} is the power that will be lost due to heat conduction. The laser output power used during the cutting is set to the minimum therefore P_{PT} should be close to zero. The absorption of the laser light into the material is expressed by the factor A .

P_{HL} is calculated with the following formula.

$$P_{HL} = 2sk(T_M - T_0)\sqrt{Pe} \quad (2.8)$$

where s is the material thickness of the sample, k the thermal conductivity, T_M is the melting temperature of the steel and T_0 is the room temperature.

In order to calculate the heat loss, the dimensionless Peclet (Pe) number needs to be determined. Based on fluid dynamics the Peclet number can be calculated with the following equation:

$$Pe = d v / \alpha \quad (2.9)$$

Where v velocity or in this case the cutting speed, d characteristic length or in this case the beam diameter and α is thermal diffusivity.

Figure 81 shows the theoretical power loss from heat conduction into the sidewall calculated with (2.8). Based on a T_M of 1500°C and a T_0 of 20°C with k being 0.03 W/(mmK) and α of 6.5 mm²/s³³.

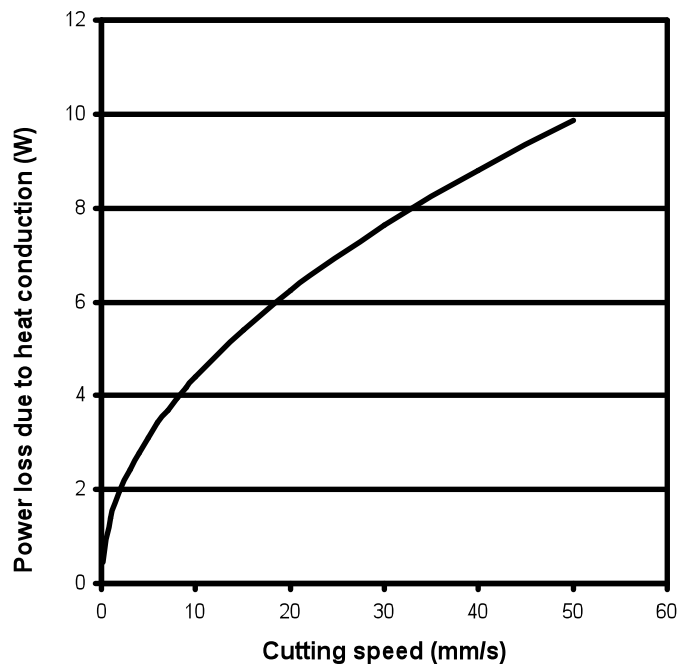


Fig. 81: Power loss due to heat conduction as function of cutting speed.

This suggests that the cutting process will be more efficient at higher cutting speed. The proportion of heat loss per unit length at increased cutting speed is getting smaller. The effect can be explained by the shorter interaction time of the laser beam with a given area of the sidewall at higher cutting speeds. The shorter interaction will limit the heat conduction into the sidewall.

Experiments have shown that the experimental cutting system was cutting 0.2 mm thick stainless steel at 50 mm/s with 50 W of average laser power. The beam diameter of the focused laser beam on the sample was 0.04 mm. Based on figure 81 the energy loss due to heat conductivity was approximately 10 W at a cutting speed of 50 mm/s. The absorption efficiency A during laser cutting with a 1070 nm wavelength laser beam is typically 0.7³³. Due to the fact that an inert gas was used for the cutting process the (P_R) reactive energy from the process gas is zero. Based on the energy balance (2.7), the power that is directly influencing the cutting process (P_c) is approximately 25 W for a cutting speed of 50 mm/s. Equation 2.8 shows that the laser power contributed to cutting the material is proportional to the energy necessary to melt a given volume of material. The volume of molten material is proportional to the cutting speed. Considering those two dependencies, the power that will directly contribute to the cutting process as a function of cutting speed can be plotted (figure 82).

Additionally, the power setting to sustain the cutting process for the fibre laser system can be calculated and is also plotted in figure 82.

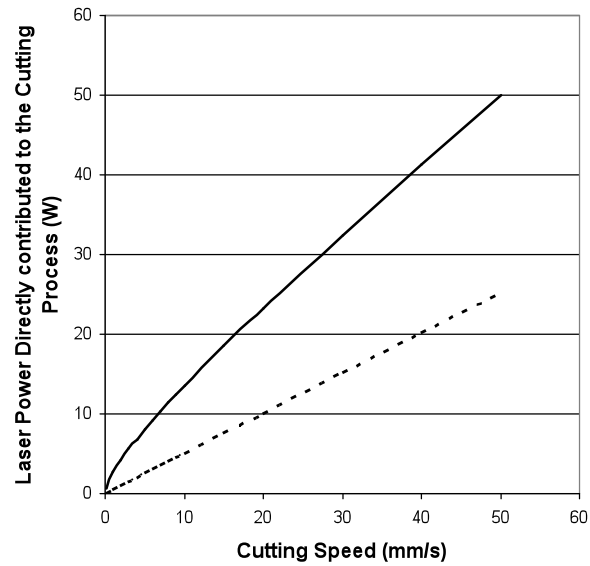


Fig. 82: Laser power contributed directly to the cutting process (dashed line) and laser power setting (solid line) at laser system.

Based on the plot in figure 82 a linear change of laser power with cutting speed is a good fit for the theoretically necessary power to cut the discussed stainless steel samples. The motion system was therefore set up to trigger laser pulses from the fibre laser proportional to the cutting speed. This setup creates uniform laser pulse spacing over the sample during the cutting process.

The power loss due to heat conductivity has an impact on the heat penetrating the material. To measure the heat penetration, the effect of surface oxidation was used as an indicator for the temperature. Even with an inert gas to assist the cutting process, there is oxygen present in the cutting area. Venturi effects pull in air from the surrounding area so that the stainless steel used for the experimental work forms an oxide layer on the surface after it is heated to a certain temperature. The assist gas just blows out the molten material and is not completely shielding the sample

from all oxidation. A brownish coloured oxide layer develops when the stainless steel is heated to around 600°C. This brownish colour can be easily identified and was used to compare real cutting results with the model. Therefore the following calculation of the heat penetration to the 600°C point is of interest.

The following formula describes the heat penetration as a function of processing speed.

Using the heat diffusion factor c_p the mass m_{600} that can be heated to a given temperature T (in this case 600°C) can be calculated with the following formula.

$$m_{600} = \frac{P_{HL}}{c_p T} \quad (2.10)$$

P_{HL} is the power loss due to heat conduction during the cutting process that was calculated with (2.7).

Furthermore, after introducing the material density of stainless steel ρ the volume heated to 600°C can be calculated with the following equation:

$$V_{600} = \frac{m_{600}}{\rho} \quad (2.11)$$

At this point, the heat affected zone (HAZ) can be calculated with following formula.

$$HAZ_{600} = \frac{V_{600}}{2A} \quad (2.12)$$

Where $2A$ is the projected area of the laser beam on both sidewalls.

The formulas will lead to the heat penetration and therefore the results will be an indicator for the size of HAZ. The plot in figure 83 illustrates the theoretical heat penetration to 600°C as a function of cutting speed.

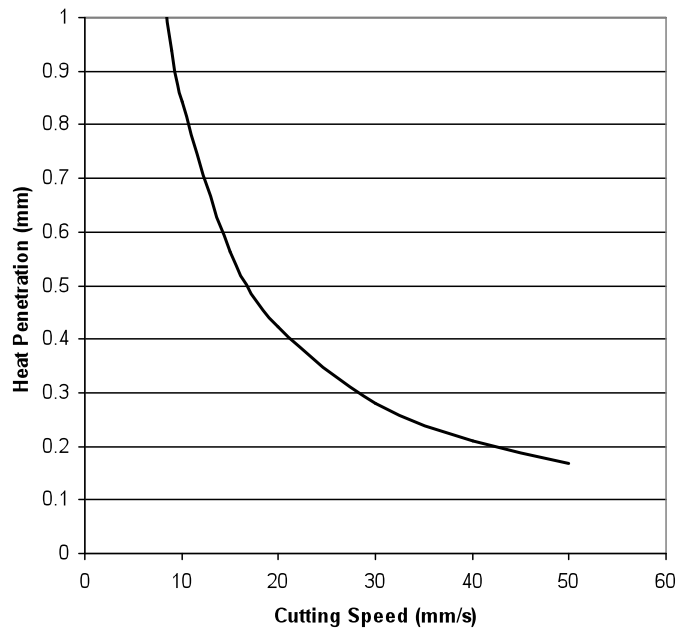


Fig. 83: Heat penetration to 600°C as a function of cutting speed based on the energy lost through heat conduction resulting from the energy balance for 50W of fibre laser power and a power loss due to heat conduction of 25W.

This plot suggests that if the power during the laser cutting process stays constant the heat penetration and therefore the HAZ will increase significantly at lower cutting speed. Especially for complex cutting patterns in micromachining the cutting speed needs to slow down in order to limit position errors from the motion system.

2.5.3. Position Synchronized Fibre Laser Cutting Process Results and Discussion

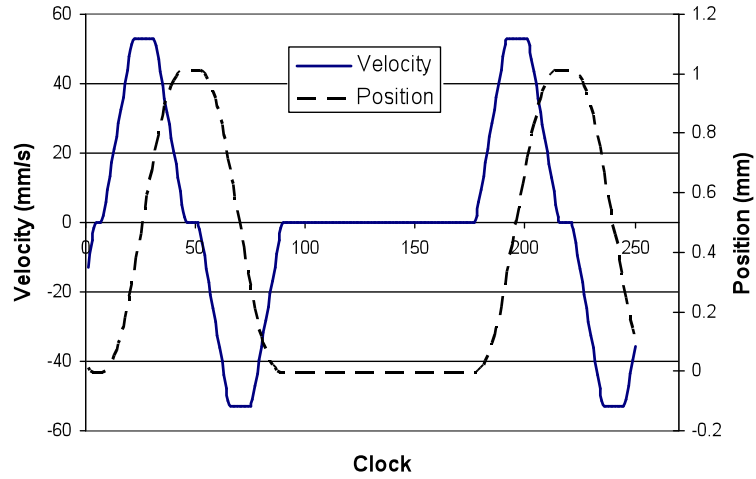


Fig. 84: Velocity and position as a function of the timing (Clock signal in ms) of the CNC motion system

For the cutting experiments the laser pulse-to-pulse frequency and therefore the average laser power will be reduced linearly with the cutting speed or cutting velocity. Figure 84 and figure 85 show how the cutting speed was changing during the cutting process.

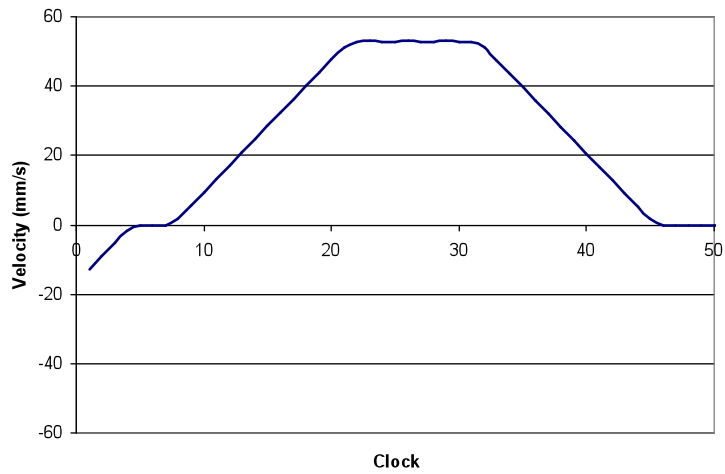


Fig. 85: Velocity as a function of the timing signal of the CNC system

Figure 85 shows just one acceleration and deceleration cycle during the laser cutting process. Figure 86 shows the laser pulsing during the acceleration and deceleration process. The slower areas around the corners of the square will be cut at a slower speed and lower pulse frequency. The lower pulse frequency will reduce the duty cycle and therefore the average laser power.

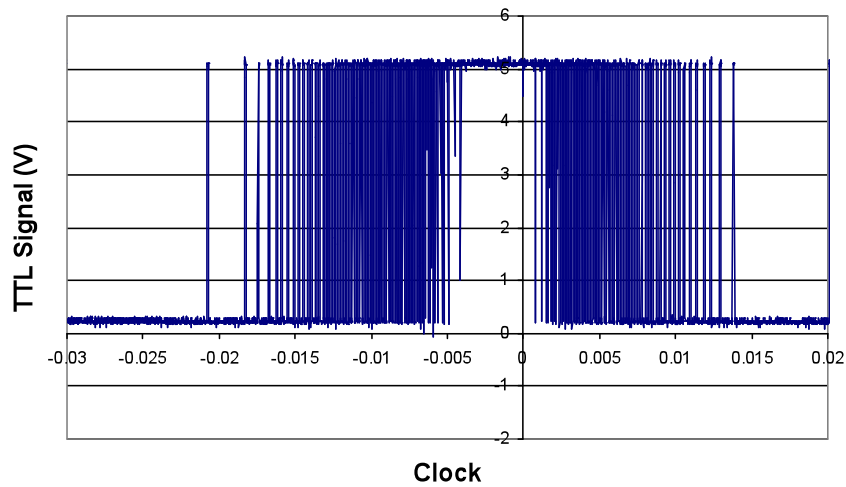


Fig. 86: Pulse train during PSO controlled acceleration and deceleration as a function of timing (Clock signal in ms).

2.5.4. Laser Cutting Results for Pulsed Synchronized Cutting

For the following experiments it is necessary to note that the beam quality needs to stay constant during the variation of the laser power. A change in beam quality will result in a variation of the laser cut kerf and the thermal lensing of the active material will shift the focus position of the laser in the sample. Typical Nd:YAG based laser cutting systems will show a variation in beam quality with average laser power. This variation of beam quality is a result of thermal lensing effects in the active material in the Nd:YAG laser. The fibre laser typically does not show thermal lensing that will have an influence on the cutting process.

Figure 87 shows a laser machined path cut at constant laser power. Due to the fact that the cutting speed was slower at the corners the heat affected zone was wider. The measured width of the 600°C zone at a cutting speed of 50 mm/s zone was approximately 0.15 mm (marker A, figure 87) and corresponds with the model.

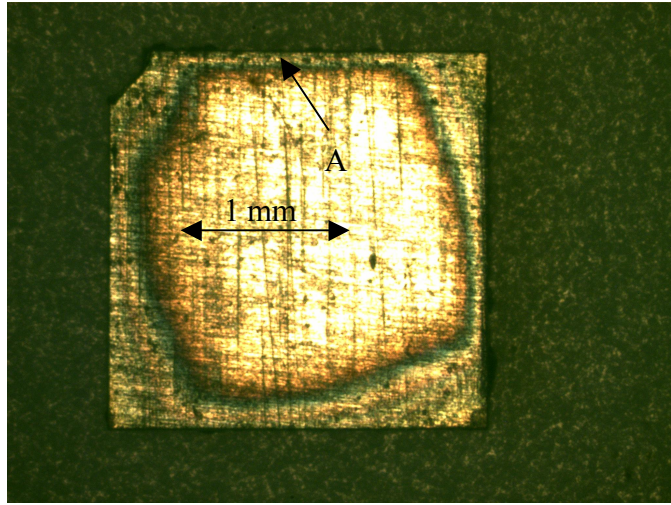


Fig. 87: Sample of a fibre laser cut without PSO.

Reducing the laser beam interaction time in those corners is beneficial. The PSO enabled motion system dynamically lowered the pulse-to-pulse frequency in the areas with reduced cutting speed.

Figure 88 shows a similar cutting path with the same cutting speed utilizing the pulse and speed synchronized cutting process.

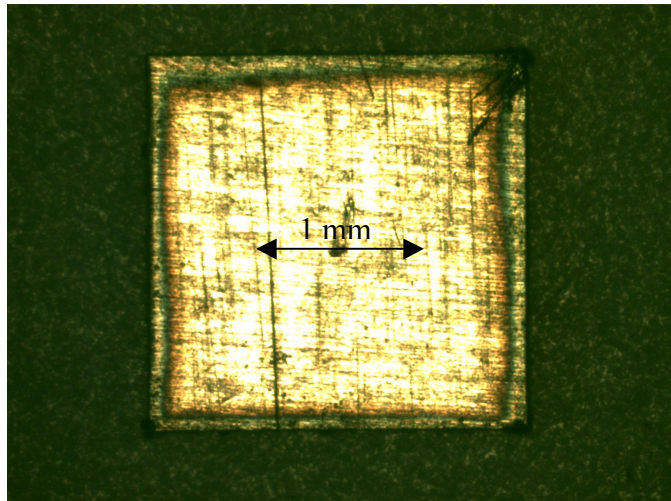


Fig. 88: Picture of a sample laser cut with PSO.

2.5.5. Conclusion on Pulsed Synchronized Cutting

Changing the laser average power linearly with the changing cutting speed optimized microcutting of complex patterns.

1. The experiments successfully dynamically adapted the laser pulse-to-pulse frequency to optimize the average laser power for changing cutting speeds.
2. The mathematical model estimated accurately the HAZ and provided average laser power settings successfully applied for initial cutting experiments.
3. The results from those cutting experiments show a significant improvement in uniformity as well as a minimization of the heat affected zone.

3. Fibre Laser for Microwelding

Many applications in the electronics, telecom and medical device industries require increasingly smaller laser joining areas. Some welding applications require focus spot diameters less than 50 μm and pulse energy levels as low as 10 mJ. The fibre laser's excellent single mode beam quality provides the desired spot size and laser power density. In addition many emerging microwelding applications require excellent power stability at low pulse energy levels to provide sufficient process yields. This chapter will provide data about the power stability of pulsed fibre lasers and will show microwelding results for a selection of materials with pulsed and CW fibre laser systems. The pulsed process is preferably used where the geometries are relatively small and the process speed is slow. A CW welding process is not recommended in such cases because at low feed rates the power necessary to weld the material would also damage the part or nearby components. On the other hand CW welding does enable higher processing speeds and could be useful for applications that will have a demand for high throughput.

3.1. Fibre Laser Welding Experimental Setup

The welding systems used for the experiments integrated a 100W fibre laser from SPI, a beam collimator and a processing head (figure 89). The processing head included a focusing optic. The output of the fibre laser was collimated to a 5 mm diameter and focused with a 165 mm focal length optic in the scanner. The measured beam quality (M^2) of the fibre laser was 1.15, therefore the focus diameter with the 165 mm focusing optic was 0.050 mm. The focus position during the experiments was set on the top of the sample. The welding area was shielded with a constant flow of argon from a gas nozzle.

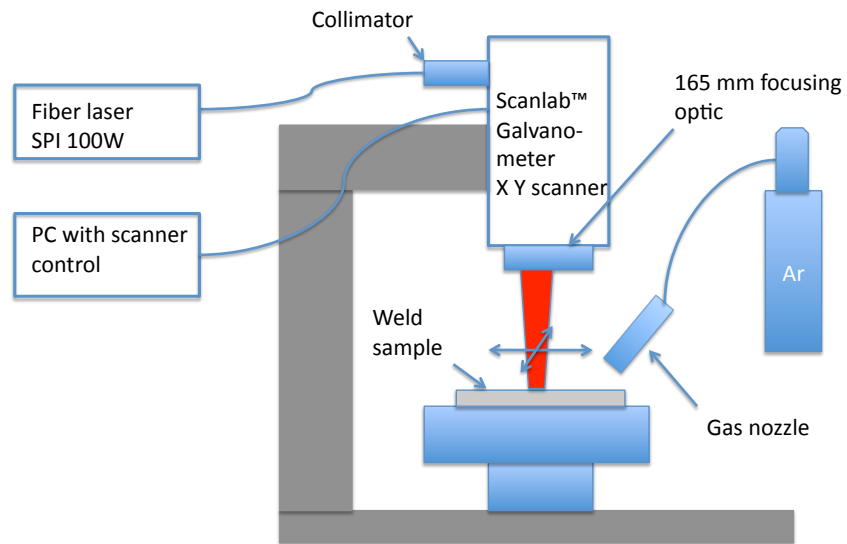


Fig. 89: Experimental setup of the continuous wave fibre laser welding system.

For the continuous wave operation welding experiments a faster galvanometer mirror system from Scanlab was used instead of a standard motion system with mechanical stages (see figure 90). The HurrySCAN-15™ scanner maximum writing speed was 1000 mm/s^{103} and was sufficiently fast for the following experiments. The protection gas was delivered with an off-axis gas nozzle.

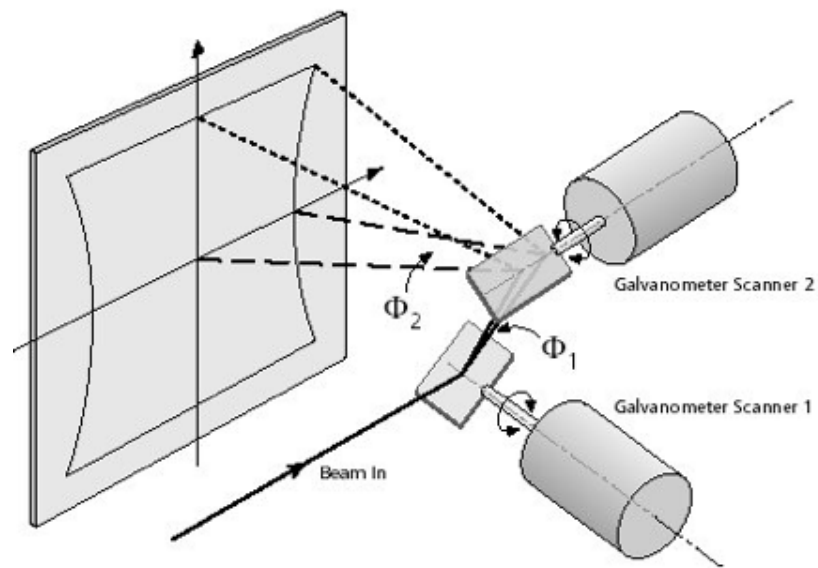


Fig. 90: Two axis galvanometer scanner setup from SacnLab™.

The 165 mm focusing optic was a special flat-field aplanatic lens that compensates for off-axis lens errors.

For the pulsed welding experiments with the fibre laser the feed rates were significantly lower and the galvanometric scanner was replaced with a welding head and an X-Y motion table with CNC controller (Aerotech N3200). Figure 91 shows an image of the pulsed welding system. The laser system was switched by pulsing the pump diodes with a function generator (HAMEG 8130).

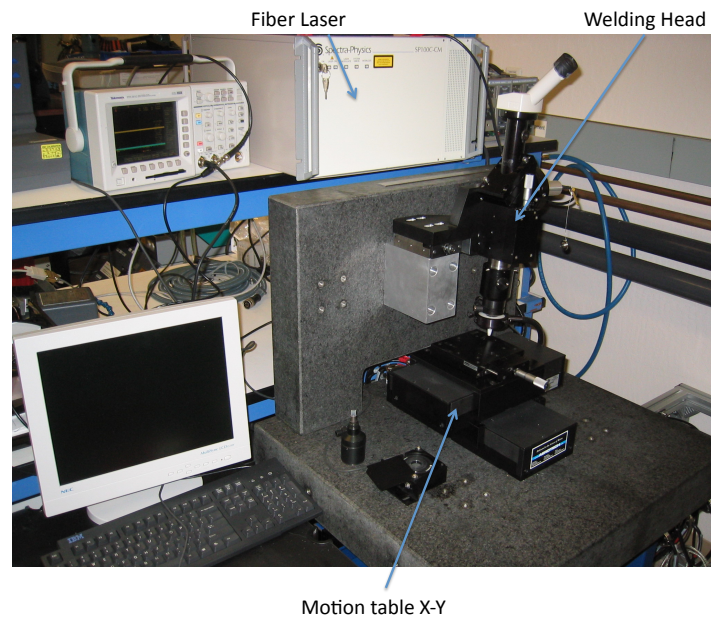


Fig. 91: Picture of the Experimental Pulsed Welding System.

The welding head used for the pulsed experiments included a focusing optic, an on-axis assist gas nozzle and coaxial viewing optics. The welding head from LaserMech Inc. TM in figure 92 was 10 degrees tilted away from the processing direction to avoid back reflection and potential damage to the fibre termination module.

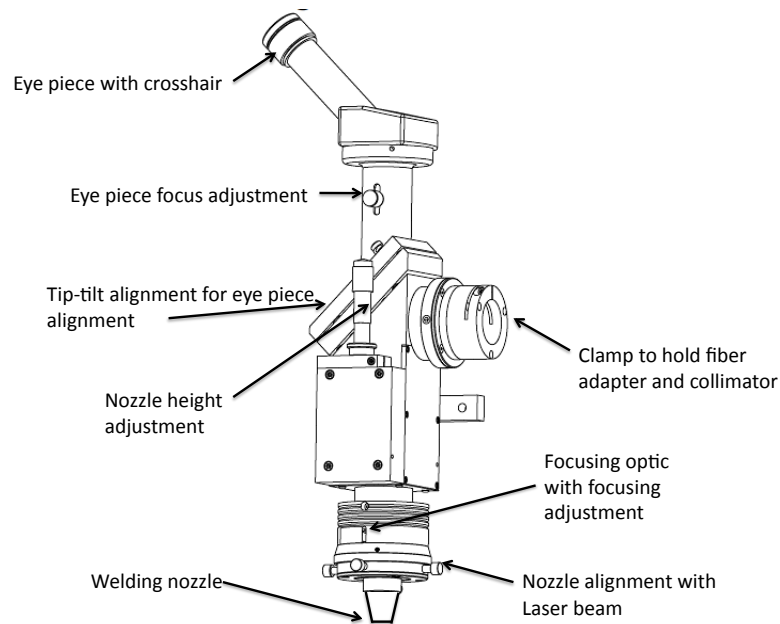


Fig. 92: Welding head from LaserMech™ for pulsed welding with a fibre laser.

3.1.1. Material and Assist Gas for the Welding Experiments

Continuous wave welding (CW) processes were investigated for two different materials: stainless steel and titanium.

The steel welding samples were made of 304 series steel. Grade 304 is a standard grade austenitic steel known to have excellent welding characteristics. The chemical composition of 304 series steel is:

Fe, < 0.08% C, 18% Cr, 8% Ni, 2% Mn, < 0.1% N, < 0.75% Si, < 0.045% P, < 0.03% S

Grade 1 titanium is widely used as the encasing material for pacemakers. It has excellent biocompatibility, similar to 316 series steel. The chemical composition of the grade 1 titanium used for the welding experiments is:

Ti, <0.08% C, <0.03% Fe, <0.03% N, <0.18% O, <0.015% H

The process gas was supplied from a cylinder of argon for all the welding experiments. The two-stage gas regulator used enabled a gas pressure range of 0.5 to 3 bar with 0.1 bar resolution. The volume of the flow of argon was monitored with a floating ball flow meter.

In order to measure the weld width and weld penetration the specimens were cross-sectioned, polished and etched to make the weld zone visible. A standard microscope (figure 93) with a camera from Bausch and Lomb (model Microzoom™) was used to document the weld samples. The measurement of the weld geometries was calibrated by an image of a scale.



Fig. 93: Bausch and Lomb microscope with camera that was used for the weld geometry measurements.

3.2. Continuous Wave Welding with Fibre Laser Experiments

3.2.1. Welding of Stainless Steel with CW Fibre Lasers

In order to investigate the effect of the processing speed on the weld performance the feed rate was varied. The range of the feed rate for the welding system was from 25 mm/s to 300 mm/s. The following image (figure 94) shows a top view of bead-on-plate weld samples that were used to measure the weld width. This shows an example of a series of laser welds of stainless steel with the fibre laser at 100 W by using the CW welding process at three different speeds: 25 mm/s, 50 mm/s and 75 mm/s.

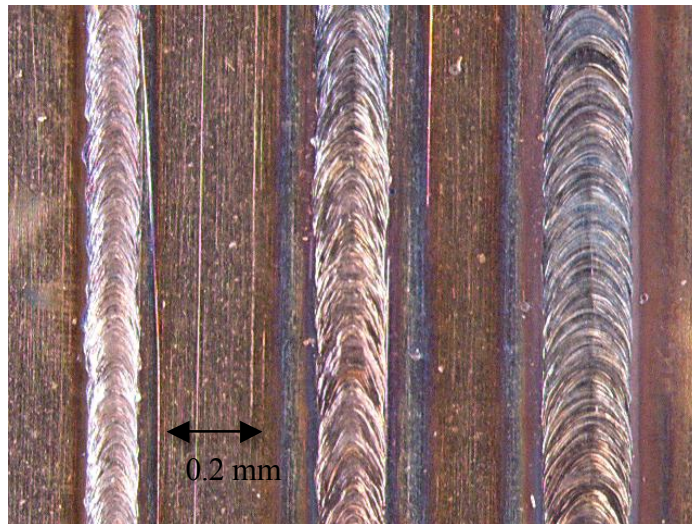


Fig. 94: Top view of fibre laser CW weld beads in stainless steel at 100W peak power for 75 mm/s, 50 mm/s and 25 mm/s weld (left to right) speed and argon shielding.

The following plots (figure 95) show the weld width for four different power levels in stainless steel for a range of different processing speeds. The power levels used in the experiments were 40 W, 60 W, 80 W and 100 W.

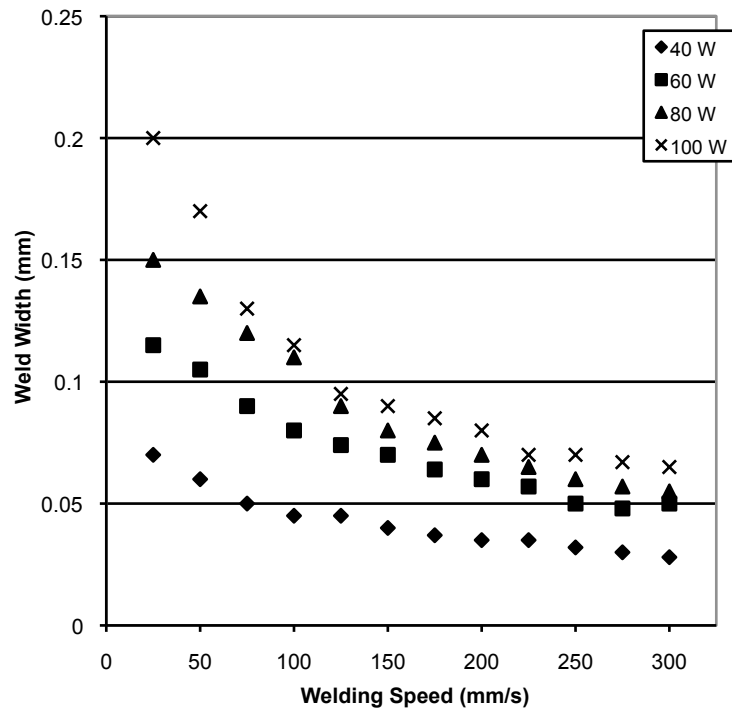


Fig. 95: Weld width as a function of welding speed and laser power for stainless steel (304 Series) with argon shielding.

Figure 95 shows that at the maximum power level of 100 W and a welding speed of 25 mm/s the weld width in stainless steel was 0.2 mm. The 100W power level created a 0.07 mm wide weld area at the highest speed of 300 mm/s. At the 40 W power level and 300 mm/s speed the weld width decreased to 0.03 mm. The change in weld width follows a non-linear decrease with increased welding speed for all power levels. The non-linear behaviour appears more pronounced at higher laser power.

As well as the weld width, the weld penetration for these samples was measured by cross-sectioning, polishing and etching with 3 % nitric acid in a methanol carrier (figure 96). Figure 97 shows the results for CW welding of stainless steel.

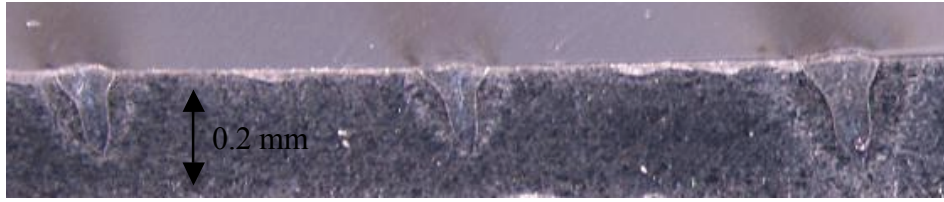


Fig. 96: Cross section of fibre laser CW weld beads in stainless steel at 100W peak power for 100 mm/s, 125 mm/s and 150 mm/s weld speed (right to left) and argon shielding.

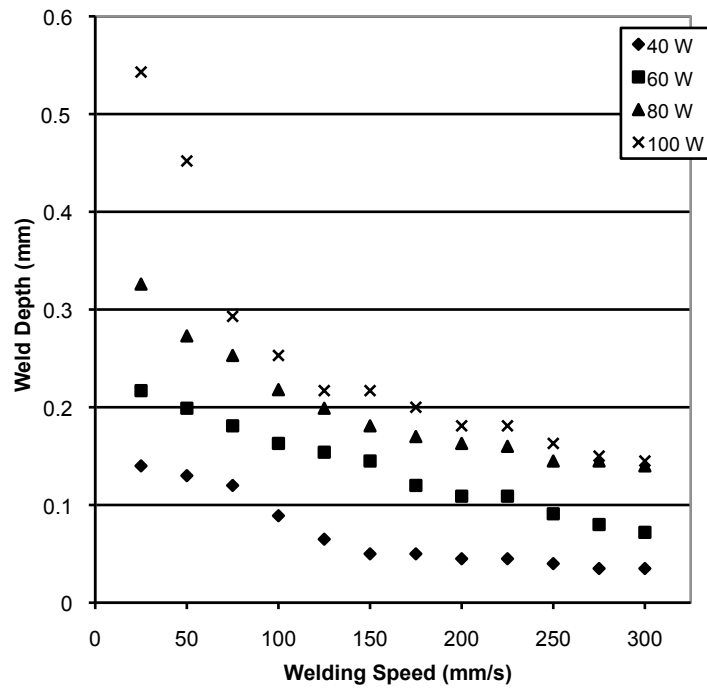


Fig. 97: Weld penetration depth as a function of welding speed and laser power for stainless steel (304 Series) with argon shielding.

Figure 97 shows that the maximum weld penetration depth in stainless steel at 25 mm/s with 100 W laser power was 0.54 mm. At a weld speed of

300 mm/s a weld penetration depth of 0.15 mm was still possible.

Comparing figure 97 to figure 95 it seems that at high laser power the weld width to weld depth ratio approaches that of keyhole welding (see figure 96). The decrease of weld penetration depth slows down at higher feed rates. This non-linear decrease appears to be similar to the effects described in the papers on the SHADOW^{104 105} weld process.

In order to see if the weld performance in stainless steel can be modelled to predict the laser power requirements the weld performance for one power setting was selected. The 100 W laser power setting was selected because the weld nugget showed the most characteristic shape of a keyhole weld.

Using the analytical keyhole welding process for line sources introduced in the literature review (1.13),

$$0.483P_L = v_S 2r_W t_S C_P \rho T_M \quad (2.13)$$

where,

P_L = absorbed laser power [W],

0.483 is the factor that's accounts for loss due to conduction (based on Swift-Hook and Gick)

v_S = welding speed [m/s],

$2r_W$ = weld width based [m],

t_S = weld penetration or depth [m],

ρ = material density = 8030 kg/m^{3 31}

C_P = specific heat = 620 J/kgK (average from room temperature to melting temperature¹⁰⁶),

T_M = melting point of 304 steel = 1527 K³¹

Using this formula and the data in figure 97 and 95 for weld width and penetration versus weld speed, the absorbed laser power P_L is approximately 50W on average over the 12 different weld speeds, not the actual 100W laser power setting. The difference can be partially explained by an estimated absorption efficiency of 80-90% and by the fact that this model does not include the heat of fusion necessary to melt the material.

With the inclusion of the power required for melting P_F ,

$$P_F = v_S 2r_W t_S \rho \Delta h_m \quad (2.14)$$

and a typical value of $\Delta h_m = 300 \text{ kJ/kg}$ ³¹ it is estimated that the latent heat of fusion will require an additional 10-12W (in average for the 12 different weld speeds). If the effect of heat conduction shown in formula 2.13 is also included, this means an additional 21-25 W of power is required to weld cross-sections seen with the 100 W of laser power. Therefore adding the predicted 50 W and the power for the heat of fusion, and considering an absorption efficiency of 80%, the theoretical laser power is in the range of 90-95 W for the 100 W experiments. This reasonable agreement suggests that this model can be used to estimate the power requirements for micro-welding.

3.2.1. Welding of Titanium with CW Fibre Lasers

In order to show the weld performance of the fibre laser for other materials, titanium was welded with the same operation conditions as the stainless steel.

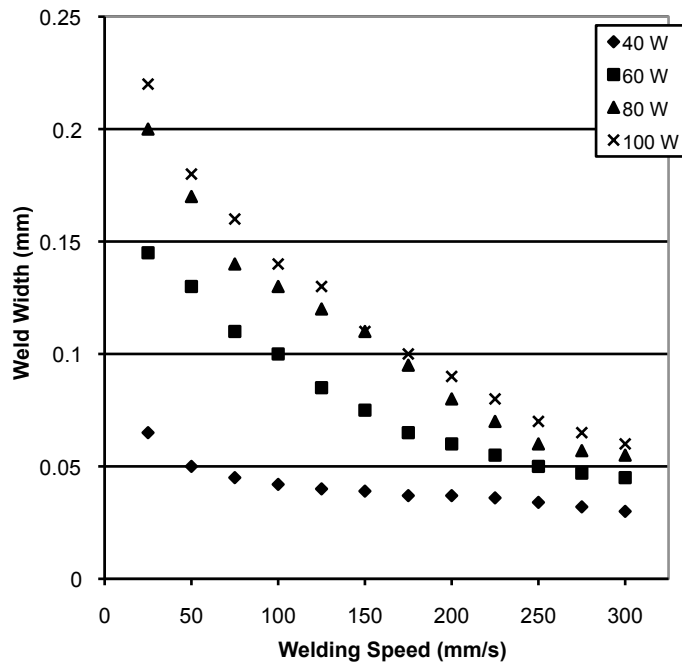


Fig. 98: Weld bead width as a function of welding speed and laser power for titanium (Grade 1) with argon shielding.

Figure 98 shows that the weld width in titanium was very similar to the weld width in stainless steel. On average the weld width was 10-20% wider in titanium than in stainless steel. The relationship between weld speed and weld width appears to be more linear than in stainless steel.

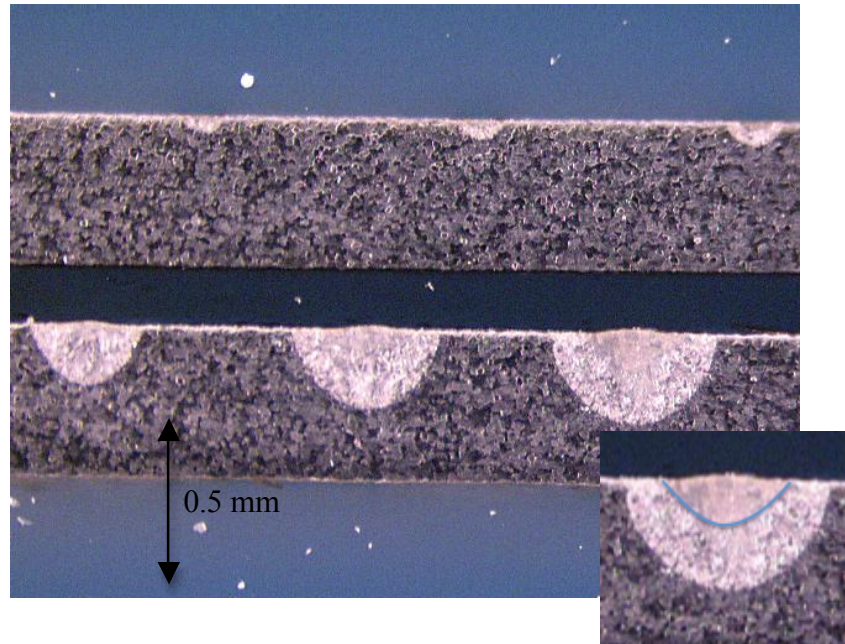


Fig. 99: typical cross section of a fibre laser CW weld after etching the titanium sample to make the weld zone visible. Insert with blue line indicating actual melted areas.

Figure 99 shows a cross section of welds in titanium. The insert in figure 99 shows that the cross-section has two areas, the actual melted material and the surrounding HAZ that was not melted. The HAZ for the CW welding process was significantly wider than in stainless steel. At the 100 W power level and 25 mm/s weld speed for example, the HAZ was 0.35 mm, but the weld width was only 0.22 mm. This effect can be explained by the lower heat conductivity of titanium compared to stainless steel (a factor of two lower).

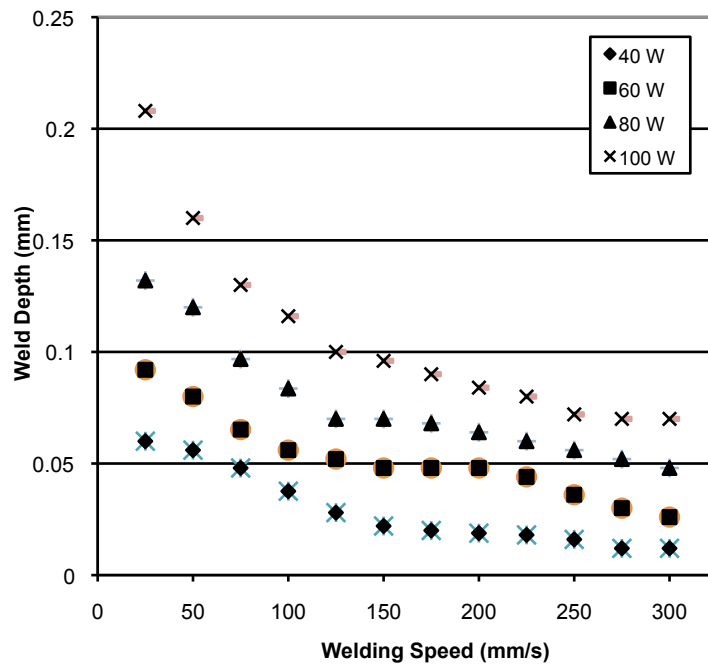


Fig. 100: Weld penetration depth as a function of welding speed and laser power for titanium (Grade 1) with argon shielding.

Figure 100 shows the variation of penetration depth in titanium for different welding speeds. The penetration depth follows the same decrease with increased welding speed as seen with stainless steel. The maximum penetration depth based on the HAZ at 25 mm/s is 0.21 mm at 100W laser power. At 300 mm/s a penetration depth of 0.07 mm is still obtainable.

In order to see if the weld performance in titanium can also be modelled to predict the laser power requirements, the weld performance for the 100W power setting again selected.

The analytical keyhole welding process model for line sources introduced in the literature review by applying the formula 1.13 in the case of stainless welding was again used but with material parameters for titanium:

$\rho = \text{material density} = 4510 \text{ kg/m}^3$ ³¹

$C_p = \text{Specific Heat} = 519 \text{ J/kgK}$ ³¹

$T_M = \text{melting point of titanium} = 1668 \text{ K}$ ³¹

Based on the weld width and penetration versus weld speed in titanium, the absorbed laser power P_L is approximately be 15W on average over the 12 different weld speeds, not the actual 100W laser power setting.

With the inclusion of the power required for melting P_F , as used in 2.14 and a typical value of $\Delta h_m = 437 \text{ kJ/kg}$ ³¹ the latent heat of fusion to melt titanium will be 7-8 W (on average over the 12 different weld speeds). Adding the power for the heat of fusion and the absorption efficiency, the theoretical laser power should be in the range of 22-23W for the 100W experiments. An explanation for this difference could be the fact that the 0.483 factor in formula 2.13 is appropriate for keyhole welding. However the titanium weld bead aspect ratio of weld width to weld depth suggests a conduction welding process. Therefore the absorbed power for melting should be below the 48.3% of the total absorbed power. If a keyhole is not present the absorption efficiency of titanium is only about 45%²⁴ in the wavelength range of a fibre laser (1070 nm). In addition the titanium forms a significant plasma plume over the work piece diffusing and shielding part of the laser beam. The experiments suggest that about 75% of the laser power was not used for melting the titanium and was lost due to the above-mentioned reasons.

3.2.2. Conclusions on Continuous Wave Fibre Laser Welding

1. The fibre laser, due to its good beam quality, is able to achieve very small focus diameters for microwelding applications.

2. The weld penetration and weld bead width was sufficient for many welding applications.
3. Continuous wave operation in stainless steel achieved penetration depths of 0.55 mm at 25 mm/s welding speed and 100 W laser power.
4. At the maximum tested weld speed of 300 mm/s during CW operation the weld penetration was 0.15 mm for stainless steel at 100 W laser power.
5. The theoretical analytical keyhole model with a line source solution can be used to estimate the laser power if the latent heat of fusion and the absorption efficiency are considered.
6. Continuous wave operation in titanium achieved penetration depths of 0.21 mm at 25 mm/s welding speed and 100W laser power.
7. At the maximum tested weld speed of 300 mm/s during CW operation the weld penetration was 0.07 mm for titanium at 100W laser power.
8. Under the experimental conditions based on heat flow modeling, only about 25% of the laser power couples into the process of welding titanium, while 75% of the laser power couples into the process of welding stainless steel. Under these conditions the welding of titanium required approximately three times the power of stainless steel welding for a given weld cross-section.

3.3. Pulsed Fibre Laser Welding Process

3.3.1. Background on Pulsed Fibre Laser Welding

In order to have a higher weld penetration at a lower average power, pulsed laser operation was applied. The gated CW fibre laser provided pulsed laser operation with good power stability.

Toensdorf et al. ⁵³, Miyamoto et al. ⁵⁵ and the previous sub-chapter describe the welding performance of fibre lasers in continuous wave operation. This thesis presents welding results with a 100W Spectra-Physics fibre laser in pulsed operation (Spectra Physics distributed the SPI 100W fibre laser in the first year). This investigation aimed to show that the fibre laser was able to weld stainless steel and titanium for microwelding applications. Specifically of interest was the welding process that hermetically sealed the cans of medical pacemakers. The laser pulse energy stability required to avoid damaging the internal components of the pacemakers during the weld process was investigated.

3.3.2. Experimental Work on Pulsed Fibre Welding

The welding experiments were shielded with a constant flow of argon. The welding feed rate was constant at 4 mm/s. This particular welding speed was dictated by the throughput requirements of the pacemaker production. There was no variation of welding speed or coaxial argon assist gas flow during the welding experiments.

Pulsed operation was obtained by gating the laser with an external pulse generator (Hameg HM8130). Figure 101 shows a typical 2 ms long individual pulse of the fibre laser.

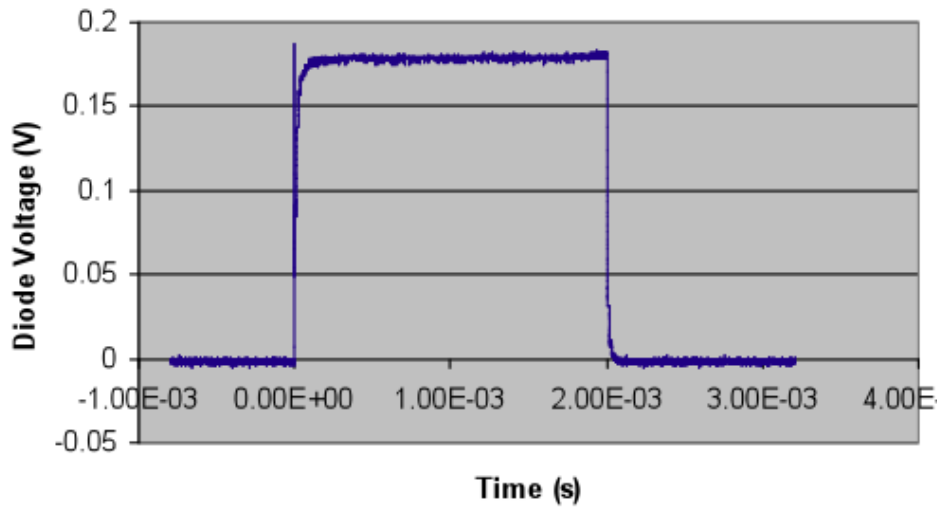


Fig. 101: Temporal behavior of a typical fibre laser pulse for laser welding measured with a Tektronix TDS 3032B 300 MHz digital oscilloscope and a Thorlabs (DET410/M) InGaAs photodiode with a 0.5 ns response time.

Gating the pump diodes pulses the fibre laser. In the same way as the already-discussed pulsed fibre laser for cutting applications, the Yb-doped fibre laser typically starts to lase approximately 0.025 ms after the laser trigger signal; the laser output power then stabilizes at a stationary value after an initial spike caused by relaxation oscillation in the lasing media of the fibre. The initial spike duration was <0.001 ms. The pulse length used for welding applications was typically longer than a laser pulse for cutting applications. The initial spike overshoot was significantly smaller at these longer welding pulse lengths compared to the shorter cutting pulse lengths.

3.3.3. Welding of Stainless Steel with Pulsed Fibre Lasers

First welding experiments used stainless steel (304 Series). The laser beam was focused on the top surface of the sample. For the following experiments the frequency and pulse length were kept constant. Figure 102 shows a typical cross section after etching the stainless steel sample to

show the weld zone. For better visibility of the heat affected zone the boundary between the re-solidified weld metal and the non-melted material is highlighted.

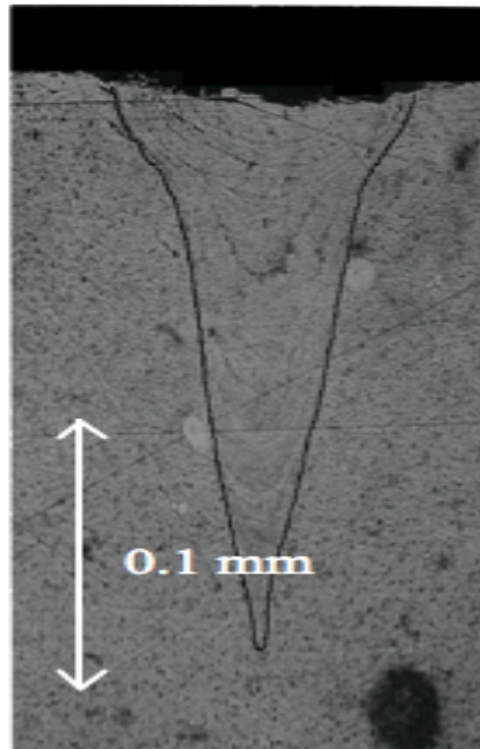


Fig. 102: Typical cross section of a fibre laser weld after etching the steel sample to make the weld zone visible.

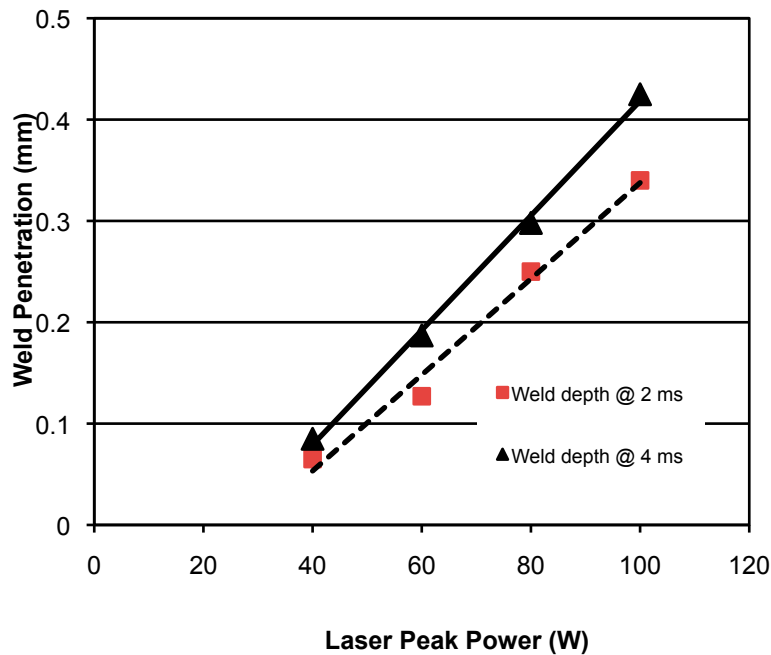


Fig. 103: Weld penetration depth in stainless steel as a function of laser peak power for 200Hz pulse-to-pulse frequency and 4 mm/s weld speed with argon shielding gas.

Figure 103 shows how the weld penetration depth changes with peak power and pulse length. The laser setting for this experiment was 200 Hz pulse-to-pulse frequency and 4 mm/s weld speed. The shield gas was a coaxial flow of argon. For the peak power range used in this experiment the weld penetration was changing linearly with the peak power. At 40 W peak power and 2 ms pulse length the weld penetration was 0.065 mm. The highest investigated energy level was 100 W peak power, and a 4 ms pulse length resulted in a weld penetration of 0.43 mm. The slope of weld penetration over laser peak power for the 4 ms pulse length is steeper than for a 2 ms pulse length.

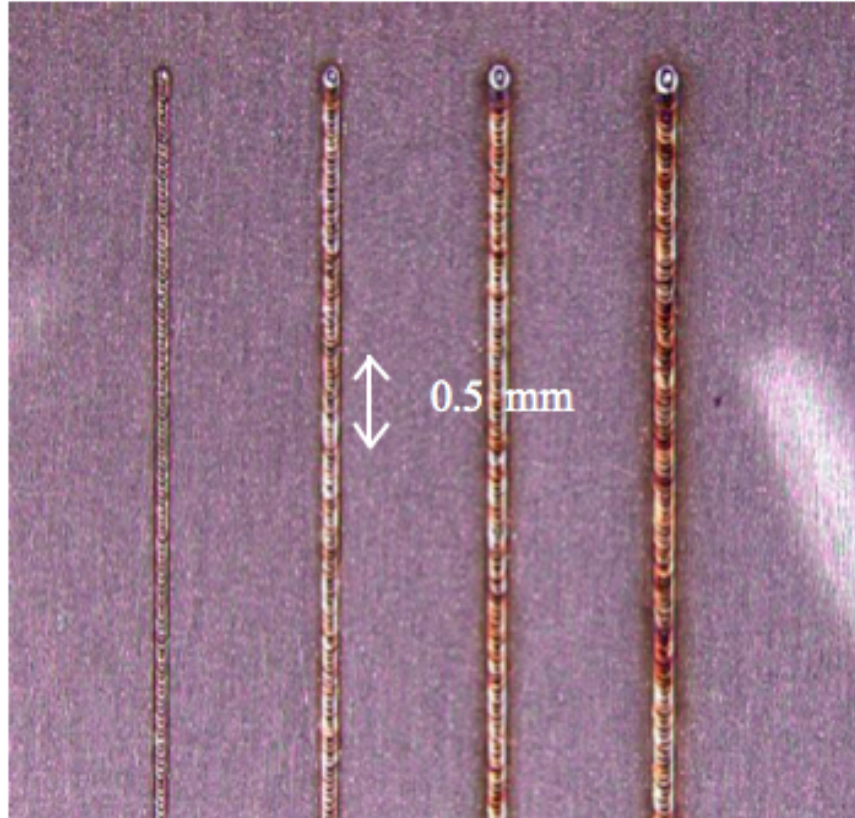


Fig. 104: Top view of fibre laser weld beads in stainless steel (left to right) at 40W, 60W, 80W and 100W peak power for 200Hz pulse-to-pulse frequency, 2 ms pulse length, 4 mm/s weld speed and argon shielding gas.

Figure 104 shows the top view of a series of laser welds made with the fibre laser in stainless steel. The next figure shows the numeric evaluation of laser welding bead width as a function of laser peak power and pulse width.

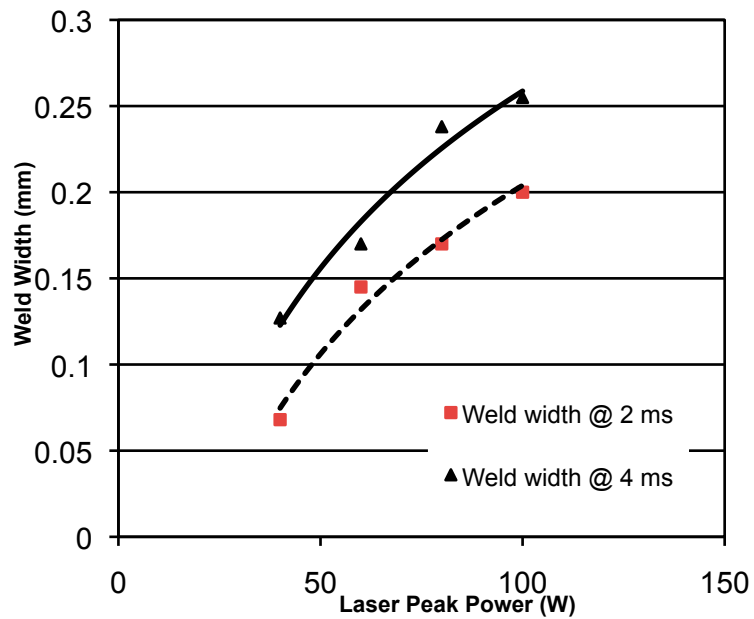


Fig. 105: Weld width as a function of laser peak power and pulse width in stainless steel for 200 Hz pulse-to-pulse frequency, 2 and 4 ms pulse length, 4 mm/s weld speed and argon shielding.

Figure 105 shows how the weld bead width changes with laser peak power for two different laser pulse lengths. The fitted trend line was not linear like the results for the weld penetration shown in figure 103. A logarithmic trend line provided a good fit for this data. The width increases less rapidly than the depth and the weld becomes keyhole-like at high peak power. The weld bead width was in the range of 0.06 to 0.25 mm dependent on the laser settings used in the experiments. The 4 ms pulse length compared with the 2 ms pulse length created an approximately 0.05 mm wider weld bead for the investigated laser peak power range.

3.3.4. Welding of Titanium with Pulsed Fibre Lasers

The following figure 106 shows a cross section of a weld in titanium as an example of a material other than stainless steel. This weld sample was

realized with 80 W laser peak power at 200Hz and 4 ms pulse length. The weld speed was 4 mm/s. The weld penetration was similar to the example in stainless steel at the same laser settings but the weld bead width was slightly wider.

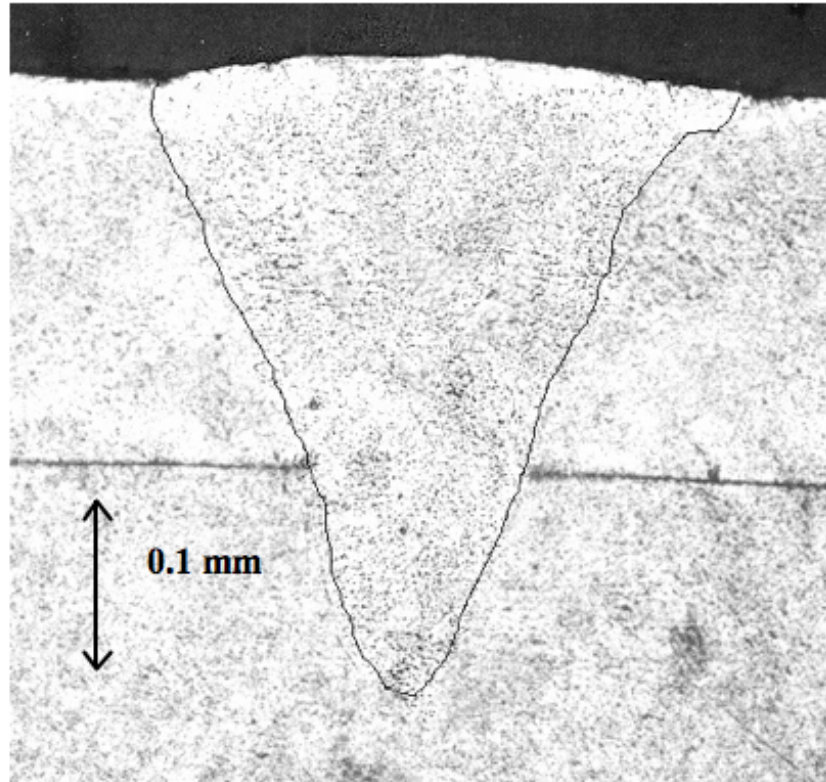


Fig. 106: Typical cross section of a fibre laser weld after etching the titanium sample to make the weld zone visible.

For this experiment a lap weld comprising of two 0.26 mm titanium sheets was produced. For better visibility of the heat affected zone the boundary between the re-solidified weld metal and the non-melted material is highlighted. The weld penetration was 0.35 mm and the weld bead width was 0.3 mm.

3.3.5. Setup to Measure Energy Stability for Pulsed Fibre Laser Welding

Pulse energy stability is an important specification for a hermetic welding application in the medical field. Fluctuation in pulse energy could inhibit the hermetic seal of a package and has the potential to damage the electronic components in the package.

This investigation will present pulse energy stability measurements for two timeframes. The first dataset will show the pulse energy stability during the timeframe of 20 seconds. 20 seconds is the typical timeframe for one weld operation (one part) in production. The second dataset will provide the stability of the laser system during a timeframe of one hour, which is the typical time between power calibrations of the laser welding system in production.

The laser setting for this measurement was 10W average laser power at 100 Hz pulse-to-pulse frequency and 2 ms pulse length. The laser peak power during the measurement was 50 W. A power meter was used to verify the absolute average laser power level and a photo diode was pointed towards the laser power head to collect data for the pulse-to-pulse energy stability measurement. An oscilloscope recorded the photo diode signal with an output interface to a PC. The Tektronix WaveStar™ software package was used in conjunction with the oscilloscope to collect and analyze the data. The recording system sampled one data point every second. Each recorded data point was equivalent to the area below the trace line of the temporal pulse shape shown in figure 101. The WaveStar software package calculated the area below each measured laser pulse. Any change in area below the pulses will be an indicator of pulse energy fluctuation. The red area in figure 107 illustrates the calculated area used for the energy stability investigation.

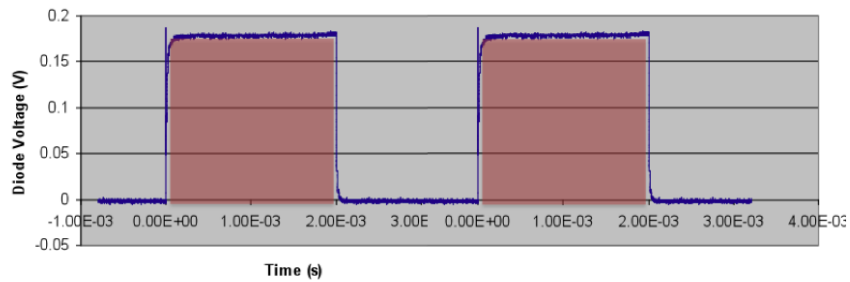


Fig. 107: Sample pulse train for Energy stability measurement.

3.3.5.1. Results for the Energy Stability of Pulsed Fibre Lasers

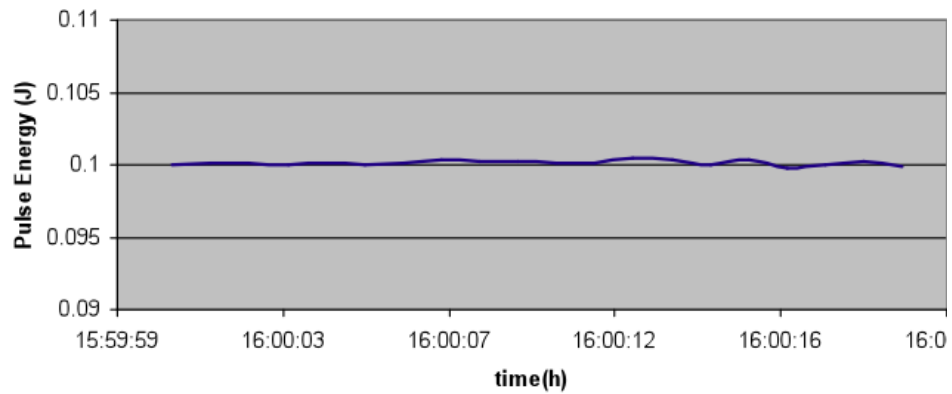


Fig. 108: Short term power stability over 20 seconds at 100Hz, 2 ms pulse length, 50 W peak power and 10 W average power.

Figure 108 plots the pulse energy stability during a standard welding application. The energy in each pulse was very constant during this short timeframe and hence was very stable. The standard deviation from the mean was 0.125%.

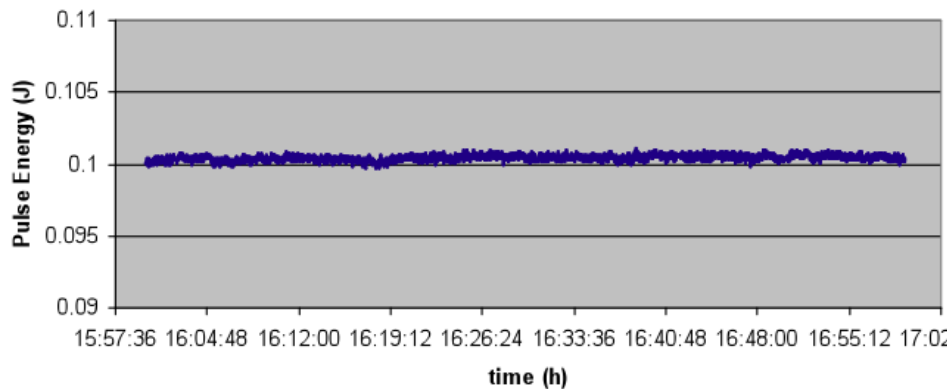


Fig. 109: Long term power stability over 1 hour at 100Hz, 2 ms pulse length, 50 W peak power and 10 W average power.

The power stability for 1 hour is plotted in figure 109. The standard deviation of 0.159% was only slightly higher than for a 20 second measurement. The energy stability of the pulsed fibre laser setup was well above the requirements of welding performances for hermetic sealing applications. The pulse energy fluctuation tolerated for this application is typically in the order of plus/minus 2-5%. Since the fibre lasers 3- σ variation is less than 0.5 % the stability is well beyond application requirements.

3.3.6. Conclusions on Pulsed Fibre Laser Welding

- 1.) Compared to continuous wave laser welding, the pulsed operation of the fibre laser provided additional parameters to tailor the laser operation for microwelding applications.
- 2.) The weld penetration, weld bead width and welding speed were sufficient for many welding applications in the medical and electronics industries. Typical weld penetrations in the range of 0.1 to 0.5 mm for hermetic metal enclosures in the medical field

can be addressed with a 100W fibre laser at 4 mm/s process speed.

- 3.) First investigations showed excellent results in both stainless steel and titanium, in contrast to the CW welding results, which were significantly better in stainless steel compared to titanium. It appears that pulsed operation of the fibre laser allows for the more efficient keyhole welding process in both materials.
- 4.) The pulse-to-pulse fibre laser energy stability is excellent during short-term and long-term measurements. The pulse-to-pulse stability is at least an order of magnitude better than the specifications of a pulsed lamp pumped Nd:YAG laser.

4. Industrial Implementation

The goal of the project summarized in this thesis was to investigate the use of single mode fibre lasers for the manufacturing of medical devices such as stents and pacemakers. Based on the results of this investigation the industrial sponsor of this work made several improvements to their production operation.

- 1.) The developments, results and conclusions of this thesis led to a replacement of most flash lamp pumped lasers for stent cutting by the sponsor of this project. So far more than 50 fibre laser based stent cutting systems have been installed on the sponsor's production floor.
- 2.) The introduction of fibre laser based stent cutting systems led to a reduction in clean room space requirements by 50% in the stent cutting production area. Each Nd:YAG laser used approximately 2 m² of floor space, mainly due to the laser's long resonator setup which has to be mounted horizontally in the production system. The fibre laser reduced that to approximately 1 m². The fibre laser is just a 19" 6U high rack mounted box. The laser power is fibre delivered and does not need an optical delivery system based on mirrors.
- 3.) The laser-related down time was reduced from 15-20% to <1% with fibre lasers. The Nd:YAG system requires periodical exchanges of flash lamps. Only especially trained maintenance personnel are allowed to change the flash lamps because of the risk of high voltage shock. Complications during the lamp

change, such as breakage of the lamp or contamination of the optics often increased the down time. The Nd:YAG laser's resonator is mounted on an optical bench. Re-alignment of the components of the optical bench required the assistance of the laser technician and often extended the down time of the system.

- 4.) Position synchronized output (PSO) enabled cutting systems were introduced into the production and increased the throughput by 30%. The maximum cutting speed was increased from 4 mm/s to 7 mm/s without a reduction in cutting quality.
- 5.) The fibre laser technology eliminated the need of a house water-cooling system. Compact water-to-air chillers can support each system. The maximum cooling capacity only needs to be 50-100W. The introduction of the fibre laser technology reduced the necessary cooling capacity by a factor of 10.
- 6.) The introduction of the fibre laser enabled significant cost reductions. The compact system and the ease of integration of the fibre coupled laser reduced the capital cost of a stent cutting system by 20% (\$50,000). The operation expenses are reduced due to a reduction in energy and cooling requirements by a factor of 10. Additionally the expenses related to the lamp exchanges on a single Nd:YAG can add up to the cost of a fibre laser (\$30,000) in 5 years, providing additional justification of the replacement of lasers in existing systems.

5. Conclusions

The detailed conclusions of each experimental investigation are included at the end of each relevant section. The most significant conclusion is that the fibre laser is an effective next generation replacement for the traditional lamp pumped Nd:YAG laser for cutting and welding applications in medical device production.

The fibre laser has superior beam quality stability at a range of power levels, it has excellent pulse-to-pulse and long-term power stability, and it has the ability to be directly pulse modulated over wide range of pulse lengths and duty-cycles.

The development of fibre lasers with greater than 50 W of average power has enabled the use of this technology in metal micromachining. The fibre laser's improved features described above have been shown in this thesis to lead directly to improved performance for welding and cutting applications. As an example the ability of the fibre laser output to be synchronized with a variable cutting speed allowed control of the heat affected zone in microcutting and enabled higher cutting speeds. This technology has been rapidly adopted and implemented in the production of medical stents by the industrial sponsor of this thesis. The work in this thesis also presented and discussed continuous welding as well as keyhole welding results with CW and pulsed fibre laser for microwelding applications.

The results presented in this thesis were the first published cutting results with fibre lasers. Directly based on this work, the sponsor was able to get

two patents awarded. Additional patents are still in review and are pending (see patents and publications section in this thesis).

At the time the research described in this thesis was completed fibre lasers showed promising first results for microwelding. The development of even higher pulse power fibre laser systems in the last few years has enabled even more applications for CW and pulsed fibre lasers. New high power pulsed fibre lasers in the kilo-watt range are now addressing cutting and welding applications in a wide range of micro and macro material processing fields including automotive, aeronautic, medical, electronics and heavy industries.

REFERENCES

- 1 Andreas Adam, Robert F Dondelinger, Peter R Mueller. "Textbook of Metallic Stents", Isis Medical Media, p. 3, 1997.
- 2 Morton J Kern. "The Interventional, Cardiac Catheterization Handbook", Mosby, p. 38, 2004.
- 3 Patrick W Serruys, Benno J Rensing. "Handbook of Coronary Stents", Martin Dunitz Ltd, p. 3, 2002.
- 4 Dr. Caroline Wright. "Pharmaceutical Issues in Perspective", Kluwer Academic Publishers, p. 2, Jan 2006.
- 5 Richard Saunders. "Method and apparatus for direct cutting of metal stents" US Patent filed in Nov. 1994. Patent number: 5759192.
- 6 Ruediger Hack. "Material Processing with Fiber Lasers" Industrial Laser Solutions, p. 37, Feb. 2003.
- 7 Ken Watkins, Klaus Kleine, Brad Whitney. "Use of Fiber Lasers for Microcutting in Applications in the Medical Device Industry" Proc. ICALEO 2002, Scottsdale, AZ, USA, 2002.
- 8 O Aquilina. "A brief history of cardiac pacing", Jones and Bartlett Publishers, p. 52, 2006.
- 9 Valentin Fuster, Robert A Q'Rourke, Richard Walsh, Philip Poole-Wilson. "Hurst's the heard", The McCraw-Hill Company, p. 1035, 2007.
- 10 Aaron B. Hesselson. "Simplified Interpretation of Pacemaker ECGs", Blackwell Publishing, p. 23, 2003.
- 11 Narendra B Dahotre, Sandip P Harimkar. "Laser Fabrication and Machining of Materials", Springer, p. 247, 2008.
- 12 P Gruenewald, J Cashmore, J Fieret, M Gower. "High-resolution 157 nm Laser Micromachining of Polymers", SPIE 4274, San Jose, CA, 2001.
- 13 Colin E Webb, Julian D C Jones. "Handbook of Laser Technology and Applications", IOP Publishing, p. 1661-1662, Volume 3, 2004.

- 14 Marc J Madou. "Fundamentals of Microfabrication – The Science of Miniaturization", CRC Press, p. 404, 2001.
- 15 H K Toenshoff, A Ostendorf, K Koerber, C Kulik, G Kamlage. "Mirco Material Processing usning UV Laser and Femtosecond Laser", Initiatives of Precession Engineering at the Beginning of a Millennium", Kluwer Academic Publishers p. 62-66, 2001.
- 16 Ruediger Hack, Jeffrey P Sercel, Matthew Philpott. " The expanding role of excimer laser", Industrial Laser Solutions, Oct. 2006.
- 17 John C Ion. "Laser Processing of Engineering Materials", Elsevier Publisher, p. 358, 2005.
- 18 Frank J Duarte. " Tunable Laser Applications", CRC Press, p. 213, 2009.
- 19 Dieter Schuoecker. " Handbook of the EuroLaser Academy, Volume 2", Chapman and Hall, p. 246, 1998.
- 20 Encyclopedia Britannica. "Aberration", p. 56, 2008.
- 21 Chris E Little, Nikola V Sabotinov. "Pulsed Metal Vapor Laser", p. 336, Proceedings of the NATO Advanced Research Work Shop, St. Andrews, UK, 1996.
- 22 Melles Griot, Products, Technical Guide, Fundamental Optics, p. 1-17, 2009.
- 23 Wolfgang Menz, S S Dimov, Bertrand Fillon. "Laser Micro-milling of Ceramics, dielectrics and metals using nanosecond and picosecond lasers, Elsevier Ltd, p. 131, 2006.
- 24 K Richter, W Behr, U Reisgen. "Low Heat Welding of Titanium Materials with Pulsed Nd:YAG Lasers", Materialwissnschaft und Werkstofftechnik, Vol. 38, Issue 1, p. 51-56, 2007.
- 25 William M Steen. "Laser Material Processing", Springer, p. 92, 1998.
- 26 Safa O Kasap, Peter Capper. "Springer Handbook of Electronic and Photonics Materials", Springer, p. 75, 2006.
- 27 Sidney F Ray. "Applied Photographic Optics: Lenses and Optical Systems for Photography", Focal Press, p. 19, 2002.

- 28 C J Nonhof. "Material Processing with Nd-Lasers", p. 67, 1988.
- 29 Michel J F Digonnet. "Rare-Earth-Doped Fiber Lasers and Amplifiers", p. 214, 2001.
- 30 Narendra B Dahotre, Sandip P Harimkar, " Laser Fabrication and Machining Materials", Springer, p. 146, 2008.
- 31 William M Steen. "Laser Material Processing", Springer, p. 107-120, 1998.
- 32 A Mahrle, E Beyer. "Theoretical aspects of fibre laser cutting", Journal of Physics 42, 2009.
- 33 Flemming O Olson. "LIA Handbook of Laser Processing" Laser Institute of America, 2001.
- 34 William M Steen. "Laser Material Processing", Springer, p. 67, 1998.
- 35 H Weber, G Herziger. "Laser-Grundlagen und Anwendungen" Physik Verlag, Nuernberg, p. 225, 1972.
- 36 William M Steen. "Laser Material Processing", Springer, p. 116, 1998.
- 37 Elijah Kannatey-Asibu. "Principles of Laser Material Processing", Wiley, p. 475, 2009.
- 38 Kenneth W Whitten, Raymond E Davis, M Larry Peck. "Chemistry", Brooks and Cole, p. 1068, 2009.
- 39 I Miyamoto, H Maruo. "The Mechanism of Laser Cutting", Welding World 29, p. 283, 1991.
- 40 J Powell, D Petring, R V Kumar, S O Al-Mashikhi, A F H Kaplan, K T Voisey. "Laser-oxygen cutting of mild steel: the thermodynamics of the oxidation reaction", Journal of Physics 42, 2009.
- 41 Charles L Caristan. " Laser Cutting guide for Manufacturing", SME, p. 169, 2004.
- 42 Charles L Caristan. " Laser Cutting guide for Manufacturing", SME, p. 160, 2004.

- 43 Elijah Kannatey-Asibu. "Principles of Laser Material Processing", Wiley Publishing, p. 454, 2009.
- 44 Charles L Caristan. "Laser Cutting guide for Manufacturing", SME, p. 21, 2004.
- 45 Dieter Schuoecker. "High Power Lasers in Production Engineering", Imperial College Press, p. 267-277, 1999.
- 46 Gy Meszlenyi, J Dobranszky, L Devenyi. "Laser Cutting of Stainless Steel thin Sheets with Pulsed Nd:YAG Lasers", Gepesze, 2008-N-02, 2008.
- 47 Li Chen. "Laser Cutting for Medical Device (stent) –Yesterday, Today and Tomorrow", p. 319-430, Proceedings ICALEO, Temecula, CA, USA, 2008.
- 48 William M Steen. "Laser Material Processing", Springer, p. 128, 1998.
- 49 Beno Benhabid. "Manufacturing: Design, Production, automation and Integration", Marcell Dekker, Inc, p. 324, 2003.
- 50 Christopher Dawes. "Laser Welding a Practical Guide", Abington Publishing, p. 18, 1992.
- 51 William M Steen. "Laser Material Processing", Springer, p. 152, 1998.
- 52 Zhili Feng. "Processes and mechanisms of Welding Residual Stress and Distortion", Woodhead Publishing, p. 61, 2005.
- 53 H K Toenshoff, A Ostendorf, K Schaefer. "Fiber Laser – Compact Source for Micro Welding, ICALEO 1998.
- 54 E Dumord, J M Jouvard, D Grevey. "Keyhole Modeling During CW Nd:YAG Laser Weleing, p. 214, 1996.
- 55 Isamu Miyamoto, Seo-Jeong Park, Toshihiko Ooie. "Ultrafine-Keyhole Welding Process Using Single-Mode Fiber Laser, ICALEO, Jacksonville, CA, USA, 2003.
- 56 W W Duley. "Physics, Chemistry, and Laser Microprocessing", Journal of Laser Applications, Volume 16, Issue 1, p. 52-54, February 2004.

- 57 D Rosenthal. "Mathematical Theory of Heat Distribution During Welding and Cutting", *Welding Journal*, Vol. 20, No. 5, p. 220-234, 1941.
- 58 William M Steen. "Laser Material Processing", Springer, p. 148, 1998.
- 59 Colin E Webb, Julian D C Jones. "Handbook of Laser Technology and Applications", IOP Publishing, p. 1607, Volume 3, 2004.
- 60 Charles L Caristan. "Laser Cutting guide for Manufacturing", SME, p. 140, 2004.
- 61 Charles L Caristan. "Laser Cutting guide for Manufacturing", SME, p. 159, 2004.
- 62 A Ivarson, J Powerll, J Kamalu, G Borden, C Magnusson. "The Effects of Oxygen Purity in Laser Cutting Mild Steel", *Laser Eng.* 1, p. 299, ICALEO, Orlando, FL, USA, 1993.
- 63 Leonard Migliore. "Welding with Lasers", *Industrial Laser Review*, Pennwell, July 1998.
- 64 A Scharff, O G Kasatkin, V N Zamkov. "Titanweld – An Information Software for Welding Titanium Alloys", 4th International Seminar Numerical Analysis of Weld Ability" Graz-Seggau, 1997.
- 65 J Norberto Pires. "Welding Robots: Technology, System Issues and Applications", Springer, p. 52, 2006.
- 66 Richard C Powell. "Physics of Solid-State Laser Materials", Springer, p. 22, 1998.
- 67 William M Steen. "Laser Material Processing", Springer, 1998.
- 68 Picture retrieved from University of Lancaster website, www.lancs.ac.uk/ug/parkt/, 11-12-09
- 69 A. Roy Hender. "A Guide to Laser Safety", Chapman and Hall, p. 71, 1997.
- 70 Lindsay W Austin, Adolf Giesen, Daniel H Leslie. "Beam control, diagnostic, standards und propagation", SPIE, San Jose, CA, USA, 1995.

- 71 Colin E Webb, Julian D C Jones. "Handbook of Laser technology and applications, Volume 1", IOP Press, p. 97, 2004.
- 72 Leonard Migliore. "Laser material Processing", Marcel Dekker, Inc, p. 52, 1996.
- 73 Walter Koechner, "Solid-State Laser engineering", Springer, 1996.
- 74 Denis R Hall, Paul E. Jackson. "The Physics and technology of laser resonators", Taylor and Francis Group, p. 159-161, 1989.
- 75 Walter Koechner, "Solid-State Laser engineering", Springer, p. 237, 2006.
- 76 Reinhard Ifflaender. "Solid-State Lasers for Material Processing Fundamental Relations and Technical Realization", Springer, p. 149, 2001.
- 77 Walter Koechner, "Solid-State Laser engineering", Springer, p. 73, p. 309-310, 2006.
- 78 William T Silfvast. "Laser Fundamentals", Cambridge, p. 570-571, 2003.
- 79 Chai Yeh. "Applied Photonics", Academic Press, p. 60-65, 1994.
- 80 Roland Diehl. "High-power diode lasers: Fundamentals, technology, Applications", Springer, p. 370-380, 2000.
- 81 D Kouznetsov, J V Moloney. "High efficient, high-gain, short length, and power-scalable incoherent diode slab-pumped fiber amplifier/laser", Journal of OSA, p. 1452-1462, 2003.
- 82 Daniel Malacara, Brian J Thompson. "Handbook of Optical Engineering", Marcel Dekker Inc, p. 788, 2001.
- 83 Giuseppe Palumbo, Ticcardo Pratesi. "Laser and Current Optical techniques in Biology", The Royal Society of Chemistry, p. 150, 2004.
- 84 IPG Product information, information from IPG's website
- 85 SPI Product information, information from SPI's website

- 86 Victor Rossin, Matthew Peters, Erik Zucker, Bruno Acklin. "Highly reliable high-power broad area laser diodes", Proceedings of SPIE, San Jose, CA, USA, Volume 6104, p. 61-70, 2006.
- 87 Y Jeong, J K Sahu, D N Payne, J Nilsson. "Ytterbium-doped large-core fiber laser with 1.36 kW continuous-wave output power", Optics Express, Vol. 12, Issue 25, p. 6088-6092, 2004.
- 88 V Gapontsev, William Krupke. "Fiber laser grow in Power", Laser Focus World, Pennwell, p. 83-87, August 2002.
- 89 Stephen Norman, Mikhail Zervas, Andrew Appleyard, Michael Durkin, Ray Horley, Malcolm Varnham, Johan Nilsson, Yoonchan Neong. "Latest Development of High Power Fiber Lasers in SPI" Proc. Photonics West, San Jose, CA, USA, No. 5335-33. 2004.
- 90 A Miller, D M Finlayson. "Laser sources and applications", SUSSP Publications, p. 163, 1997.
- 91 Michael M Parker. "Physics of optoelectronics", Taylor and Francis Group, p. 33, 2005.
- 92 R Paschotta. "Encyclopedia of Laser Physics and Technology", Wiley-VCH, p. 142, 2008.
- 93 D Wolf, G Bonati, P Hennig H Voelckel. "Reliability of high power diode laser bars in industrial applications" SPIE, Vol 5711", P. 66-72, 2005.
- 94 C G Masi. "Basic Optics Effects Limit Image Quality", Test and Measurement World, Reed, 5/1/2000.
- 95 Thorlabs Product Specification DET 410, 2009.
- 96 ISO/DIN 11146-2:2005, "Laser and laser-related equipment-Test methods for beam widths, divergence angles and beam propagation ratios – Part 1, 2 and 3", 2005.
- 97 Mells Griot, Product Literature, p. 43.24, 2009.
- 98 R Paschotta et al. "Ytterbium Doped Fiber Amplifiers" IEEE Journal of Quantum Electronics 33: p. 1049-1056, 1997.
- 99 C S Lee, A Goel, H Osada. "Parametric studies of pulsed-laser cutting of thin Metal plates" Amada Engineering, Jan 1985.

- 100 V King, J Powell. "Laser-cut mild steel – factors affecting edge quality" E I Monthly, April 1985.
- 101 P M Ilavarasan, P A Molian. "Modeling of Surface Roughness in Laser Cutting" Proc. Of fifth Int. FAIM Conference, Stuttgart, Germany, June 1995.
- 102 H Weber, G Herziger. "Laser-Grundlagen und Anwendungen" Physik Verlag, Nuernberg, 1972.
- 103 Scanlab GmbH, Product Literture, hurrySCAB TM, 2007.
- 104 Ulrich Duerr. "High-Speed Contour Welding" Industrial Laser Solutions, Pennwell, Nov. 2004.
- 105 Alexander M Olowinsky, Kilian Klages, Jens Gedicke. " Shadow a new welding technique: basics and applications", ICALEO, San Francisco, CA, USA, 2004.
- 106 Stan Ream. "Disc and fiber gain ground" Industrial Laser Review, Pennwell, February 2005.
- 107 D K Y Low, et al. "Taper Control During Laser Percussion Drilling of NIMONIC Alloy Using Sequential Pulse Delivery Pattern Control", ICALEO, San Diego, CA, USA,1999.

**PATENTS, PUBLICATIONS AND ACADEMIC
CONTRIBUTIONS TO DATE BY THE AUTHOR**

Patents awarded:

Klaus R F Kleine, et al.

“Pulsed fiber laser cutting system for medical implants”

Patent 6,927,359, filed February 18, 2003

Stephen Jones, Klaus R F Kleine, Brad Whitney

“Pulsed fiber laser cutting system for medical implants”

Patent 6,521,865, filed June 14, 2001

Larry R. Marshall, Klaus R F Kleine

“Aspheric lensing control for high power butt-coupled end-pumped laser”

Patent 6,222,869, filed June 3, 1998

Henry Kobsa, Klaus Kleine

“Method and Apparatus for Laser Cutting Materials”

Patent EP07704448, filed October 27, 1995

Klaus Kleine, et al.

Two additional Patents awarded for Stent Materials

Patent Applications:

Klaus R F Kleine, et al.

“Pulsed Synchronized Laser Cutting of Stents”

Application 20070228023, filed March 30, 2006

Klaus R F Kleine, et al.

“Laser induced plasma machining with an optimized process gas”

Application 20070045255, filed August 23, 2005

Papers:

Klaus Kleine

“High-Power Multi kW Diode Lasers, Structure and Applications”

Proc. CLEO 2008, Paper PThB2, San Jose, CA, 2008

Ken G Watkins, Klaus Kleine

“Fiber Laser Microcutting with Pulsed Synchronized Output”

Proc. CLEO 2006, Paper PThE, Long Beach, CA, 2006

Ken G Watkins, Klaus Kleine

“Pulse shaping for microcutting of metals with fiber lasers”

Proc. SPIE, Volume 5339, Page 510, 2004

Ken G Watkins, Klaus Kleine

“Fiber laser for microcutting of metals”

Proc. SPIE, Volume 4974, Page 184, 2003

Ken G Watkins, Klaus Kleine, Brad Whitney

“Use of Fiber Lasers for Microcutting Applications in the Medical Device Industry”

Proc. ICALEO 2002, Paper M509, Scottsdale, AZ, 2002

Ken G Watkins, Klaus Kleine

“Microwelding with Single Mode Fiber Lasers”

Proc. of the third International WLT Congress in manufacturing 2005,
Munich, June 2005

Ken G Watkins, Klaus Kleine

“Microwelding with Pulsed Single Mode Fiber Lasers”

Proc. ICALEO 2004, San Francisco, CA 2004

Articles

Klaus Kleine, Andre Eltze

“Diode Lasers for Plastic Welding”

Industrial Laser Solutions, October 1, 2006

Presentations

Klaus Kleine

“Recent Developments on Pulsed Diode Laser Systems”

2nd Advanced Laser Application Information Exchange, Chicago, IL
August 29, 2006

Klaus Kleine

“ Laser Brazing with High Power Diode Lasers”

ALAW 2007, Plymouth, MI, 2007